2017-04-20

The Investigation on Natural Assembly for Biomedical Application

Xu Han
University of Miami, nkhanxu@gmail.com

UNIVERSITY OF MIAMI

THE INVESTIGATION ON NATURAL ASSEMBLY FOR BIOMEDICAL APPLICATION

By

Xu Han

A DISSERTATION

Submitted to the Faculty
of the University of Miami
in partial fulfillment of the requirements for
the degree of Doctor of Philosophy

Coral Gables, Florida

May 2017

UNIVERSITY OF MIAMI

A dissertation submitted in partial fulfillment of
the requirements for the degree of
Doctor of Philosophy

THE INVESTIGATION ON NATURAL ASSEMBLY FOR BIOMEDICAL APPLICATION

Xu Han

Approved:

_____ Roger M. Leblanc, Ph.D. Chairman and Professor of Chemistry	_____ Françisco M. Raymo, Ph.D. Professor of Chemistry
_____ Jamie D. Walls, Ph.D. Associate Professor of Chemistry	_____ Guillermo Prado, Ph.D. Dean of the Graduate School

_____
Yidong Yang, Ph.D.
Assistant Professor of Radiation Oncology

HAN, XU (Ph.D., Chemistry)
The Investigation On Natural Assembly For Biomedical Application (May 2017)

Abstract of a dissertation at the University of Miami.

Dissertation supervised by Professor Roger M. Leblanc.
No. of pages in text. (110)

Nature materials achieve structural complexity by inducing a network of molecules into forming elaborate hierarchical nanostructures. The efficiency of organizing these assembly processes in respond to the structure changes demonstrates certain cellular functions. However, attempts to explore the assembly of natural or non-biological materials to help design a better system in the application of drug discovery and biosensing nanotechnology still remain a major challenge. The aims of the research are to develop new class of materials, examine their role on inducing biomaterials assembly to form hierarchical structures, and to utilized their emergent properties for the new design of a biocompatible system.

Amyloid-β peptides (Aβ) fibrillation is pathologically associated with Alzheimer's disease (AD), resulting in the development of Aβ inhibitor essential for the treatment of AD. To this end, my research focused on the discovery of potential agents, including resorcinarene and carbon dots, to help redirect the nature assembly of Aβ. Different experimental and computational methods were examined, and these studies demonstrate not only clues to understanding interactions involved in Aβ fibrillation, also a novel strategy for the discovery of novel antiamyloidogenic agents for AD treatments.

Another topic of this thesis is to mimic the nature assembly to design a system for diagnostic detection. Currently, different diseases and cancers are costly and require

complicated analysis methods, such as ultrasound (US), computerized tomography (CT) scan, electrocardiography (ECG), and magnetic resonance imaging (MRI). What's worse, these strategies often delay timely treatment, and most diseases and cancers happen without any symptoms. Thus, it is essential that new techniques be implemented for parallel detection of several diseases at the same time to expedite clinical treatments. To this end, the binding of antibody with antigen was performed based on the localized surface plasmon resonance. The assembly of the antibody with the antigen successfully provides an excellent platform for the biosensing. This study may also help lead to breakthroughs in the sensing nanotechnology and future clinical use.

To my loving parents

And

My wife

And

My parents-in-law

ACKNOWLEDGEMENTS

I would like to acknowledge the support and encouragement I received during my doctoral research. First and foremost, I am incredibly grateful for my advisor and mentor, Dr. Roger M. Leblanc, who stood by to support me along the way. He has always put his students and their future career first. As is known, the Ph.D. life is challenging and stressful, but I experienced a happy and exciting journey with the guidance of Dr. Leblanc. I would like to thank you for encouraging my research and for allowing me to grow as a research scientist. Your advice on both research as well as on my career have been priceless. I would always feel grateful and lucky to have Dr. Leblanc as my advisor and mentor in my academic career. I could not have imagined having a better advisor and mentor for my Ph.D. study.

Besides my advisor, I would like to thank my committee members, professor Françisco M. Raymo, professor Jamie D. Walls, and professor Yidong Yang for serving as my committee members. I want to thank you for letting my defense be an enjoyable moment, and for your brilliant comments and suggestions. In addition, I would like to extend my thanks to Dr. Adam B. Braunschweig for his academic advise, discussions, and help at the beginning of my Ph.D. career.

My sincere thanks also goes to my father, Wenxing Han, and my mother, Xiangchun Jin, for their love and support throughout my life at the University of Miami. A special thanks to my farther-in-law, Guomin He, and my mother-in-law, Xiaowei Bo, both of your prayers for me is what have sustained me thus far.

In particular, I am truly grateful for my wife, Gefei He, for her love, support, understanding, and patience. Without you, I would not have been able to thrive in my

doctoral program in the U.S. and balance my research with everything else. I would also like to thank all of my friends who have incented me to strive towards my goal as well.

I would also like to thank all the current and past group members in Leblanc group, all faculty members and staff and all other graduate students in the Department of Chemistry at the University of Miami, especially Zhili Peng and Shanghao Li, for their sharing and cooperation during my studies. I have learned a lot from them, and thank you for accepting nothing less than excellence from me.

I am also grateful to my collaborators, Dr. Kendall Houk, Dr. Yong Liang, and Dr. Jiyong Park at the University of California, Los Angeles, Dr. Shudan Bian at New York University, Dr. Pengyu Ren and Mr. Zhifeng Jing at the University of Texas at Austin, Dr. Sung Jin Kim, Dr. Hossein Shokri Kojori, Dr. Athula Wikramanayake, Dr. Lingyu Wang, and Mr. Wei Wu at the University of Miami, for their support and insightful comments. Furthermore, I want to give my special thanks to Dr. Hossein Shokri Kojori and Dr. Shudan Bian for their encouragement, intelligent comments, and hard questions which incented me to widen my research from various perspectives, and also for the great support as an intimate friend.

Last but not the least, I would like to extend my thanks to the College of Arts and Sciences at the University of Miami for the financial support in the past five years. Without this, it would be impossible for me to pursue my studies in the Untied States.

TABLE OF CONTENTS

Page

LIST OF FIGURES

Chapter 1

LIST OF TABLES

Chapter 1

Chapter 2

LIST OF ABBREVIATION

Aβ	amyloid-β peptide
Ab	antibody
ACC	American College of Cardiology
ACS	acute coronary syndromes
AD	Alzheimer's disease
AFM	atomic force microscopy
AFU	α-L-fucosidase
Ag	antigen
ALP	alkaline phosphatase
AMI	acute myocardial infarction
AMPPD	3-2'-spiroadamantyl-4-methoxy-4-3''-phosphoryloxy-phenyl-1,2-dioxetane
APP	amyloid precursor protein
AuNP	gold nanoparticle
BACE1	β-secretases
BBB	blood-brain barrier
BSA	bovine serum albumin
CB[7]	cucurbit[7]uril
CD	circular dichroism
C-Dots	carbon dots
CM	center-of-mass
CNF	carbon nanofiber
CNT	carbon nanotube

CT	computerized tomography
cTn	cardiac troponin
CVD	cardiovascular diseases
DI	de-ionized
DLS	dynamic light scattering
DNA	Deoxyribonucleic acid
DPV	differential pulse voltammetry
ECG	electrocardiography
EDC	1-ethyl-3-3-dimethylaminopropyl carbodiimide hydrochloride
ELISA	enzyme-linked immunosorbent assay
EOC	ELISA-on-a-chip
ESC	European Society of Cardiology
FET	field effect transistor
FITC	fluorescein isothiocyanate
FRET	Förster resonance energy transfer
FTIR	Fourier transform infrared
GAFF	generalized Amber force fields
GO	graphene oxide
HCC	hepatocellular carcinoma
hIAPP	human islet amyloid polypeptide
HIV	human immunodeficiency virus
HIVP	HIV-1 protease
HRP	horseradish peroxidase

HSA	human serum albumin
HT	human transferrin
LED	light emitting diode
LFA	lateral flow assay
LOD	limit of detection
LSPR	localized surface plasmon resonances
MA-MEF	microwave-accelerated and metal-enhanced fluorescence
MD	molecular dynamics
MI	myocardial infarction
MRI	magnetic resonance imaging
MWCO	molecular weight cut-off
NACB	National Academy of Clinical Biochemistry
NC	nitrocellulose
NHS	N-hydroxysuccinimide
NIR	near-infrared
NMR	nuclear magnetic resonance
PDB	protein data bank
PDMS	polydimethylsiloxane
PEG	polyethylene glycol
PELE	potential energy landscape explorer web-server
PL	photoluminescent
PMPs	paramagnetic particles
POCT	point-of-care testing

PTKs	protein tyrosine kinases
QDs	quantum dots
QY	quantum yield
RNA	ribonucleic acid
SAM	self assembled monolayer
SDS-PAGE	sodium dodecyl sulfate polyacrylamide gel electrophoresis
Selex	systematic evolution of ligands exponential enrichment
SNF	silver nanoparticle film
SPR	surface plasmon resonance
ssDNA	single strand DNA
TEM	transmission electron microscopy
TEMED	tetramethylethylenediamine
ThT	thioflavin T
TIRFM	total internal reflection fluorescence microscopy
Trp	L-tryptophan
Tyr	tyrosine
WHO	World Health Organization
XPS	X-ray photoelectron spectroscopy

Chapter 1 Introduction

1.1 Protein Fibrillation in the Extracellular Space

Nature materials achieve structural complexity by inducing a network of molecules into forming elaborate hierarchical nanostructures.[1] The efficiency of organizing these assembly processes in respond to the structure changes demonstrates certain cellular functions. One of the primary goals of nanotechnology and biotechnology is to understand, mimic, and affect these nature assemblies so as to be applied in biological, chemical, and other scientific and engineering communities. Within biological systems, the message that directs hierarchical assembly is ciphered within the Watson-Crick based DNA and RNA. Peptide or protein, whereby expressed by these encoded genes, is the major embodiment of biofunction. Research with regard to it can effectively help reveal the rules of life secrets. Amyloid is one resulting production spring from nature assembly, where normally soluble proteins assemble into insoluble fibrils that are resistant to degradation. Extracellular deposition of these amyloid fibrils is believed to be pathological hallmark of several amyloidogenic diseases, such as Alzheimer's, Parkinson's, diabetes type II, multiple myeloma, neuropathies, and cardiomyopathies.[2] Of all these amyloidosis, Alzheimer's disease (AD) is the most common form of dementia and has become a major threat across the globe.[3] Recent reports indicate 81.1 million people are expected to be living with it by the year 2040,[4] and the financial burden is estimated to be $236 billion in 2016 alone.[5] Therefore, the development of therapeutic agents for AD, which can redirect the nature assembly, are undoubtedly at the center of current and future research areas.

The precise mechanism of AD pathogenicity remains to be established, but one considerable molecular etiology that underlies AD involves the aggregation of Aβ 40 and 42 – 40/42-residue fragment of β-amyloid (Aβ) peptide, which are produced from sequentially proteolytic cleavage of amyloid precursor protein (APP) by β- and γ-secretases.[6] APP is a transmembrane glycoprotein. The extracellular domain of APP contains the N terminus of Aβ, while the transmembrane region donates the C terminus of Aβ. The activity of β- and γ-secretases gives rise to the N and C termini, respectively, so as to yield Aβ 40 and 42. Aβ can assemble into flexible soluble oligomers in different forms, but not all peptides follow the encoded assembly process "accurately". What's worse, the misfolded oligomers, also known as seeds, can induce other Aβ peptides to track the front ones, further promoting the formation of Aβ fibrils in a tremendously effective catalytic cycle. To successfully redirect or impede the unhealthy assembly, the inhibitor design involves effective binding towards initial Aβ monomer, oligomer, or filament to disturb the original encoded misassembly process. However, in addition to it, challenges arise with the discovery of potential antiamyloiddogenic agents also include: 1) the toxicity of Aβ 42 oligomer, and 2) capability to penetrate is believed to be toxic to nerve cells. Most scientists also proposed that the toxicity of Aβ oligomers is the primary cause of AD.[7] Thus, along with redirecting the "false" nature assembly of Aβ, inhibition of the toxicity of Aβ oligomers become another concern towards discovering antiamyloiddogenic agents for AD treatment.

1.2 Recent Development of Cardiac Troponin I Detection

Cardiovascular diseases (CVD), heart and blood vessel disease, is mainly related to atherosclerosis. Plaque building up inside the arteries, which limits the flow of blood, can

lead to atherosclerosis. There are a number of reasons, including lifestyle, that may cause CVD. According to the report from the World Health Organization (WHO), there will be over 23.3 million people who die annually from CVD by 2030.[8] In 2010 alone, CVD placed a burden of a total cost of approximately 444 billion dollars in the United States.[9] Myocardial infarction (MI), one of the clinical forms and also one of the most immediately life threatening sorts of acute coronary syndromes (ACS), has caused the most severe adverse cardiac events, such as the irreversible tissue injury in the myocardium.[10] The analysis of MI primarily depends on electrocardiography (ECG), but only 57% of patients can be diagnosed correctly for acute myocardial infarction (AMI), and AMI patients can even show normal or non-diagnostic EGC when presented to the Emergency Department.[11, 12] What is worse, 25% of AMI have happened without any symptoms, like pain in the chest, back or jaw.[13, 14] Therefore, a rapid, sensitive, and cost-efficient platform becomes an urgent demand to focus on to fulfill the diagnosis requirements in AMI detection.

Biomarkers can indicate pathogenic processes resulting from different diseases, and are widely used in basic and clinical research.[15] Any small change of biomarkers measured in the blood can predict the corresponding ongoing disease relatively correctly and rapidly. The ideal biomarker for AMI should be in high concentration in myocardium, and not exist in the noncardiac tissues.[16] The earliest cardiac biochemical marker employed includes lactate dehydrogenase isoenzymes, aspartate aminotransferase, and total lactate dehydrogenase.[17] However, none of them display high specificity to AMI. In 2000, the European Society of Cardiology and the American College of Cardiology (ESC/ACC) announced a new criteria for the indication of AMI diagnosis.[18, 19] It is

recommended that the 99th percentile concentration of a healthy population with the coefficient of variation should be 10% as the cutoff point to avoid false positive results. Right now creatine kinase-MB, myoglobin, cardiac forms of troponin T (cTnT), and cardiac troponin I (cTnI) are valuable diagnostic biomarkers for AMI. Among these biomarkers, cTnI is considered the gold standard for AMI, since it is usually produced only in the myocardium and shows highly specificity to cardiac injury.[20] Since the accuracy of AMI diagnosis reflected by electrocardiogram changes is very low, the assistantance of cTnI biomarker measurements is required for accurate diagnosis. The current research thus has focused more on fabricating a small-sized, rapid, and highly sensitive biochip with the ability for point-of-care testing (POCT). In a typical term, POCT is defined as a test operated near the patients.[21] Depending on the different POCT operating settings, such as doctor offices and emergency departments, there might be minor differences in the definition of the term. According to the guidance and recommendations developed by the National Academy of Clinical Biochemistry (NACB), the turnaround time of POCT should be within 1 h with a specimen of plasma or whole blood.[22]

Troponin complex, including cTnI, cTnT, and cTnC, together with tropomyosin are located on the actin filament, and play an important role as a molecular switch mediating calcium regulation in the contraction of skeletal and cardiac muscle. Human cTnI single isoform is made up of 209 amino acid residues, with a molecular weight of roughly 22.5 kDa.[23, 24] It can inhibit the actomyosin ATPase, and this function can be enhanced in the presence of tropomyosin. The isoform of cTnI in myocardial tissue differs from the sequence of those in skeletal muscles.[25, 26] This difference allows the development of

highly specific antibodies to cTnI without cross reaction with other isoforms of troponin. In a recent study,[27] 0.5 to 2.0 ng/mL cTnI concentration is regarded as the borderline between normal people and patients. After the outbreak of AMI, the cTnI concentration can go up to 50 ng/mL within 3-6 h, and finally to a level around 550 ng/mL.[28] In addition, its concentration still remains elevated for a few days, while that of other biomarkers will decline more rapidly.[29] The cTnI level will go back to its standard status in 6-8 days, such that the diagnostic window is long enough for detection.[30] For conventional cTnI detection methods, many drawbacks, including low sensitivity, and high cost, inhibit their future practical use. Besides, for most tests in a typical hospital setting, serum after a blood separation process is needed.[31, 32] Currently, large and complex instruments, like Roche E 2010/602 cTnI, are used in most clinics,[33] but better performance and properties, such as ultrasenstive rapid detection, label-free technique improvements, and POCT still need to be considered due to the time critical nature of the disease.

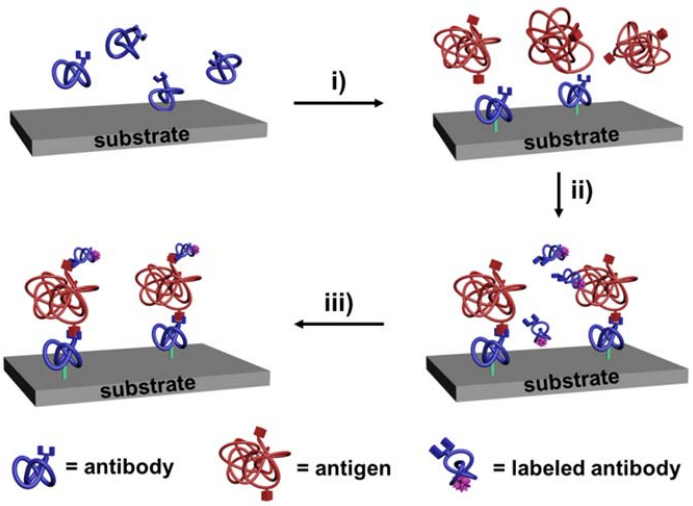

Figure 1.1 i) Antibody was immobilized onto a substrate, ii) antigen was captured by the first antibody on the surface, and iii) the labeled secondary antibody was bound to the antibody

1.2.1 Surface-Immobilized

For decades, immunoassay has been used as a tool for research in the fields of biodetection and clinical diagnostics.[34] The signaling process has extensively expanded from radiolabeling[35] at the very beginning to colorimetric[36], fluorescence[37], paramagnetic[38], electrochemical[28], and others[39-41]. The first immunoassay for cTnI sensing was fabricated in 1987 by radiation technique in a antibody-antigen-antibody sandwich format.[42] Almost all the current cTnI biosensor involves this sandwiched structure at the localized site on the surface. Antibodies are produced in the blood by the white cells. Antigen (biomarker) contains numerous epitopes, but the binding of antibody to the unique epitope of antigen, providing the antibody-antigen-antibody sandwich approach a high specificity. As illustrated in Figure 1.1, antibody (Ab) **1** is immobilized onto a substrate via covalently or noncovalently bonding strategies, followed by capturing the antigen (Ag) from the sample solution. The secondary Ab can be in a more free format. Depending on the label of the secondary Ab, the immunoassay can display different measurable properties, such as color, fluorescence, and electrochemical signal. In such a way, the analyte of interest is able to be detected. However, the conventional strategies require multiple laboratory steps and high expense without POCT performance. Different portable immunoassay based cTnI detection techniques are summarized in Table 1.1 with regard to the method, analytical time, POCT, and detection limit. In the following sections, we will present a review of different scientific reports on colorimetric assay, fluorescent assay, paramagnetic assay, and electrochemical assay, respectively. We will focus more on the different strategies used to improve the speed and sensitivity of cTnI detection.

Table 1.1 Performance and detection methods of different cTnI immunoassays

Method	Platform	Analytic Time	POCT Potential	Limit Detection
HRP	Colorimetric	15 min	High	0.027 ng/mL[36]
HRP	Colorimetric	20 min	Low	5.6 ng/mL[43]
AuNP	Colorimetric	10 min	High	0.01 ng/mL[44]
PDMS-Au-Ag	Colorimetric	1.3 h	Low	0.01 ng/mL[45]
Fluoro-microbead	Fluorescence	40 min	High	0.1 ng/mL[10]
QD, Protein A, AF-546 Dye	Fluorescence	1 min	High	32 nM in PBS 55 nM in human plasma[46]
AMPPD-ALP	Fluorescence	30 min	High	0.1 ng/mL[33]
TiO_2 nanotube array AM700	Fluorescence	2 h	Low	0.1 pg/mL[47]
FITC	Fluorescence	1 min	High	5 pg/mL[48]
Europium(III)	Fluorescence	15 min	High	2 pg/mL[49]
Alexa Fluor 647 donkey anti-mouse IgG	Fluorescence	2.5 h	Low	35 aM[50]
Aptamer	Fluorescence	Over 1 h	Low	5.00 ng/mL[41]
Erenna Immunoassay	Paramagnetic	15 min	High	0.2 pg/mL[38]
Magnetic Nanoparticles	Paramagnetic	5 min	High	3 pM[51]
Magnetic Nanoparticles	Paramagnetic	4.1 min	High	0.50 ng/mL[52]
Magnetic Nanoparticles	Paramagnetic	5 min	High	0.03 ng/mL[53]
HRP enzyme	Electrochemical	1 h	Low	1 ng/mL[28]
QD	Electrochemical	3.7 h	Low	4 pg/mL[54]
Au Nanoparticles	Electrochemical	1 h	Low	0.2 ng/mL[55]
Au Nanoparticles Ru-peptide	Electrochemical	2 h	Low	0.4 pg/mL[30]
Carbon nanofiber	Electrochemical	Over 1 h	Low	0.2 ng/mL[40]
Aptamer	Electrochemical	5 min	High	1.19 ng/mL[56]
Au film Dextran layer	SPR	35 min	High	1.4 ng/mL[39]
Peptide epitope	SPR	5 min	High	0.068 ng/mL[57]
Au nanorod	SPR	15 min	Low	10 ng/mL[58]

1.2.2 Colorimetric assay

The colorimetric immunoassay is based on the principle of the amount of the light absorbed by the chromogenic reaction at the specific wavelength in the presence of analyte. This type of assay was not developed until the year 1971, to avoid the hazardous process from radio-immunoassay.[35] Generally the colorimetric assay is now known as enzyme-linked immunosorbent assay (ELISA). Similar to the sandwiched assay principle, Ag is captured by the Ab **1** at first, and the second enzyme linked Ab will be added to form sandwiched complex. Finally the changed color and corresponding measurements can determine the analyte quantitatively.

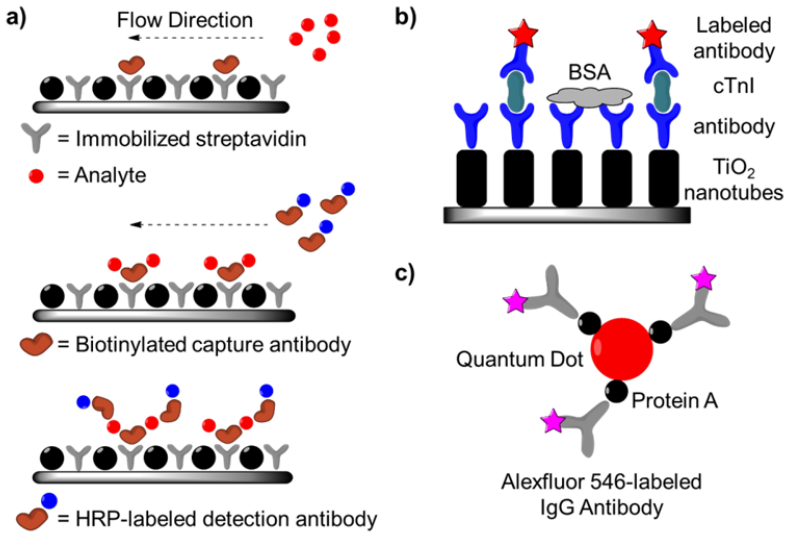

Figure 1.2 a) Capture antibody BD clone 12 was immobilized onto the surface by biotinylation. Analyte, cTnI, and HRP labeled antibody were sandwiched onto the substrate.[36] b) Anti-goat troponin antibody, cTnI, and fluorophore labeled anti-mouse troponin were sandwiched onto a TiO_2 array.[47] c) The labeled capture antibody were attached to the quantum dot by a bridge molecule protein A.[46]

Based on the basic principle described above, horseradish peroxidase (HRP) which can initiate a chemiluminometric signal was widely utilized to build the colorimetric assay.[43, 59-61] Cho *et al.*[36] fabricated an ELISA-on-a-chip (EOC) biosensor for cTnI (figure 1.2a). The sensor employed cross-flow chromatography technique, vertical channel for holding the immune-strip and horizontal channel for detecting, and in such a way variable signals were able to be detected at the sites of complex formation. A monoclonal antibody (BD clone 12) which is specific to cTnI was functionalized by biotinylation. Then another BD clone 12 was labeled by HRP, which is used to catalytic oxidize a luminogenic substrate luminol. Analyte (cTnI), biotinylate functionilzed antibody, and HRP labeled antibody were sandwiched onto the substrate via biotin-streptavidin interaction through vertical channel. Luminol passed through the immobilized surface, and chemiluminometric signal generated was captured by a simple detector installed in the chamber. After adding the cTnI antigen, only approximately 20 min are needed for the incubation and measurement process.

In addition to HRP chemistry, gold nanoparticle (AuNP) based colorimetric assay is another optional approach for cTnI sensor, which is carried out by using AuNPs to catalyze the silver reduction. In 2010, Wu *et al.*[45] developed a poly(dimethylsiloxane) (PDMS)-gold composite film-based biosensor. Anti cTnI antibody and cTnI antigen were captured onto the PDMS-AuNPs surface separately. Since the spot blocked by the cTnI can influence the amount of the silver reduction, the color would be different in each reaction wells. The method shows small size, cost-effective, and high sensitivity (0.01 ng/mL) characteristics, but over 1 h incubation time is needed after adding the antigen. Similar to the Wu method,[45] Kim's group rationally utilized the lateral flow assay (LFA)

method without an additional operation step to analyze cTnI.[44] The LFA strip consisted of different parts, including a sample pad, conjugate pads, nitrocellulose (NC) membrane, and an absorbent pad. After adding antigen cTnI to the sample pad, the flow would pass through conjugate pads which contained two different AuNP conjugates, and the cTnI reacted 1st anti-troponin I antibody bearing AuNP. In addition, the 2nd AuNP would also bound to the first AuNP through BSA and anti-BSA antibody interaction, which proved to demonstrate higher signal intensity comparing to conventional LFA method. With the sample flowing through the NC membrane, conjugated AuNPs were immobilized onto the surface. The color intensity was measured followed by dipping the cut LFA strip into troponin I containing well plates. Different concentrations of various troponin I from the patient samples were successfully determined by this novel LFA method, and the detection limit is as low as 0.01 ng/mL. Comparing to the Wu method, only 10 min is needed for the detection. The next year, another AuNPs based LFA immunoassay was developed.[62] One more test line was added to the NC membrane, which effectively achieves the simultaneous detection of different biomarkers. Both AuNPs based cTnI detection strategies are cost effective, especially for the Wu method,[45] which employed PDMS microchip, one of the most widely used cheap materials for making device. Also the portability of such small size lab chip would be helpful in future research of cTnI rapid and sensitive analysis.

1.2.3 Fluorescence Immunoassay

Fluorescence immunoassay is another form of optical biosensors. The first fluorescence immunoassay can be dated back to the year 1941 by Coons *et al.*.[63] Fluorescence organic dye and fluorescent nanoparticles are mainly used as signal

molecules to monitor the existence of target analyst. Various commercially available fluorescent assay based cTnI detection instrument (Table 1.2) can offer results within 20 min, such as Abbott i-STAT, Roche Cardiac Reader, and Singulex Erenna System. In 2006, Wu *et al.*[37] examined and modified the Zeptxtm system assay for cTnI detection. In this system, there contains flow immunoassays linked to a digital molecule-counting machine, and performed with a fluorescent tracer labeled either 96- or 384-well plate. Following washing, the remaining tracer would be sipped into the instrument. cTnI specific antibody and serum specimen, in a sandwiched format to create the photoassay, were pumped through a capillary into the instrument. Interrogation volume was established inside followed by directing a laser beam through the capillary. Fluorescence signal was able to be detected by the photo detector when the sample pass through the interrogation volume. Serum samples from patients were tested using this system in a pilot clinical study. High sensitivity with detection limit of 1.7 ng/L cTnI concentration was achieved, and the data also demonstrate the presence of AMI earlier than a conventional cTnI assay, but further confirmation by research with larger normal and diseased population with known clinical outcomes is needed. Although the commercially available cTnI assay is a lab-on-a-chip devices, and short time is needed with POCT, measurement at a time by these systems requires high initial and high maintenance cost. With regard to the cost efficient, the development of novel cTnI immunoassay is still desired.

TiO_2 nanotube array is an option to constitute a low cost biosensor. Shankar and co-workers[47] immobilized 16-phosphonohexadecanoic acid self assembled monolayer (SAM) onto a TiO_2 array (figure 1.2b). Comparing to direct physisorption or chemisorption,

alkylphosphonic and TiO_2 interaction is stable and durable. Anti-goat troponin antibody was coated onto the SAM monolayer via EDC/NHS coupling, such that cTnI could be captured onto the surface. The secondary anti-mouse troponin was labeled by a fluorophore. At last, the sandwiched structure formed by antibody-antigen-antibody was detected by the fluorescence signal. In this ultrasensitive platform without the help of enzymatic amplification, that as low as 0.1 pg/mL cTnI concentration detection was accomplished. However, the antigen-antibody recognition is a slow kinetically step. In this study, over two hours are required to complete the analysis. In another approach, long time antigen-antibody incubation process is also needed. The technique named total internal reflection fluorescence microscopy (TIRFM) adopted in the research is interesting. It is well known for its single-molecule investigation of cell membranes.[64] There are two types of TIRFM, one is prism-, and the other is objective-type. When a fluorophore is close to the metal surface, both of its electronic and optical properties will greatly change. Based on this metal quenching effect, the detection sensitivity can be enhanced. Lee and Kang[50] deposited gold onto the glass substrate, followed by immobilizing protein A, antibody, antigen, fluorescence labeled antibody, respectively. According to the distance between the fluorescent dye and the gold surface, the fluorescent dye was not greatly quenched, but adsorption of dye leaded to the quenching of its fluorescence. Therefore, such enhanced fluorescence was detectable. The advanced performance of the system is about 7000 times lower in the detection limit comparing to the conventional method. However, it is still a time consuming measurement.

Alkaline phosphatase (ALP) is broadly exploited for the fluorescent cTnI immunoassay,[33, 65-67] especially in the commercial products. Recently, Liu *et al.*[33] adopted

the ALP chemiluminescence chemistry for the cTnI detection. At first, monoclonal anti-cTnI was coated to the carboxylic acid modified magnetic beads via EDC coupling for the purpose of the specific antigen-antibody interaction. After adding the other ALP labeled cTnI antibodies, the excess of uncoupled ALP-antibodies were washed away by running the magnetic field, which leads to the proportional relationship between residual ALP and the cTnI concentration of the sample. Finally, 3-(2'-spiroadamantyl)-4-methoxy-4-(3''-phosphoryloxy)-phenyl-1,2-dioxetane (AMPPD) was introduced as the substrate for chemiluminescence of ALP. The combination of magnetic and fluorescence strategy is promising for the fast and sensitive cTnI detection. In addition, the treatment of AMPPD as amplification strategies is worth for further study to improve the detection limit.

Table 1.2 Analytical characteristics of commercial cardiac troponin I assays declared by the manufacturer[65]

Device	LOD (µg/L)	99th % (µg/L)	Detection Tag
Abbott i-STAT	0.02	0.08	ALP
Radiometer AQT90 FLEX TnI	0.0095	0.023	Europium
Alere Triage Cardio 3	0.01	0.02	Fluorophor
Roche E 2010/602 cTnI	0.16	0.16	Ruthenium
Siemens Dimension® EXL™ TNI	0.017	0.056	Chemiluminescence
Siemens IMMULITE® RxL CTNI	-	0.07	ALP
Tosoh ST AIA-PACK	-	0.06	ALP

In addition to the initiated fluorescence design, fluorescent nanoparticles is another option for assay fabrication. A rapid and sensitive fluorescent-europium (III)-chelate-dye-

nanoparticle based cTnI assay was made in 2012.[49] Streptavidin was coated onto microtiter wells, followed by conjugating biotinylated antibodies. The secondary antibody was covalently coupled to europium (III)-chelated-dyed nanoparticles. Then cTnI could be sandwiched into the two antibodies described above. After incubation and washing, the fluorescence generated by the europium was measured in a time-resolved mode. In both cases, the analytical time is approximately 40 min which is much better than the TiO_2 nanoarray and TRIFM strategies. Also the limit of detection can both reach to as low as 1 ng/mL.

Aptamer has recently been extensively studied and actively developed for the possible therapy and diagnosis of diseases. This is because its specificity and stability are usually superior to those of the antibodies. An aptamer is a single strand DNA (ssDNA) or RNA (ssRNA) or a peptide loop which can specifically recognize a wide variety of target molecules, such as chemical molecules, proteins, and even cells.[68] Due to the unique properties of aptamer, Dorraj *et al.*[41] most recently in 2015 selected an aptamer from a 79 bp single-stranded DNA random library that was used to bind the human cTnI from a synthetic nucleic acids library by systematic evolution of ligands exponential enrichment (Selex). Among the several aptamers they selected, TnIApt 23 showed best affinity in nanomolar range (2.69 nM) toward the target protein. Their experiment showed that the detection limit of using aptamer–AuNPs-based assay was found to be 5 ng/mL, but over 1 hour detection process is still a weakness for this method. Although the current detection limit of cTnI using aptamer is not as sensitive as the immunoassay methods, a much more sensitive aptamer and less time consuming will be soon developed due to the progress of Selex.

Recently microwave-accelerated and metal-enhanced fluorescence (MA-MEF) for protein detection was reported.[69] With the assistant of microwave-accelerate, only a few minutes are needed in the incubation process. In 2011, Aslan and Grell[48] applied this new technique to the cTnI detection. Silver nanoparticle films (SNFs) were freshly made on the amine terminated glass surface. Protein A was coated onto the surface for antibody immobilization in the next step. cTnI was then added and captured by the antibody on the surface. In the aid of microwave heating, the binding event only took 30 seconds. Finally, FITC-labeled antibody was conjugated with the cTnI by microwave heating for 30 seconds as well. During the fabrication, conjugation of antigen antibody processed rapidly with the assistance of microwave heating. What's more important, usual cheap kitchen microwave is capable for the whole incubation process, which is an excellent benefit for cost effective immunoassay construction. Another short time analysis design was made by Stringer *et al.*[46] for cTnI detection. Fluorescence resonance energy transfer (FRET) was utilized to build a sensing architecture (figure 1.2c). Quantum dots as a donor was attached to an capture antibody labeled acceptor by a bridge molecule protein A. When cTnI was bound to the antibody, the conformational change of antibody was initiated. The distance between donor and acceptor changed with this morphological change. In such a method, the shift in energy transfer was measurable. After adding the analyte cTnI, only 1 minute is demanded for the measurement. The potential of either strategies can see the promising future for the development of the cTnI detection.

In addition to the singly analyte immunoassay, multi-analyte chip assay is another option for biomolecule detection64-66.[70-72] The first CK-MB, cTnI, and Mb assay on an integrated optical waveguide was created by Plowman *et al.*.[73] Different biomarkers

including cTnI were sandwiched onto a multi-analyte sensor surface, and excited by a silicon oxynitride integrated optical waveguide. In such a multi-analyte platform, the simultaneous detection of several biomarkers and highly sensitivity make this type of biochips capable of being point of care testing device. Although ELISA-based assay, including colorimetric and fluorescent immunoassay, can detect cTnI rapidly with high sensitivity, multiple experimental steps are involved, and they are a also time-consuming process.

1.2.4 Paramagnetic Immunoassay

Paramagnetic particles (PMPs) have seen its applications in many areas, such as MRI contrast agents and biomolecules separations.[74, 75] Typically, PMPs consist of an iron oxide core with a high biocompatibility layer outside. The first proposed PMPs for binding assay was made in 1970s.[76, 77] Since then magnetic nanoparticles widely used as a carrier for biomolecules detection, and prove to be able to increase the rate and the sensitivity.[78, 79] Majority of PMPs based immunoassay involves the antigen-antibody sandwiched structure formation on its surface with PMPs being a reaction label. Generally, reagents containing PMPs and antigen are added into a chamber in which the bottom surface is coated with antibody. Antibody attached PMPs can capture the antigen, and by the driving force generated from the bottom magnetic field, antigen can be transported to the bottom surface rapidly. The unbound PMPs is washed away by the top magnetic force in the chamber. By characterizing the bottom reacting surface, the antigen is able to be detected successfully.

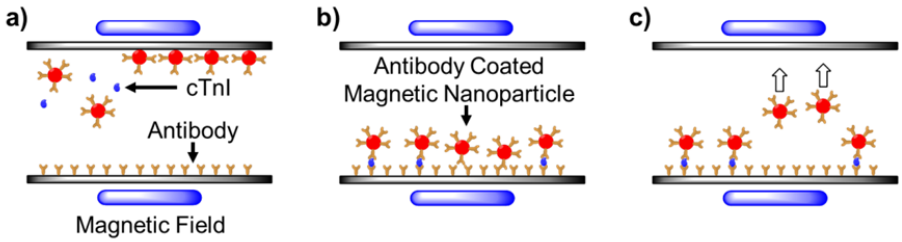

Figure 1.3 a) cTnI and antibody coated magnetic nanoparticle were mixed in the channel. b) cTnI were captured by the antibody on the bottom surface, also sandwiched by the antibody coated magnetic nanoparticle. c) Unbounding particles was washed away by the upper magnetic fields.[51]

Prins' group[51] designed a multiplexed cTnI immunoassays exploiting actuated PMPs (figure 1.3). At first, antibody coated magnetic nanoparticles were mixed with the sample to capture the cTnI analyst. Due to the large total surface area of the particles, the binding was able to run fast and efficiently. In the next step, the mixed solution passed through the cartridge by the driving force of electromagnets. In such a way, the particles can also help concentrate the captured analyst on the binding surface, which leads to a less time consuming incubation process. Finally, unbound and weakly binding particles would be washed away by the magnetic fields generated from the upper surface. Since the cTnI concentration is proportional to that of the magnetic nanoparticles, the reflected light intensity from the surface is capable of sensing cTnI, by the mechanism of frustrated total internal reflection. With the combination of magnetic technique and optical detection, rapid and highly sensitive with a limit detection of 0.03 ng/mL cTnI is achieved. Moreover, Kiely *et al.*[52] developed another novel PMPs immunoassay based biosensor. The advantage of it over the former method lies in no extra washing or other post operations procedures. The alternative approach relies on the presence of the PMPs in the sample to cause the increase of the coil inductance which leads to directly determination

by using a bridge circuit. To accomplish the sensor construction, two reaction coil surfaces, one for detection and the other for reference, were mounted onto the substrate. In order to detect the PMP and enhance the binding process, an electromagnet was placed under the substrate. A pair of antibodies for cTnI were immobilized onto detection coil surface and the surface of PMP, respectively. After adding the cTnI samples to the device, cTnI was sandwiched between the PMP and the surface. Due to the significant influence of PMPs on the magnetic field, cTnI can be detected. The whole process finished within 4 min, and high sensitivity with recognizing 0.5 ng/mL cTnI was achieved in this study.

Comparing the paramagnetic assay and optical immunoassay (colorimetric and fluorescent assay), the main challenges for optical immunoassay are the inherent opacity and autofluorescence.[34] To circumvent such a problem, paramagnetic assay is more suitable in clinical diagnostics because of the nonmagnetic properties of surrounding biological parts. In addition, PMPs can play a role as not only mixing the reagents, also a transportation for the antigen to be delivered onto the surface rapidly. In another combination of magnetic and optical approach to rapidly detect cTnI with high sensitivity, Todd *et al.*[38] achieved LOD of 0.6 ng/L with a dynamic range of >435 logs using single molecule counting technology based Erenna Immunoassay System. Streptavidin modified PMPs were attached to fluorescent dye labeled cTnI by streptavidin-biotin chemistry. MPs were separated by a magnetic bed after incubating samples in a 96-well plate. Before measuring, urea was utilized to disrupt antibody-analyte interactions to release the cTnI from the MPs. For the Erenna Immunoassay System, samples were pumped through a interrogation space contained capillary flow cell. Light reached the interrogation space after passing through a dichroic mirror and a confocal microscope lens. When dye labeled

cTnI passed by, emitting fluorescent light could be measured by the confocal microscope lens and the detector.

1.2.5 Electrochemical Immunoassay

Electrochemical assay based biosensors mainly rely on the interaction between transducer and target molecules. It is operated by the detection of an electrochemical signals from the specific reaction. When captured by the immobilized surface antibody, charges exchange occurs between host and guest molecules, leading to the change in the current or voltage on the localized surface. Thus, based on the operating principle, the electrochemical biosensor can convert the chemical information into a measurable electrical signal.

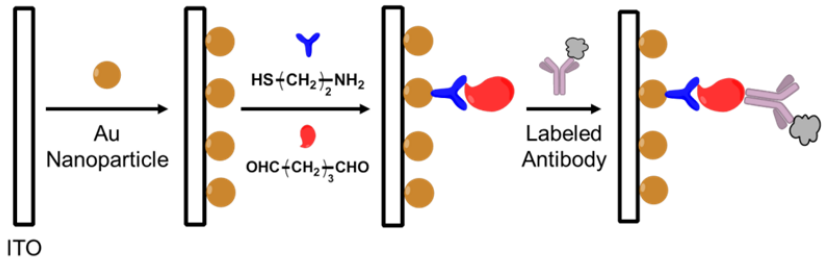

Figure 1.4 HRP labeled antibody was linked to the gold nanoparticles by glutaraldehyde molecule.[28]

Use of nanoparticles in the electrochemical biosensors has drawn much attention to the scientists over the past years. Variable novel cTnI detection platform by using nanoparticles has been reported. In 2011, Ahammad *et al.*[28] designed a highly sensitive cTnI biosensor (figure 1.4). At first, the ITO surface was modified by depositing AuNPs. Different linkers including cystamine and glutaraldehyde were chemically attached to the AuNPs through self-assembly method. Then the anti-cTnI antibody were immobilized

onto the AuNPs-modified ITO electrode surface by linker molecules. In such a method, the cTnI could be captured onto the AuNPs-ITO electrode. Meanwhile, the secondary anti-cTnI antibody was labeled by horseradish peroxidase (HRP) enzyme which can be used to catalyze H_2O_2 reduction. Finally, the sandwiched structure can be a powerful nanohybrid to detect the concentration of cTnI by measuring the changes of open circuit potential during H_2O_2 electroreduction. HRP is a common label for the detection technology. Comparing to the HRP strategies employed in the optical immunoassay, more incubation time was consumed in this method, though the high sensitivity of 1 ng/mL was achieved. Recently, Shan *et al.*[30] developed a cTnI biosensor showing a higher sensitivity of 0.4 pg/mL. Two specific peptides were used as capture peptide and report peptide, respectively. Gold nanoparticles, again utilized as amplification platform, were electrodeposited onto the gold electrode. Capture peptide was self assembled onto the gold nanoparticles via the well studied thiol-gold reaction. The report peptide was labeled with ruthenium contained molecule at lysine via acylation reaction. After incubating the electrode with cTnI and the probe peptide, the response was electrochemically generated.

One concern about fabricating the biosensor for clinical diagnostics is the smaller sample size. Recently, microfluidics has been applied in different areas, such as cellular behavior, optics, and sensing chips.[80, 81] The intrinsic feature of miniaturization of the microfluidic system can help overcome the limitation of conventional immunoassays. What's more, the microfluidics can be integrated into various immunoassay. Recently, a methodology was developed based on AuNPs-Poly(Dimethylsiloxane) (PDMS) composite microfluidic systems.[54] PDMS was cured with a series of holes on the

substrate, followed by adding $HAuCl_4$ aqueous solution to the hole to obtain GNP contained microreactor cells. The anti-cTnI antibodies were absorbed in each microreactor well to capture the cTnI. The secondary antibody was labeled by CdTe and ZnSe quantum dots (QDs). After the sandwiched structure formed in the localized surface, QDs were dissolved, and Cd^{2+} and Zn^{2+} could be detected by square-wave anodic stripping voltammetry. This immunosensor demonstrates the success of integration of microfluidics with electrochemistry to detect cTnI for clinical application. However, it is well known that QDs are toxic materials, and also a label-free method is more welcome in the cutting edge science today. In 2012, Bhalla *et al.*[55] developed a unique label free cTnI biosensor based on the principle that electrical capacitance at the electrode surface changes with the binding of highly charged antigens. In this study, negatively charged citrate-capped AuNPs were electrodeposited on the electrodes using bulk electrolysis technique. The specific anti-cTnI antibodies were coated onto the gold matrix. Since the electrical capacitance increases at the electrode surface with the binding of cTnI and anti-cTnI antibody, cTnI can be detected.

Platforms using carbon nanomaterials have recently been used for the detection of cardiac biomarkers with superior sensitivity. The current limits of common sensing platforms include long duration of assay processing, expensive equipment and use of highly toxic or fluorescent labels. Periyakaruppan *et al.*[40] have recently reported a simple, inexpensive, and label-free method to detect biomarker troponin-I using vertically aligned carbon nanofiber (CNF) based nanoelectrode arrays. The anti-cTnI Ab was first immobilized on CNFs, and the detection of human-cTnI in assay was achieved by using electrochemical impedance spectroscopy and cyclic voltammetry techniques. The signal

changes in electrical capacitance or resistance were due to the specific adsorption of Ab–Ag interaction. The sensing system demonstrated a good selectivity and high sensitivity against human-cTnI analytes with the lower limit detection at 0.2 ng/mL cTnI concentration.

Similar to the paramagnetic immunoassay, the electrical biosensors can overcome the limitation of inherent opacity and autofluorescence in colorimetric and fluorescence immunoassay. Electrochemical based biosensors can also provide highly sensitive and rapid sensing platform, making it a promising protein detection tool. However, the detection environment, including the pH and ionic strength can disturb the sensing results. In some cases, the electrochemical technique can not provide reliable specific binding affinity due to the antibody isolation problem.[70]

1.2.6 Surface Plasmon Resonance

Besides colorimetric assay, fluorescence immunoassay, paramagnetic immunoassay, and electrochemical immunoassay as mentioned above, surface plasmon resonance (SPR) has emerged as a new optical detection component of biosensors by measuring changes in the index of refraction upon adsorption.[82] This technique enables rapid detection of the unlabeled proteins with a simple optical apparatus. In 2004, Masson *et al.*[39] reported a fiber-optic-based surface plasmon resonance sensor for cTnI detection in HEPES buffered saline solution. Antibodies specific to cTnI were attached to a carboxymethylated dextran layer on a gold SPR surface. The constructed sensor had a lower detection limit of 1.4 ng/mL. Compared with other methods, the advantage of their sensor was that the probe surface with antibody attachment was stable for a few weeks in a wide pH range (pH 2–12). Kwon *et al.*[57] recently constructed an SPR-based cTnI sensor

by crosslinking a monoclonal antibody as an epitope peptide onto a chemically modified thin gold film. The performance of the sensor was determined by examining the SPR signal intensity against cTnI concentration. They found that the SPR signal intensity was directly correlated to the cTnI concentration in the range of 0–160 ng/mL. The lower detection limit of the sensor was 0.068 ng/mL cTnI, which was comparable to ELISA-based commercial cTnI detection systems according to the statement of the author in the paper.

In particular, gold nanoparticles with elongated shape (*i.e.* gold nanorods) have attracted much attention for in the field of SPR application due to the fact that their highly anisotropic shape exhibits much different optical properties from those spherical gold nanoparticles.[83] Using anti-human cTnI immunoassay on gold nanorods, Guo *et al.*[58] reported a convenient and rapid method for human cTnI detection in solution by SPR. The sensing was based on changes of longitudinal localized SPR signal induced by specific binding between cTnI antibody and cTnI. Although the detection limit of this method was quite high (10 ng/mL), this study was the first report of taking advantage of gold nanorods for sensing cTnI, which was more sensitive for detecting compared with that of spherical AuNPs.

It is essential to diagnosis of the cardiovascular diseases at the early stage, in order to operate successful treatment for recovery of patients. Cardiac troponin I (cTnI) has proven to be a significant biomarker for acute myocardial infarction (AMI). Therefore, it is important to develop a rapid, sensitive, and POCT cTnI biosensor to assist the diagnosis of AMI at very low concentration (less than 0.5 ng/mL) in the whole blood. This review has hoped to demonstrate numbers of research with regard to the detection of

cTnI for AMI. Despite the significant developments in the field, no ideal device has been used for clinic application. The big challenge for the technology is the limit detection and POCT measurement which includes small bench top device and hand-held instrument. Future cTnI detection technology can be directed towards 1) miniaturization of portable, sensitive, highly specific biosensors, 2) shorter analytical time evaluation including more efficient incubation process, 3) cost efficient, 4) POCT measurements, and 5) immunoassay suitable for multianlyte detection. Combination of all the features with continuous efforts, the next decades will see the breakthrough in the field of cTnI as a biomarker for AMI diagnostics at the early stage.

1.3 Interactions between Carbon Nanomaterials and Biomolecules

Carbon, present in all forms of organic lives, serves for human in different aspects for centuries, such as coal which is the main source of energy. When the size scales to nano level, carbon nanomaterials and their colloids exhibit extraordinary properties in terms of electrical,[84] thermal,[85] chemical,[86] and mechanical,[87] and own a unique place in nanoscience technology. Three different dimensions, including zero dimension, one dimension, two dimension, are the basic forms of carbon nanomaterials. This contains carbon dots (C-Dots), fullerene, carbon nanotube (CNT), graphene, and graphene oxide (GO) which is a graphene based material. Although these nanomaterials mainly consist of only one element carbon, different structures of it show the extraordinary properties. In addition to the architecture itself, the colloids whose solute particle size ranges from 10^{-9} m to 10^{-6} m obtained from the carbon nanomaterial demonstrate excellent functions as well.[88] C-Dots mainly act as nonmetal quantum dots, and demonstrate promising potential in the development of bioimaging[89] and other clinic applications[90] owing to its

excellent biocompatibility[91]. Fullerene is a sphere shaped carbon nanomaterial. The fullerene-biomolecule conjugates are widely investigated for the purpose of medical applications.[92] The special structure of the CNT indicates high sensitivity and fast response for the reaction at its interface when used in the fabrication of nano electronic devices.[93] A variety of CNT-based nanomachines have been built for biosensing applications. Graphene was recently experimentally isolated but may have been used for centuries, and regarded as the newest carbon nanomaterials. Since its discovery in 2004,[94] it has drawn much attention in chemistry and material communities. GO, as one of the graphene based materials, has been investigated a lot in the area of biomedical field as well.

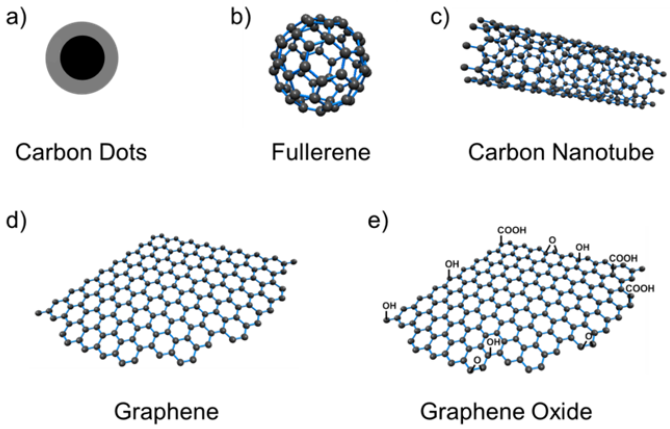

Figure 1.5 Zero dimensional carbon nanomaterials, a) carbon dots, and b) fullerene. One dimensional carbon nanomaterial, c) carbon nanotube. Two dimensional carbon nanomaterial, d) graphene, and e) graphene oxide.

Biomolecule, associated with metabolism, consist of any molecule, including protein, carbohydrate, lipid, DNA, and other big or small molecules, present in the living

organism. The biomolecules show an influence on metabolism in different ways. Acute myocardial infarction (AMI) is one clinical form of the cardiovascular diseases. When the person is diagnosed with it, a protein named cardiac troponin I (cTnI) will be released into the blood. Such that cTnI is believed to be the gold standard biomarker for AMI.[95] In addition, carbohydrate growing on the cell surface also plays an important role in metabolism. Many biological processes, such as cell-cell adhesion and protein folding, take place as a result of saccharides on the surface of the cell.[1, 96] To overcome the obstacles and make more achievements in solving diagnostic and therapeutic biomedical problems, many efforts have been devoted to the research in the field of biomolecules. With its novel features, the family of carbon nanomaterials has been widely investigated with its function in the biomolecule activity, and shows growing biomedical applications. In this paper, different groups of carbon nanomaterials, including zero dimensional, one dimensional, two dimensional nanomaterials, will be discussed based on their interactions with biomolecules.

1.3.1 Zero Dimensional Carbon Nanomaterials

Carbon dots (C-Dots), zero dimension nanomaterials, have recently attracted much attention due to its unique properties, such as low cytotoxicity, high photostability, magnificent biocompatibility, and easy conjugation with biomolecules.[89] A myriad of synthesis strategies have been developed to fabricate C-Dots. Oxidative acid treatment is generally used to obtain C-Dots. Liu *et al.*[97] prepared C-Dots from the combustion soot of candles. Polyacrylamide gel electrophoresis was utilized to purify the C-Dots. The quantum yield (QY) of the C-Dots was relatively low, with the highest value of 1.9%. Laser irradiation method for C-Dots fabrication was reported by Hu *et al.*.[98] This study

opened a new way to prepare C-Dots.[99] Graphite powders was irradiated at first. After boiling in perchloric acid, mixing with PEG, centrifugation, and separation, C-Dots were obtained. The QY yields vary from 3 to 8%. Zhai *et al.*[100] reported a microwave-assisted pyrolysis method. Citric acid, the carbon source, and various amine contained molecules, which are used for surface passivation agent, were utilized for the C-Dots synthesis. The photoluminescent (PL) QY was 30.2%, and it is comparable to the common fluorescent quantum dots. Electrochemical exfoliation is another way to prepare C-Dots. Li *et al.*[101] used graphite rods as anode and cathode, with NaOH and EtOH as electrolyte, and the intensity of the current was 10-200 mA/cm^2. Alkaline environment is important for this approach. In 2013, Zhu *et al.*[102] employed hydrothermal method to form C-Dots. Polymer shaped C-Dots were prepared by condensing citric acid and ethylenediamine. Then it was carbonized to form C-Dots. Different characterizations, including transmission electron microscopy (TEM), atomic force microscopy (AFM), Raman microscopy, NMR spectroscopy, and other techniques, were applied. The QY was as high as 80%, which is suitable for industrial production.

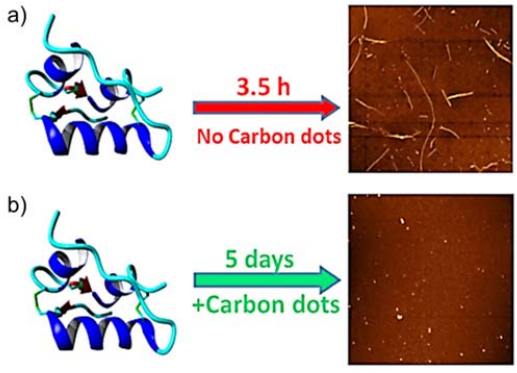

Figure 1.6 a) Without carbon dots, insulin will fibril within 3.5 h. b) By the function of carbon dots on insulin, the fibrillation is inhibited within 5 days.[103] (Reproduced with permission from reference 103. Copyright 2015 American Chemical Society)

Recently, the effect of C-Dots on protein fibrillation was investigated for the first time (Figure 2).[103] Human insulin was selected for the study. Different characterizations, including UV-vis, Fourier transform infrared (FTIR) spectroscopy, X-ray photoelectron spectroscopy (XPS), atomic force microscope (AFM), and transmission electron microscopy (TEM), were performed for the C-Dots prepared from carbon powder. The non-toxic property of C-Dots was demonstrated by incubating it with sea urchin embryos. To monitor the kinetics of human insulin fibrillation, thioflavin T (ThT) fluorophore was used. In addition, circular dichroism (CD) and AFM were applied over different periods of the fibrillation process. According to the fluorescence study, three stages, including lag phase, elongation phase, and saturation phase, were observed. That the interaction between C-Dots and human insulin at the early stage makes the C-Dots inhibit human insulin fibrillation was proposed in the paper. The study displays the inhibiting effect of C-Dots on human insulin fibrillation, and shows the great potential of C-Dots in application of biological systems.

The potential application of C-Dots for bioimaging was studied by Sun *et al.*[104] for the first time. The C-Dots were produced by laser ablation method with argon as carrier gas. The products did not exhibit photoluminescence until the surface was passivated by attaching organic molecules, and the observed QY ranged from 4 to 10%. The mechanism of C-Dots photoluminescence was also discussed, which is attributed to the surface energy traps as a result of surface passivation. Two-photon fluorescence materials, such as CdSe quantum dots, have promising applications in bioimaging. However, due to the heavy metal contained, the two-photon fluorescence materials have caused serious problems, including hazard on human health and environment. Sun and co-workers[105]

moved on to investigate C-Dots for the function of multiphoton bioimaging. The same set up as the previous one was performed to characterize the C-Dots. Human breast cancer MCF-7 cells were cultured to demonstrate the potential of C-Dots in cell imaging by two photon luminescence microscopy. This study shows great capability of C-Dots in bioimaging, and comparable to the best performing semiconductor quantum dots. In 2009, Sun and co-workers[106] discussed the use of C-Dots for in vivo and in vitro applications. In the study, the PEGylated C-Dots were found to show strong fluorescence both in aqueous solution and on the surface. Human breast cancer MCF-7 and human colorectal adenocarcinoma HT-29 cells were utilized for the C-Dots toxicity assessment in vitro, and nontoxic property of C-Dots, comparing to other heavy metal contained quantum dots, were concluded. The toxicity evaluation of C-Dots in vivo were investigated by using CD-1 mice, and these fluorescence nanomaterials demonstrated nontoxic to the selected cell lines. Based on the results, C-Dots showed competitive bioimaging functions to the commercially available heavy metal bearing quantum dots both in vitro and in vivo applications. Tao *et al.*[107] utilized C-Dots for vivo imaging in the near-infrared (NIR) region for the first time. The C-Dots were obtained from the modified traditional method of using mixed acid to oxidize carbon nanotubes and graphite. AFM, FTIR, UV-Vis, and fluorescence microscopy were employed separately for C-Dots characterizations. The in vitro cytotoxicity of C-Dots was tested by incubating C-Dots with the human kidney embryonic 293T cell line. In vivo fluorescence imaging and in vivo bio-distribution were demonstrated in mice over time. This work shows the promising application of C-Dots in biomedical imaging.

Fullerene, discovered at Rice University in 1985, was another zero dimension carbon nanomaterial.[108] Since then research regarding to fullerene-biomolecule conjugates, besides the field of solar cell,[109] has drawn much attention. Fullerene is a sphere shaped molecule, and unable to dissolve in water which limits its applications in biotechnology.[110] Due to this reason, water soluble fullerene derivatives are largely needed. The landmark work was the one performed by Friedman *et al.*[111] in 1993. With the model built via the program DOCK3, that the active site of HIV-1 protease (HIVP) was able to host fullerene derivatives was found. In addition, the inhibition function of the fullerene derivatives to the HIVP was examined experimentally. Followed by this work, numerous efforts were devoted to the field of fullerene biomedical applications, including attaching amino acides and peptides to the fullerene for the applications in the neural diseases,[112] binding DNA to the fullerene for the use of breaking DNA,[113] and immobilizing carbohydrate onto the fullerene for photodynamic therapy[114]. Nowadays research with regard to the field of fullerene-biomolecule is still active, and more applications of fullerene also needs to develop.

1.3.2 One Dimensional Carbon Nanomaterials

Carbon nanotubes (CNTs) are important one dimensional nanomaterials which have a cylindrical nanostructure.[115] The CNTs length to diameter ratio could be up to 108.[116] In 1991, Iijima reported a similar method to producing fullerene to prepare CNTs.[117] The CNTs were obtained on the negative carbon electrode via arc-discharge method. In addition, different synthesis strategies have been developed to construct the CNTs, such as laser ablation,[118] and chemical vapor deposition[119]. The needle shaped carbon

nanomaterial shows excellent properties like fullerene, and have been investigated by numerous researchers for the valuable applications in the field of nano-biotechnology.

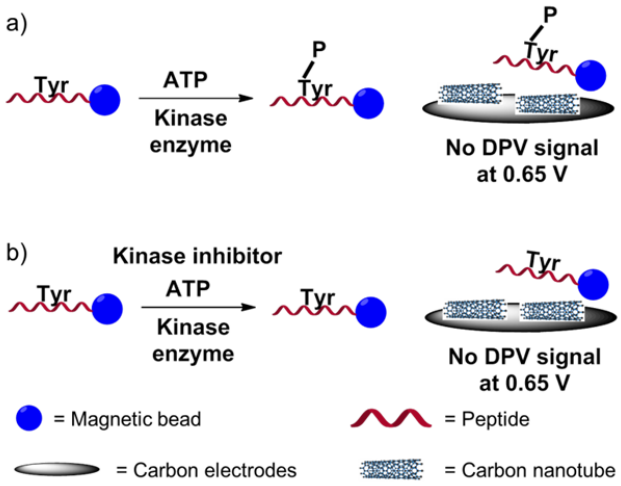

Figure 1.7 a) Differential pulse voltammetry (DPV) was suppressed after the phosphorylation of Tyrosine (Tyr) in the peptide residue b) The oxidation current signal was recorded in the presence of kinase inhibitor which is able to prevent the phosphorylation of Tyr in the peptide residue.[120]

In 1974, individual molecules were introduced into electronic devices for the first time.[121, 122] Since then molecular electronics attracted much attention, due to the high sensitivity, fast response, and low detection limits.[123] Carbon nanotubes are capable of decreasing over-potential and improving sensitivity when incorporated into electronics. Variable CNT-based devices have been fabricated to detect biomolecules, such as proteins, DNA, and others.[124] In CNT-based field effect transistor (FET), the CNT which can provide faster electron transfer kinetics plays a role of channel, and the charge of biomolecules like protein bind to the device followed by serving the gate for the current flow.[125] In 2007, Kerman *et al.*[120] studied the effect of protein tyrosine kinases (PTKs) on

the phosphorylation of the tyrosine (Tyr) residue of the protein (Figure 1.7). A multi-walled carbon nanotube was coated to the electrode to improve the detecting sensitivity. A small molecule, 4-amino-5-(4-chlorophenyl)-7-(tert-butyl)pyrazolo[3,4-d]pyrimidine, was used for the phosphorylation inhibition process. That the phosphorylation could prevent phosphorylated Tyr oxidizing at approximately 0.65V was concluded. It was concluded that phosphorylation could prevent phosphorylated Tyr oxidizing at approximately 0.65 V. The research is important for the pharmaceutical development, since PTKs is related to cancer. Another CNT-based FET was built by Wang and Musameh.[126] The results confirmed the CNT could accelerate the electron transfer kinetics. The CNT modified electrode showed high sensitivity and stability to insulin sensing by amperometric measurements.

More interestingly, CNTs could be internalized by the cell via tip recognition and rotation according to the report by Shi *et al.*.[127] With the aid of computer based model and experiments, they found that the receptor on the cell membrane could bind to the tip of CNT. In such a way, the CNT is capable of entering the cell, and providing a new approach to send the cargo attached to the CNT into the cell for therapeutic applications. CNT can also be used in energy storage. Lee and Lee[128] studied the potential of CNTs in hydrogen storage through density-functional calculations. Two different sites for H_2 chemisorption were found inside the empty space of CNT. The storage capacity of over 14 wt% (160 kg H_2/m^3) were predicted in the paper. However, the experimental reports with regard to the CNT-hydrogen storage can not achieve such a high level.[129] Chen *et al.*[130] utilized the aligned CNT for hydrogen adsorption study at room temperature under 10 atm pressure. The capacity of storage could only get 5-7 wt%, which is much smaller

than the computational study, but the pretreatment by heating samples to 300 ^{o}C could increase storage capacity up to 13 wt%.

1.3.3 Two Dimensional Carbon Nanomaterials

Graphene is an atomically thin and two dimensional carbon nanomaterials. Since its first experimental discovery in 2004,[94] graphene has gained lots of popularity in biological systems and applications of therapeutic properties due to its unique structure, such as extremely large surface area on both sides and one atomic thickness. To improve the sensitivity of biosensing system, graphene has been widely used to fabricate more efficient nanodevices. As a novel semiconductor, graphene shows extraordinary properties comparing to conventional industrial materials, such as silicon. For example, there exists many electron collisions when current flow flows through silicon, which limits its wider applications. Not only its fantastic electronic properties, graphene is an outstanding conductor of heat, and also the world's thinnest and strongest material. However, unlike other semiconductor materials, there is no band gap between conduction and valency band in graphene, bringing up problems for fabricating nano electronic devices. For graphene based transistors, once the device is turned on, it is hard to be switched off. To overcome such obstacles, many groups are trying to modify the graphene to open up the band gap in graphene, thereby improving the sensitivity of the nano bioelectronics. Covalently[131] and non-covalently[132] bonded strategies are generally adopted to solve the problem. Recently, Mann *et al.*[132] developed a method to modify the graphene via the aromatic moieties by non-covalent strategy. The approach studied in this paper can provide promising applications in the field of sensing and biosensing. Graphene oxide (GO) is a derivative carbon material of graphene. It contains carboxyl

groups at the edges, hydroxyl and epoxide groups mainly at the basal plane, and some carbon sp^2 domains. Such different oxygen containing groups provide more active reacting sites to link the molecule to the surface via covalent or non-covalent bound strategies. In 2009, Lu *et al.*[133] immobilized dye labeled ssDNA onto the GO via the ionic interaction (Figure 1.8). Since the small distance between the probe DNA and GO, the conjugated organic dye was quenched after deposition. The restoration of dye fluorescence proved the detection of target DNA, which is due to its interaction with the released DNA from the GO.

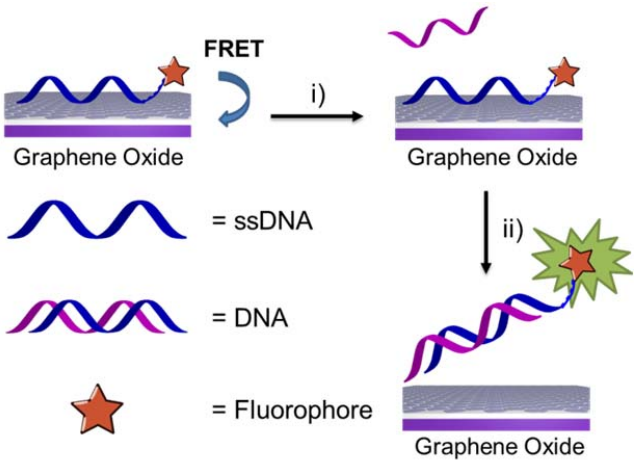

Figure 1.8 i) Fluorophore attached DNA was absorbed onto graphene oxide, and its fluorescence was quenched because of Förster resonance energy transfer (FRET). ii) Specific sequence ssDNA was added to the surface, which leads to the fluorescence restoration.[133]

To understand the roles of GO in interacting with biomolecules, Li *et al.*[134] studied the effect of GO as a quencher on the fluorescent assay of amino acids, peptides, and proteins. The work started with the fluorescence quenching of L-Tyrosin (Tyr) and L-tryptophan (Trp) by GO. That the hydrophobic interaction and electrostatic interaction

between amino acids and GO could contribute to the quenching effect was concluded in the study. Also the quenching mechanism was discussed, and it was attributed mainly to the static quenching. To test the fluorescence quenching of peptides and proteins by GO, amyloid β-protein 40 (Aβ 40), human islet amyloid polypeptide (hIAPP) and bovine serum albumin (BSA), human serum albumin (HSA) were selected separately for the investigation. The work deeply addressed the interaction between GO and biomolecules, and is important before applying GO to actual applications. GO can also be used for the selectivity and sensitivity enhancement. Followed by this study, the influence of GO on the determination of Trp was studied.[135] Different parameters including pH, temperature, incubation time, and chemical reagents were screened to optimize the conditions. By oxidizing the products from reaction of formaldehyde and Trp with the hydrogen peroxide, the selectivity and sensitivity were enhanced in the presence of GO.

One important issue when applying GO to biosensing system is that the selective detection of a specific protein from a biological fluid which contains various proteins. To examine the interaction between lysozyme, which exist abundantly in body fluid, and GO for biosensing, Li *et al.*[136] demonstrated the strong and selective adsorption of lysozyme on GO. The strong quenching effect of GO on lysozyme confirmed the lysozyme and GO interaction, and this interaction was further characterized by zeta potential, dynamic light scattering (DLS), and AFM. The nature of the interaction was determined to be electrostatic interaction. After lysozyme adsorpted onto GO, that adding pH 11.5 NaOH and precipitating it with $CaCl_2$ could release lysozyme from the GO surface. What's more, their strong interactions made lysozyme from binary and ternary protein mixtures adsorpt onto GO as well. This study well addressed the fundamental problem, selective

detection of abundant proteins, for the further development of GO based diagnostics approach.

Besides peptides and proteins, the interaction between GO different lipid models were also investigated by Li *et al.*.[137] To understand how the GO acts in the interaction with lipids, the Langmuir monolayer was used, and five different lipids with the same alkyl chain but different head groups were selected. The results showed that it is electrostatic interaction that governed the lipids and GO interaction. An "edge-in" orientation of GO was proposed for inserting GO into lipids.

The interactions between biomolecules and carbon nanomaterials offer an excellent chance for the chemists and material scientists to dig into the field of nanobiotechnology. A myriad of new discoveries in terms of carbon nanomaterials with biomolecules have been made in the past decades. From the views of different forms of carbon nanomaterial, recent developments and practical biomedicine applications were briefly summarized. Not only fibrillation inhibition function of carbon quantum dots, also bioimaging ability of these nano sized carbon dots shows great potential in practical applications. Fullerene, another style of zero dimensional carbon nanomaterial, conjugated with other biomolecules also attracts much attention due to the special properties. The one dimensional nanomaterial carbon nanotube (CNT) is usually employed for the biosensing system. The high sensitivity from CNT based nanobioelectronics gains its highly popularity. Graphene was recently discovered, but graphene itself and its derivate such as graphene oxide have been the hot topic in the area of biotechnology. Research regarding to the interactions between these graphene based materials and biomolecules harvested much in the past decades. Although the carbon in its nano scale shows unique properties,

challenges including biocompatibility and cost efficiency, coexist with opportunities. More and more new sightings still need to be discovered.

Chapter 2 A Resorcinarene for Inhibition of Aβ Fibrillation

2.1 Background

Alzheimer's disease (AD), the most common form of dementia, causes progressive memory loss, behavior, and thinking problems.[138, 139] It has become a major threat for human beings around the globe. Approximately 24.3 million people suffer from AD in the world nowadays.[139, 140] In accordance with a recent report,[141] the number of the AD patients is expected to increase up to 81.1 million by 2040. Over the past 30 years, the etiology of the disease has been attributed to the accumulation of the extracellular plaques, which are mainly composed of amyloid-β peptides (Aβ), and intracellular tangles formed by tau proteins.[6, 142] Much scientific research[142-147] has proven that sequentially cleavage of amyloid precursor protein (APP) by BACE1 and β- and γ-secretases can produce Aβ monomer, and the aggregation of Aβ monomer into amyloid fibrils is strongly associated with AD.[148] In other words, Aβ plays a central role in the pathogenesis of AD. Both Aβ 42 and Aβ 40 are primary isoforms of Aβ, where Aβ 42 is considered as the most toxic form,[149] and Aβ 40 is the most abundant form.[150] The development of therapeutic agents targeting upstream secretases had been unsuccessful.[151] Thus the development of an inhibitor for early stage Aβ fibrillation could be a promising treatment of AD.[152]

The major Aβ contains 40 or 42 amino acids with residues from 18 to 42 forming two parallel β sheets.[153] Significant efforts and progress have gone into developing new amyloid fibrillation inhibitors. Aβ fibrillation inhibitors are mainly designed in two different ways: peptides or peptide mimetics[154-158] and organic compounds.[145, 159-162] However, the challenge to design small molecules for Aβ fibrillation is because protein-

protein interaction regions, approximately 20 nm^2, are larger than the protein-small molecule interaction regions which are around 3-10 nm^2.[163] Most small molecules, therefore, cannot afford adequate steric hindrance to prevent the aggregation. Supramolecular strategy to block the aggregation process exhibits another option for potent AD therapies. Lee *et al.* have demonstrated such a strategy by using cucurbit[7]uril (CB[7]).[164] However, the efficiency of the designed inhibitor is low. More inhibitors – the reported lowest effective concentration ratio of the inhibitor to Aβ 42 is approximately 100 – to prevent amyloid fibrillation are needed (Table 2.1). In addition to less powerful performance on blocking Aβ aggregation, the cytotoxicity of Aβ 42 fibrils cannot be delayed or inhibited by most other designed inhibitors (Table 2.1). It is, thus, in dire need to develop inhibitors with sufficient potency to delay the onset of Aβ fibrillation and cytotoxicity of Aβ 42.

The utility of resorcinarene has expanded greatly in the field of supramolecular chemistry and biochemistry.[165-167] Not only the semi-rigid structure and the π-electron rich cavity, but also the hydrogen bonding sites of the molecule, provide an excellent platform for the host-guest complexation.[1, 168] These compounds can be functionalized in diverse manners for different applications, such as recognition of amino acids as well as delivery tool in pharmacology.[169-171] Inspired by such vital applications in host-guest chemistry, we turned to the functionalized resorcinarene as a potential strategy towards the inhibition of Aβ amyloid fibrillation for the first time. Figure 2.1 shows the Aβ fibrillation pathway, where the partial denaturation of the peptide monomer initiates the fibrillation route. The denatured monomers self-assemble into oligomers and in turn form fibrils via protofibril formation. In a set of sequential events, resorcinarene is expected to

interact with Aβ in a way that increases the steric hindrance for fibril aggregation and abolishes the Aβ fibrillation process which may delay the toxic Aβ 42 as well. Herein, we studied such a hypothesis by experimental method, including thioflavin T (ThT) binding assay, circular dichroism spectroscopy (CD), atomic force microscopy (AFM), and cytotoxicity assay, as well as theoretical approach using docking calculations and MD simulations. These results demonstrate a great potential application of resorcinarene in retarding Aβ fibrillation, and propose a new possibility for further optimization of the inhibitor design. In particular, resorcinarene as a delivery system with recognition and encapsulation properties will emerge as a promising agent for therapies of Alzheimer's disease.

Table 2.1 The comparison of different inhibitor towards blocking Amyloid β-protein aggregation

	Molecule	**Aβ 40**[a]	**Lag Time**	**$t_{1/2}$**[b]	**Aβ 42**[a]	**Lag Time**	**$t_{1/2}$**[b]	**Cyto toxicity**[c]
Supra molecule	Ours	0.1	~240	~480	0.1	~360	~1200	Yes
	Cucurbit[7] uril[164]	10	~120	~150	100	< 60	~100	Yes
	CLR01[162]	-	-	-	1	-	-	-
Peptide	LK7[157]	-	-	-	0.5	< 60	360	Yes
	NV[172]	-	-	-	1	-	-	Yes
Small molecule	DC-AB1[173]	-	-	-	200	-	-	-
	Catechol derivative[174]	-	-	-	1	-	-	-
	Tanshinones[161]	-	-	-	1	-	-	-
Metal Chelator	Aromatic co-ligands[159]	0.1	-	-	-	-	-	-
	HL3 and HL4[160]	6	-	-	-	-	-	-

[a] The smallest reported effective molar ratio of inhibitor to Amyloid β-protein.

[b] The time (min) required to reach half the maximum fluorescence intensity at the reported ratio of inhibitor to Amyloid β-protein.

[c] Whether the inhibitor can reduce Amyloid β-protein cytotoxicity.

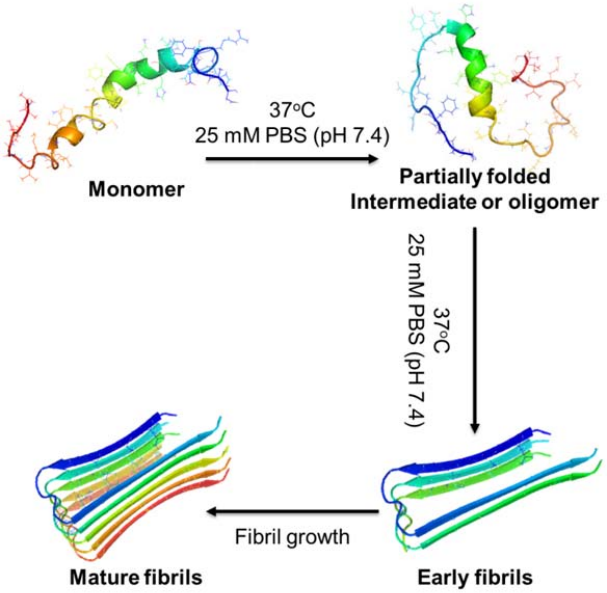

Figure 2.1 A schematic overview in vitro study of Aβ fibrillation, which includes the conformational transition from monomer to partially folded intermediate or oligomer to mature fibrils.

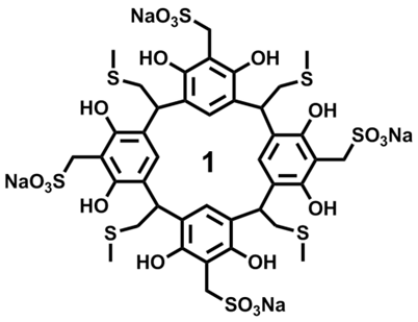

Figure 2.2 The structure of resorcinarene

2.2 Experimental Section

2.2.1 Materials

All solvents were purchased from commercial suppliers and used without further purification. Amyloid β-protein 40 (purity 95.77%) and 42 (purity 95.19%) were purchased from ChinaPeptides. All other reagents and starting materials were purchased

from Aldrich or VWR and used without further purification unless otherwise noted. Solutions were prepared from nanopure water purified from Milli-Q plus system (Millipore Co.), with a resistivity over 18 MΩ cm^{-1}. Compound **1** were prepared according to our previously published literature procedures.[175] Deuterated solvents were purchased from Cambridge Isotope Laboratories Inc. and used as received. ThT fluorescence was measured by a fluorescence spectrophotometer (LS-55, Perkin Elmer) at 25 ^{o}C with a slit width of 5 nm for both excitation and emission. Far-UV CD spectroscopy was measured on JASCO J-810. Atomic force microscopy was used by tapping mode with cantilever having a resonance frequency of ~170 kHz and typical force constant of 7.5 N/m.

2.2.2 Methods and Characterization

Synthesis of resorcinarene

The resorcinarene was prepared according to our previous published literature procedures.[175] All characterizations, including NMR, mass-spec, and X-ray crystallography, are consistent with previous reported results. Briefly, the resorcinarene precurser was added to a solution which contained formaldehyde, sodium sulfide, and water, and stirred for 4 h at 90-95 ^{o}C. The mixture was cooled down to room temperature, and neutralized with hydrochloric acid. Acetonitrile was added to precipitate sulfonated resorcinarene. Finally, the resulting product **1** (Figure 2.2) was recrystallized and washed in the same solvent acetonitrile.

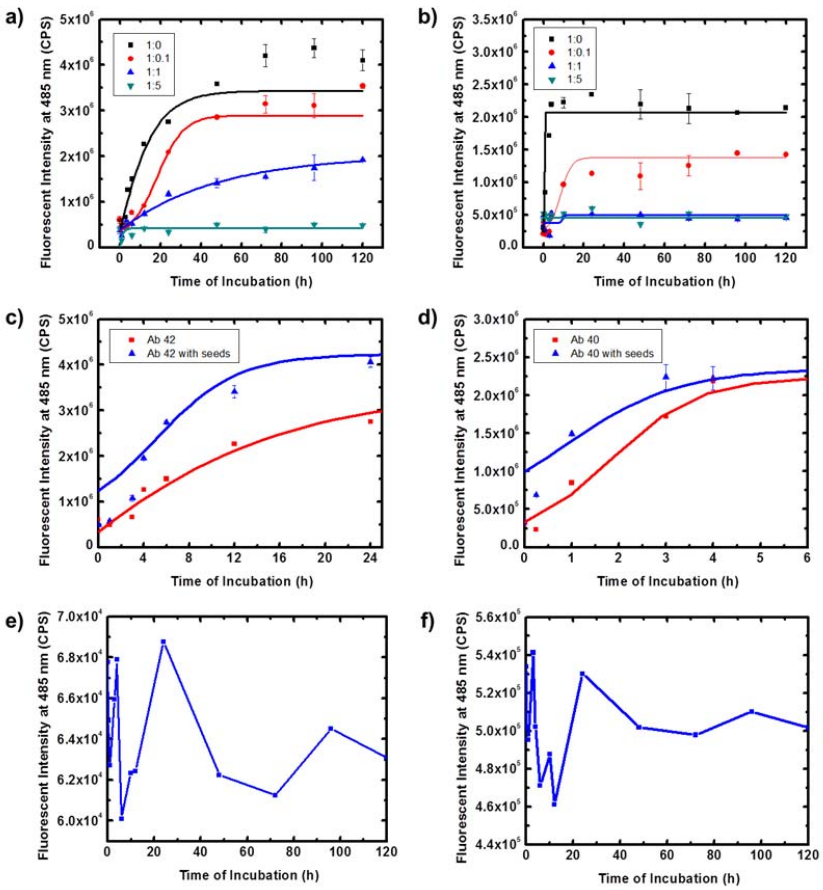

Figure 2.3 a) Kinetics of 10 μM of Aβ 42 and Aβ 40 fibrillation: fluorescence intensity of Thioflavin T (ThT) at 485 nm as a function of incubation time at 37 ^{o}C in 25 mM PBS, pH 7.4 with the ratio of Aβ to 1 at 1:0, 1:0.1, 1:1, and 1:5, respectively. The final concentration was a 2-fold dilution with 20 μM ThT. Normalized ThT fluorescence intensity of incubated c) Aβ 42 and d) Aβ 40 at 485 nm against incubation time: no seeds added (red), preformed seeds added (blue). Preformed seeds were collected after different hours incubation (2 h for Aβ 42 and 0.17 h for Aβ 40) of freshly made 10 μM Aβ 42 and Aβ 40 solution. After gel filtration by running through Phenogel™ 5 μm 10E4A column, the collected solution was lyophilized. Then the resulting products were added to Aβ 42 and Aβ 40 to prepare 0.3 μM seeds solution. Fluorescence spectra of e) 0.15 mM **1** alone and f) 0.15 mM **1** with 20 μM Thioflavin T (ThT) as a function of incubation time at 37 ^{o}C in 25 mM PBS, pH 7.4. The emission was monitored at 480 nm with the excitation at 440 nm. The ThT fluorescence was obtained for three repeats of each sample. The error bars indicate the standard error of the mean.

Thioflavin T (ThT) Fluorescence Assay

The kinetics of Aβ 42 and Aβ 40 fibrillation can be characterized by the fluorescence increase of fibril-specific dye of Thioflavin T (ThT). To accomplish this, different concentrations of resorcinarene, including the ratio of peptides to the resorcinarene at 1:0, 1:0.1, 1:1, and 1:5, were prepared for examination. At first, Aβ 42 and Aβ 40 were dissolved in 1,1,1,3,3,3-hexafluoroisopropanol to stabilize the α-helix structure of the peptides. After evacuating the solvent, the solution was filtered through a 0.2 μm membrane to remove the pre-fibrils. Different concentrations of resorcinarene were added to 10 μM Aβ in 25 mM PBS buffer solution (pH 7.4), respectively. Thereafter, the mixture were incubated at 37 ^{o}C, and aliquots of incubation solutions at different time points were collected and then diluted two times into ThT solution (25 μM ThT in 25 mM PBS buffer, pH 7.6). ThT fluorescence was measured by a fluorescence spectrophotometer (LS-55, Perkin Elmer) at 25 ^{o}C with a slit width of 5 nm for both excitation and emission. ThT emission was monitored at 480 nm with the excitation at 440 nm.

Circular Dichroism (CD) Spectroscopy

To gain insights into the effects of resorcinarene on the conformational transition of Aβ, far-UV CD spectroscopy (JASCO J-810) were utilized to monitor the secondary structure of Aβ over time.[176] Similar to the fluorescence characterization, aliquots of incubation solutions described above were collected for CD spectra as well. The spectra was recorded between 190 and 260 nm at room temperature by a 2 mm optical path length quartz cell.

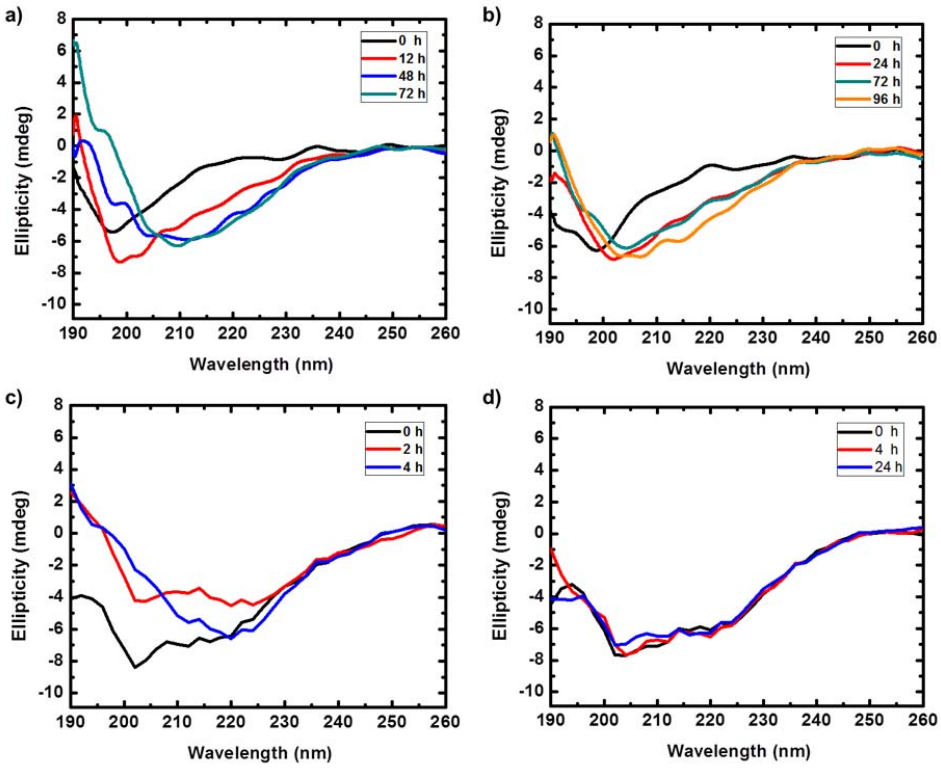

Figure 2.4 Far-UV circular dichroism spectra of a) 10 μM Aβ 42 alone at 0, 12, 48, 72 h, b) 10 μM Aβ 42 incubated with 10 μM **1** at 0, 24, 48, 96 h. c) 10 μM Aβ 40 alone at 0, 2, 4 h, and d) 10 μM Aβ 40 incubated with 10 μM **1** at 0, 4, 24 h, in 25 mM pH = 7.4 PBS.

Atomic Force Microscopy (AFM)

AFM images of samples withdrawn at different incubation times can be studied to directly observe and monitor the formation of fibrils. Tapping mode was used to observe morphologies during the fibrillation process. The cantilever has a resonance frequency of approximately 170 kHz with typical force constant of 7.5 N/m. To scan the AFM images, aliquots of samples withdrawn at different incubation times were diluted with pure water, drop-coated on a freshly cleaved mica surface, and allowed to dry for at least 1 h.

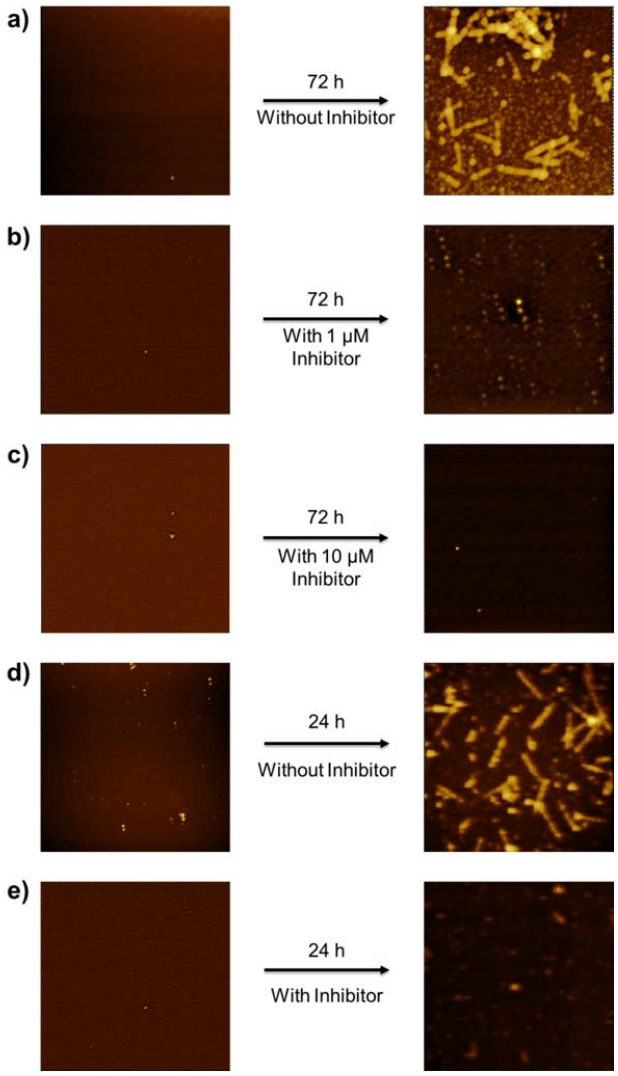

Figure 2.5 AFM images (size: 2.5 X 2.5 μm) of 10 μM Aβ 42 incubated with a) 0 μM, b) 1 μM, and d) 10 μM **1**, respectively, and 10 μM Aβ 40 incubated with e) 0 μM and f) 10 μM **1**, respectively, at 37 ^{o}C in 25 mM PBS, pH 7.4.

Cytotoxicity Assay

Toxicity tests were performed in a new 24-well cell culture plate. In each well, health fertilized eggs were incubated in 2 ml control sea water or 2 ml dilution of 1 in sea water. For the **1** cytotoxicity test, the plate with fertilized eggs (*Strongylecentrotus purpuratus*

sea urchins) was incubated at 15 °C for 48 hours until they reach prism stage embryos. Aβ 42 fibrils and different Aβ 42 - **1** complex were collected from incubated solutions. The plate with fertilized egg (*Lytechinus variegatus sea urchins*) to test the inhibiting effect of **1** on Aβ 42 toxic species were performed at room temperature for 24 hours until they reach prism stage embryos. 100 of embryos are examined and rate of embryo with normal development was calculated. Each experiment was repeated with similar results. The error bars indicate the standard error of the mean.

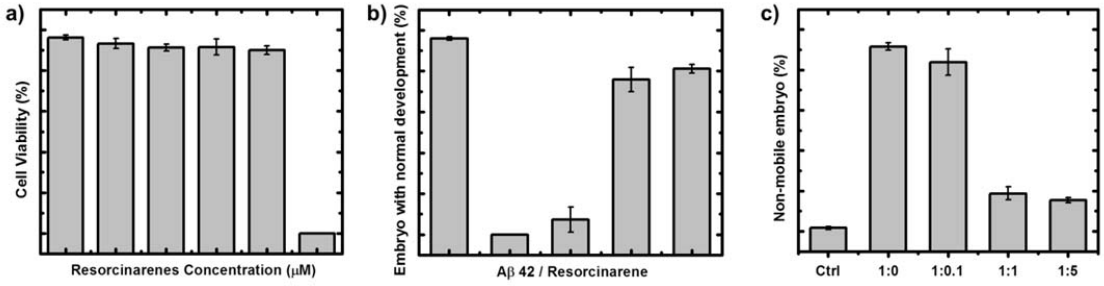

Figure 2.6 a) Cytotoxicity test of resorcinarene to seaurchin embryos. b) The inhibitory effect of resorcinarene on the cytotoxicity of Aβ 42 fibrils at different molar ratios of Aβ 42 to resorcinarene. c) Percentage of non-mobile embryos at different molar ratios of Aβ 42 to resorcinarene.

SDS Polyacrylamide Gel Electrophoresis

After incubating 48 h, SDS-PAGE of Aβ - resorcinarene complex, including pure Aβ 40 and 42, Aβ 40 and 42 with 10 μM resorcinarene, and pure Aβ 40 and 42 mixed with 10 μM resorcinarene was performed. The component of 18 % SDS-PAGE gel contains: 1) 5 mL 18 % resolving gel which is made up of 0.6 ml H_2O, 3 ml 30% acrylamide mix, 1.3 ml 1.5 M Tris-HCl (PH 8.8), 50 μl 10% SDS, 50 μl 10% ammonium persulfate, 4 μl TEMED, and 2) 1 ml 5% stacking gel which consist of 0.68 ml H_2O, 0.17 ml 30%

acrylamide mix, 0.13 ml 1.0 M Tris-HCl (PH 6.8), 10 µl 10% SDS, 10 µl 10% ammonium persulfate, 1 µl TEMED. Each protein sample was prepared by dissolving 100 ng of pure protein in Laemmli sample buffer (Laemmli 1970) and boiling for 5 minutes before running on an 18% SDS-PAGE gel. After electrophoresis, the gel was fixed in fixing solution (30% ethanol, 10% acetic acid) for 45 minutes and then processed for silver staining using Pierce® Silver Stain for Mass Spectrometry kit (Thermo Fisher Scientific, Waltham, MA). Picture of gel was taken by using Epson Perfection V370 Photo scanner.

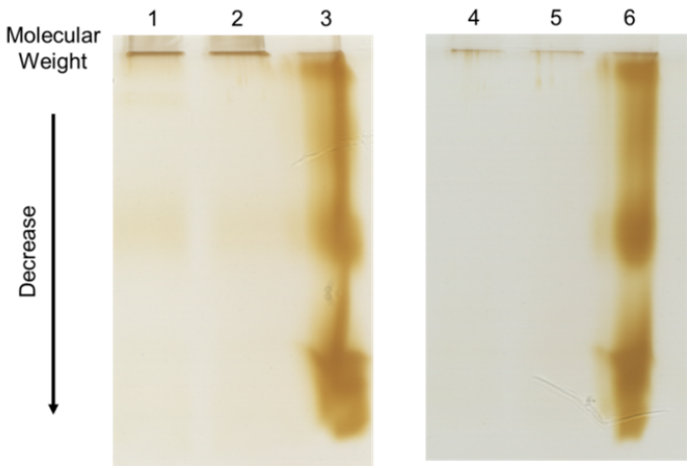

Figure 2.7 SDS-PAGE of Aβ and Aβ - resorcinarene complex. Each number represents 1) Aβ 42 at incubation time 48 h, 2) solution of 1) mixed with 10 µM resorcinarene, 3) Aβ 42 - 10 µM resorcinarene complex at incubation time 0, 4) Aβ 40 at incubation time 48 h, 5) solution of 4) mixed with 10 µM resorcinarene, 6) Aβ 40 - 10 µM resorcinarene complex at incubation time 0.

Ligand Docking and Molecular Dynamics Simulations

Possible binding modes of the resorcinarene to Aβ 42 amyloid fibrils were simulated using Potential Energy Landscape Explorer web-server (PELE:

http://pele.bsc.es/pele.wt).[177] We hypothesized that the resorcinarene can bind to the ends of the filament and delay the amyloid fiber growth by interfering the monomer addition. Accordingly, two most populated conformations from the PELE simulations with the ligand bound on the top or the bottom of the filament were selected for the initial configurations of the subsequent molecular dynamics simulations. Molecular dynamics (MD) simulations of the ligand bound amyloid fibrils were carried out using Amber14 software.[178] The molecular mechanics parameters of the resorcinarene was prepared using the Generalized Amber Force Fields (GAFF).[179] Atomic partial charges of the ligand were computed using the AM1-BCC charge model embedded in the antechamber program (Table 2.2). The amyloid filament was modeled using the AmberFF14SB force fields.[180] The MD simulations were initiated from the two most populated structures found from the PELE simulations. Each initial structure was solvated in an octahedral box filled with TIP3P water molecules, where the solute molecule has 11 Å margin from the solvation boundary. Counter ions were added to guarantee the charge neutrality. Each solvated system was equilibrated at 300 K for 6 ns, while keeping positions of all carbon atoms at initial values. 100 ns production runs were followed, while restraining alpha carbons of the filament at initial positions using weak harmonic potentials (spring constant was 0.1 kcal/mol/$Å^2$).

Details of the PELE simulations

Detailed molecular structure of the amyloid filament (PDB Code: 2BEG) was retrieved from Protein Data Bank (PDB). The amyloid fibril structure consists of five chains of Aβ protein, spanning from Leu17 to Ala42. Using the amyloid fibril and a

resorcinarene, 40 PELE simulations were repeated to produce > 24,000 ligand bound conformations.

Table 2.2 Optimized coordinates and atomic partial charges of resorcinarene that are used for MD simulations

Atom	X	Y	Z	AM1-BCC Partial Charge
C1	0.305	-3.151	0.263	-0.1463
C2	1.728	-3.096	0.784	0.04915
C3	2.52	-1.954	0.181	-0.1463
H1	2.23	-4.063	0.489	0.0822
C4	-0.047	-4.1	-0.724	0.156975
C5	-0.701	-2.333	0.787	-0.0675
C6	-1.368	-4.237	-1.203	-0.10905
C7	-2.345	-3.414	-0.604	0.156975
C8	-2.038	-2.475	0.401	-0.1463
C9	-3.152	-1.693	1.056	0.04915
C10	-3.237	-0.289	0.493	-0.1463
H2	-4.135	-2.21	0.798	0.0822
H3	-0.441	-1.576	1.541	0.12275
C11	-4.197	-0.004	-0.505	0.156975
C12	-4.373	1.294	-1.03	-0.10905
C13	-2.425	0.747	0.96	-0.0675
C14	-3.557	2.31	-0.485	0.156975
C15	-2.587	2.06	0.506	-0.1463
H4	-1.654	0.531	1.713	0.12275
C16	-1.774	3.207	1.062	0.04915
C17	-0.415	3.263	0.392	-0.1463
H5	-2.314	4.175	0.8	0.0822
C18	3.532	-2.219	-0.765	0.156975
C19	4.399	-1.221	-1.259	-0.10905
C20	4.173	0.092	-0.803	0.156975
C21	3.179	0.401	0.151	-0.1463
C22	2.352	-0.63	0.606	-0.0675
H6	1.561	-0.397	1.333	0.12275
C23	3.115	1.803	0.723	0.04915
C24	1.919	2.573	0.215	-0.1463
H7	4.046	2.351	0.364	0.0822
C25	2.084	3.482	-0.851	0.156975
C26	1.047	4.332	-1.294	-0.10905

C27	0.655	2.464	0.804	-0.0675
H8	0.503	1.74	1.618	0.12275
C28	-0.203	4.176	-0.665	0.156975
O1	0.981	-4.884	-1.172	-0.5311
H9	0.664	-5.721	-1.71	0.457125
O2	-3.629	-3.596	-1.068	-0.5311
H10	-4.296	-2.989	-0.571	0.457125
O3	-4.94	-1.077	-0.912	-0.5311
H11	-5.799	-0.818	-1.447	0.457125
O4	-3.778	3.568	-0.996	-0.5311
H12	-3.167	4.267	-0.553	0.457125
C29	-1.744	-5.171	-2.296	-0.24705
S1	-1.708	-6.823	-1.75	1.4213
H13	-1.087	-5.012	-3.194	0.085825
H14	-2.743	-4.893	-2.73	0.085825
O5	-2.554	-6.996	-0.523	-0.752533
O6	-2.171	-7.747	-2.83	-0.752533
O7	-0.257	-7.118	-1.396	-0.752533
O8	4.94	1.157	-1.214	-0.5311
H15	5.513	0.941	-2.02	0.457125
O9	3.663	-3.535	-1.154	-0.5311
H16	4.313	-3.644	-1.923	0.457125
O10	3.273	3.607	-1.531	-0.5311
H17	3.982	2.951	-1.178	0.457125
O11	-1.301	4.929	-1.006	-0.5311
H18	-1.177	5.45	-1.863	0.457125
C30	-5.33	1.605	-2.123	-0.24705
S2	-6.975	1.524	-1.563	1.4213
H19	-5.154	0.929	-3.003	0.085825
H20	-5.092	2.601	-2.588	0.085825
O12	-7.919	1.946	-2.643	-0.752533
O13	-7.165	2.383	-0.347	-0.752533
O14	-7.221	0.071	-1.184	-0.752533
C31	-3.047	-1.668	2.581	0.0202
S3	-3.187	-3.321	3.316	-0.37845
H21	-3.816	-0.997	3.013	0.067575
H22	-2.068	-1.265	2.929	0.067575
C32	-4.776	-3.943	2.741	-0.0235
H23	-4.774	-4.184	1.67	0.069033
H24	-5.001	-4.871	3.288	0.069033
H25	-5.599	-3.243	2.927	0.069033
C33	5.519	-1.552	-2.175	-0.24705
S4	6.954	-1.964	-1.262	1.4213

H26	5.231	-2.366	-2.897	0.085825
H27	5.704	-0.722	-2.91	0.085825
O15	6.66	-3.173	-0.41	-0.752533
O16	8.084	-2.268	-2.198	-0.752533
O17	7.321	-0.813	-0.366	-0.752533
C34	1.74	-3.031	2.315	0.0202
S5	3.465	-3.056	2.895	-0.37845
H28	1.161	-3.866	2.754	0.067575
H29	1.267	-2.102	2.699	0.067575
C35	3.578	-4.608	3.805	-0.0235
H30	3.405	-5.483	3.168	0.069033
H31	2.876	-4.657	4.646	0.069033
H32	4.594	-4.692	4.221	0.069033
C36	1.28	5.334	-2.364	-0.24705
S6	1.811	6.859	-1.695	1.4213
H33	0.378	5.452	-3.021	0.085825
H34	2.018	4.94	-3.114	0.085825
O18	0.764	7.38	-0.745	-0.752533
O19	2.029	7.834	-2.813	-0.752533
O20	3.093	6.664	-0.927	-0.752533
C37	-1.638	3.168	2.584	0.0202
S7	-3.239	3.324	3.424	-0.37845
H35	-0.948	3.962	2.932	0.067575
H36	-1.199	2.211	2.944	0.067575
C38	-3.897	4.9	2.855	-0.0235
H37	-4.801	5.127	3.44	0.069033
H38	-4.185	4.884	1.796	0.069033
H39	-3.195	5.731	2.999	0.069033
C39	3.189	1.744	2.25	0.0202
S8	3.502	3.372	2.989	-0.37845
H40	3.971	1.027	2.573	0.067575
H41	2.241	1.376	2.703	0.067575
C40	5.13	3.833	2.37	-0.0235
H42	5.446	4.751	2.889	0.069033
H43	5.889	3.066	2.563	0.069033
H44	5.13	4.042	1.293	0.069033

Once the PELE simulations were finished, we analyzed the conformations of the Aβ 42 fibril bound to resorcinarene. First, we analyzed the center-of-mass (CM) position of the bound resorcinarene on top or the bottom of the filament. We considered 1 $Å^3$ bins

near the ends of the fibril. For each bin, the total number of occurrences that the CM of resorcinarene were bound was counted. The most populated spatial bins on the top and the bottom of the fibril were chosen and the corresponding conformations were used as the initial configurations of the molecular dynamics (MD) simulations.

Analysis of solvent accessible surface area (SASA) and trans-rotational entropy

We used VMD software for the computations of solvent accessible areas of the resorcinarene bound complex ($SASA_{cmpl}$), the amyloid fibril ($SASA_{prot}$) and the ligand ($SASA_{lig}$). The buried solvent accessible surface area is defined:

$$\Delta SASA = SASA_{cmpl} - \left(SASA_{prot} + SASA_{lig}\right).$$

From the MD trajectories of the complex, we separated the amyloid fibril and the ligand to compute corresponding SASA values. The probe radius of the SASA value was 1.6 Å.

The translational and the rotational entropies are defined11:

$$S_{trans} = \frac{k_B}{2}\left[5 + 3\log\left(\frac{2\pi m}{\beta h^2}\right) - 2\log(\rho)\right]$$

$$S_{rotation} = \frac{k_B}{2}\left[3 + \log(\pi I_A I_B I_C) + 3\log\left(\frac{8\pi^2}{\beta h^2}\right) - 2\log(\sigma)\right]$$

where m is the mass of molecule, T is temperature, $\beta = k_B T$ is the Boltzmann constant, h is Planck constant, ρ is the number density (in units of mole), σ is the symmetry factor of the molecule, and $I_{A,B,C}$ are three rotational moments of inertia. The rotational moments of inertia were averaged over the last 20 ns of MD simulations, using VMD software. The entropic contribution of free energy (-TS) is computed at 300 K.

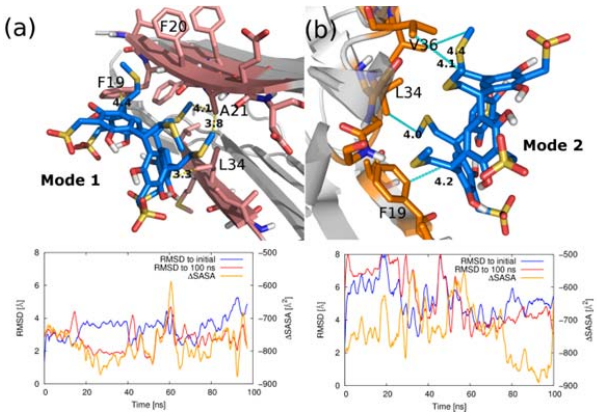

Figure 2.8 Predicted interactions of the resorcinearene and the Aβ 42 amyloid filament. Two of the relatively stable interactions patterns are predicted using the PELE and the MD simulations: (a) and (b). The last snapshots from the MD simulations are illustrated. Root-mean-squared deviations from the initial docked structure (blue), the last configuration of the MD simulation (red), and the buried surface area of the ligand-protein interface (orange) of each are plotted on bottom.

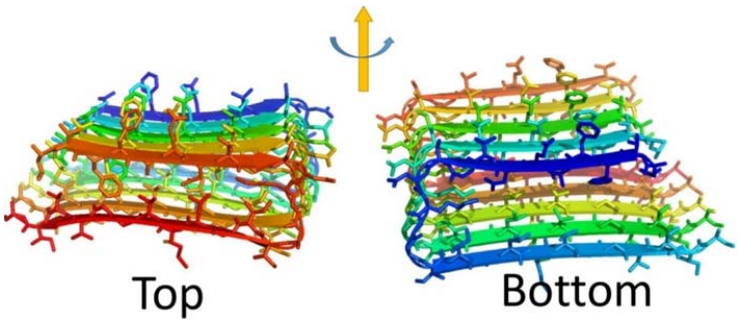

Figure 2.9 The top and the bottom of the Aβ 42 fibril (PDB Code: 2BEG).

2.3 Results and Discussions

2.3.1 Inhibitory Effect of Resorcinarene on Aβ Fibrillation.

The cationic benzothiazole dye, thioflavin T (ThT), is well known for its specific staining of amyloid fibrils, which enhances emission fluorescence. Figure 2.3 shows the aggregation kinetics of Aβ fibril formation at different concentrations of **1** by the time dependent ThT fluorescence assay. When incubating 10 μM Aβ 42 alone, the ThT

fluorescent profile presented a lag phase within 3 h, a slow elongation, and a saturated phase after 3 days, while Aβ 40 displayed a similar but faster fibrillation process with an almost negligible lag phase which maintained less than 1 h, an elongation phase within 3 h, and a saturated phase after 4 h. To evaluate the inhibition activity of **1** against Aβ fibrillation, Aβ were present with different concentrations of **1** at the ratio of the resorcinarene to peptides of 0.1, 1, and 5, respectively. At a Aβ 42/1 ratio of 0.1, suppression of Aβ 42 aggregation was observed, where the elongation phase did not start until incubating for 12 h, in contrast to 3 h for Aβ 42 alone to enter into the same phase. Adding more 1, the fluorescent intensity decreased by over 50 % at the plateau. At Aβ 42/**1** ratio of 5, almost no fibrils were observed as evidenced by the nearly flat curve comparing to others. Overall, ThT profiles demonstrated that **1** inhibited Aβ 42 fibrillation in a dose dependent manner. **1** displayed a similar but more effectively inhibition on Aβ 40. **1** began to exhibit inhibition effect at Aβ 40/**1** ratio of 0.1. When the Aβ 40/**1** ratio increased up to **1**, the lag phase period extended to approximately 4 h. If the concentration of **1** was further increased, **1** showed a stronger effect of fibrillation inhibition, which retained active for 5 days. As control experiments, resorcinarene was incubated alone at 37 ^{o}C for 24 h, and the fluorescence spectra of not only resorcinarene (Figure 2.3e), also resorcinarene with 20 μM ThT (Figure 2.3f) showed no disturb towards ThT assay tests above. To note, it is surprising to observe that Aβ 40 aggregated faster than Aβ 42. It may attribute to the protein purity since impure protein tends to aggregate more slowly. However, in accordance with Table 2.1 and results above, **1** exhibited excellent potential for effectively inhibiting both Aβ 40 and Aβ 42 fibrillation. The other reason leading to the faster Aβ 40 aggregation might be that the prepared

amyloid-β peptides may contain seeds which can accelerate the fibrillation process.[181-183] To further confirm our hypothesis, we carried out additional series of measurements with regard to the aggregation of kinetics of Aβ 40 and 42. Preformed fibrils (seeds) were added to Aβ 40 and Aβ 42 at the beginning of incubation, respectively. By recording ThT assay of aggregation kinetics, the lag phase time of both amyloid-β peptides with additional seeds was found to decrease comparing to that without added seeds. In other words, both Aβ 40 and Aβ 42 with additional seeds aggregate faster than those without seeds.

The Aβ peptides are mainly random coil or α-helical in the native conformation and undergoing a conversion to β-strand during the fibril formation, which is consistence with ThT assay examination. To attain a clear perception of the effect of **1** on the conformational conversion of Aβ 42 and 40 upon aggregation, far-UV CD spectroscopy was employed to monitor the secondary structure of the Aβ peptides over time (Figure 2.4). Aliquots of Aβ 42 and 40 in the absence and presence of inhibitor were collected for CD spectra at different time, respectively. Even though peptides were incubated in PBS buffer which has an influence on the CD spectra, the spectra obtained is still distinguishable. As shown in Figure 2.4a, Aβ 42 alone at incubation time 0 has a negative band at around 197 nm, indicating that the initial secondary structure of Aβ 42 adopted a random coil form. After incubating 12 hours, this peak diminished and shifted slightly to approximately 200 nm, suggesting the conformational change of Aβ 42. Upon peptides aggregation for 48 hours, a negative valley appeared at 213 nm, which is assigned to β sheet of mature peptide fibril. When present with 10 μM **1**, Aβ 42 showed a similar structure transition with adopting mainly random coil conformations as evidenced from

Figure 2.4b. However, Aβ 42 did not completely convert to β sheet conformation even after incubating 96 hours comparing to the study of Aβ 42 in the absence of **1**. That is, **1** can potentially delay the conformational transition of Aβ 42. In the case of Aβ 40, Figure 2.4c showed a mixture of random coil, β sheet, and β turn forms. Upon peptide aggregation, bands shrink demonstrating conformational change severely where a significant decrease in the negative absorption around 200 nm. The final content of β strand conformers at 4 h was much more than that of initial Aβ 40. In the presence of **1** in Aβ 40 solution, it displayed a similar random coil dominated conformations, but undergoing no transition with 24 h incubation, suggesting a delay of fibrillation process (Figure 2.4d). It can be concluded that the inhibitory effect of **1** on conformational transition of Aβ aggregation from random coils to β strand.

To directly observe and monitor the formation of these Aβ 40 and 42 fibrils, AFM images were obtained in the absence and presence of **1**. The inhibition effect of **1** on Aβ peptides fibrillation is consistent with the previous observations. As illustrated in Figure 2.5, Aβ 42 fibrils were apparent after 72 h incubation in the absence of **1**, whereas when present with **1**, especially with higher concentration, no long fibrils showed up during the incubation. Aβ 40 went through the fibrillation process with a higher rate, and fibrils were observed clearly only after 24 h incubation (Figure 2.5), comparing to the fact that no long fibrils but a few protofibrils were recognized when incubating with the inhibitor. To further confirm the contents of the ThT endpoint samples, a pellet assay with an SDS-PAGE gel was prepared. Figure 2.7 shows that fibrils from the solution without **1** are much larger than that with **1**, which again reveals that **1** can retard the aggregation of both amyloid-β peptides.

To note, all the tested Aβ and resorcinarene mixtures contained the same amount of Aβ, and any increase in the fluorescent intensity from ThT assay profile may indicate more fibrils were formed. It is interesting to observe that the final ThT intensity of resorcinarene mixed Aβ solution decreased and stabilized much lower than that of Aβ alone, meaning less fibrils were produced. The amyloid fibril formation is a multi-stage process that depends on the formation of small oligomeric species.[144, 184, 185] With regard to the inhibition effect, we speculate that resorcinarene interact with Aβ filament at early stage. The bound resorcinarene impede inter oligomers association by steric hindrance and delay the onset of fibril growth. The hypothesis is in accordance with CD and AFM study where Aβ fibrils were apparent in the absence of resorcinarene while a few oligomers were formed in the presence of the inhibitor.

2.3.2 Cytotoxicity test of resorcinarene to sea urchin embryos

The effective inhibition of Aβ fibril formation by **1** suggests the potential capability of 1 for therapy of AD application. A series of cell viability tests were conducted to evaluate the cytotoxicity of **1** in the cellulous environment in which sea urchin embryos were selected as a model system due to its extremely sensitive to hazardous materials, and have been widely used for static acute toxicity of many chemicals test. Strongylecentrotus purpuratus sea urchins (*Marinus Scientific, Long Beach, CA*) were utilized in this study to test the toxicity of **1**, and adult animals with ripe gonads were used to collect gametes. Fresh eggs were washed for 3 times with cold filtered artificial sea water and mixed with sperm to examine fertilization rate. Only eggs with a fertilization rate greater than 95% were used for the toxicity tests. Three biological replicates using three individual male-female pairings were performed. Figure 2.6a shows

90 % of embryos retain a normal morphology after 20 h of incubation with the presence of 20 μg/ml **1**, in which concentration already exhibited significant effect on inhibition of Aβ fibrillation, indicating low cytotoxicity of **1** to cells. Unfortunately, since sea urchins are extremely sensitive to invading materials, when the concentration of **1** increasing up to 1000 μM, most of the cells failed to survive under the incubation environment. The effective inhibition of Aβ 42 cytotoxicity by **1** can suggest potential utility for therapeutic applications. A series of cell viability tests were performed to measure such effects induced by **1**. Pure Aβ 42 fibril reduced the viability of sea urchins cells (Lytechinus variegatus) in normal forms to 0 %, whereas the Aβ 42 – **1** complex delayed the formation of Aβ 42 toxic species, where the rate of normal embryos increased to 81% with 50 μM **1** (Figure 2.6b). In addition to the normal form of sea urchin cells, there exist some cells alive but unable to swim. In figure 2.6c, 92% of embryos are alive but in abnormal forms when present with 10 μM pure Aβ 42 fibrils. Applying more **1**, the rate decreased, which indicated the reducing toxicity of Aβ 42 fibrils induced by **1**.

2.3.3 Resorcinarene Binds to the Top and the Bottom of the Aβ42 Filament

The detailed interactions between the resorcinarene and the amyloid filament were studied using molecular docking and molecular dynamics (MD) simulations. The MD simulations were initiated with bound resorcinarene on the top or the bottom of the amyloid fibril (Figure 2.9). The bound conformations were identified from the results of the docking simulations using the PELE software. Figure 2.8 shows two of the binding modes of the resorcinarene resulting from the 100 ns MD simulations. After 80 ns of MD simulations, the root-mean-squared deviation (RMSD) of all heavy atoms of the bound resorcinarene converged to < 3.0 Å from the last configuration at 100 ns. Of note, the

RMSD to the initial docked conformation increased to > 4.0 Å as MD simulation progressed, that suggests a conformational relaxation took place during the course of MD simulations. The solvent accessible surface area of the ligand-amyloid fiber complex was always smaller than that of the isolated ligand and amyloid fiber. The finding indicates the ligand is always in contact with the amyloid fibril. The averaged buried solvent accessible surface area (ΔSASA) over the last 20 ns was -767 $Å^2$ for the mode 1 and -845 $Å^2$ for the mode 2. We also computed surface area dependent non-polar hydrophobic energies using the formula proposed by Honig's group: E_hphobic = γ×ΔSASA, where γ is 0.05 kcal/mol/ $Å^2$.[186] The computed non-polar hydrophobic energies averaged over the last 30 ns MD simulations are -38 kcal/mol and -42 kcal/mol for the mode 1 and the mode 2, respectively. The amount of the non-polar interaction energies are sufficient to overcome translational-rotational entropic penalty that is +26 kcal/mol less favorable for binding. We analyzed favorable interactions across the interface of the bound resorcinarene and the amyloid fibril. In the first binding mode (Figure 2.8), thiomethyl groups of the resorcinarene were in contact with methyl group of Ala21 in the amyloid bilayer interface. Also a sp^2 carbon of resorcinol is in contact with the sidechain of Leu34 and Phe19. Likewise, in the second binding mode (Figure 2.8), thiomethyl groups make non-polar contacts with Val36 and Leu34. A sp^2 carbon of resorcinol is in contact with the sidechain of Phe19.

2.4 Summary

In summary, the effective inhibition of Aβ fibrillation by resorcinarene was demonstrated in vitro by the ThT assay, the circular dichroism spectroscopy, and the atomic force microscopy. Using the computational methods, including docking

simulations and MD simulations, the binding of resorcinarene was shown to be mediated by both the non-polar interactions and the sulfur mediated hydrogen bonds. The advantages that could arise with resorcinarene that is significantly better than others at Aβ fibrillation inhibition include: (1) lower concentration required to block Aβ aggregation, (2) low toxicity to seaurchin embryo, which is extremely sensitive to hazardous materials, and (3) the formation of Aβ toxic species can be delayed, which all make our designed inhibitor a promising candidate for the treatment of Alzheimer's disease. To our knowledge, it is the first time for the application of resorcinarene on the Aβ fibrillation. Thus, with the remarkable inhibitory function towards Aβ fibrillation and its capability in encapsulation, resorcinarene presented in this work shows great potential to be applied in pharmaceutical industry or other areas for the treatment of Alzheimer's disease.

Chapter 3 Biocompatible and Blood-Brain Barrier Permeable Carbon Dots for Inhibition of Aβ Fibrillation and Toxicity, and BACE1 Activity

3.1 Background

Within biological systems, the information that directs hierarchical assembly is ciphered in the Watson-Crick structure based DNA and RNA, respectively, to induce the formation of elaborate nature materials.[1, 187] Peptide or protein, whereby expressed by these encoded genes, is the primary embodiment of biofunction, and the effective organization of their nature assembly in response to environmental and structural changes demonstrates certain corresponding cellular functions. However, misfolded peptide or protein can result in the irreversible damage to the regular metabolism.[188] It has been established for decades that highly ordered peptide or protein aggregates deposited in the brain can cause most neurodegenerative diseases, such as Alzheimer's, Parkinson's, and Huntington's.[144] Of all these amyloidosis, Alzheimer's disease (AD) is a leading cause of death worldwide, where no current cure but therapy for delaying its onset is available.[138]

The precise mechanism of AD pathogenicity remains to be established, but one considerable molecular etiology that underlies AD involves the aggregation of amyloid-β peptides (Aβ), Aβ 40 and 42.[6, 142] Both peptides are produced from sequentially proteolytic cleavage of amyloid precursor protein (APP) by β- and γ-secretases.[189] The resulting Aβ peptides can assemble into oligomers, also known as seeds, and induce other peptides to follow this misfolded process to further promote the formation of Aβ fibrils in an effective "catalytic" cycle.[181, 190] To redirect this "inaccurate" encoded pathway, the design of antiamyloiddogenic agents for AD involves inhibiting the energetically driven assembly process of amyloid plaques by their binding towards Aβ monomer, oligomer, or

filament. To this end, many of peptides,[158] organic compounds,[191] and conjugated nanoparticles[192] have been examined towards developing novel amyloid inhibitors. However, in addition to inhibiting Aβ fibril assembly, very few of these addressed other challenges arise with AD treatments, which include the capability to: 1) target upstream secretases, β- or γ-secretases,[193] to cut off Aβ fibrils generation resources, 2) reduce the toxicity of Aβ 42 oligomer,[149] and 3) penetrate blood-brain barrier (BBB),[194] where capillary endothelial cells are tightly interconnected to protect the central nervous system, for delivery to pathological tissues. Therefore, before the development of potential drug for better AD treatment can be realized, there is a need for new antiamyloiddogenic agent that can resolve these concerns.

Carbon dots (C-Dots) – whereby first discovered accidently during purification of carbon nanotubes - recently have emerged as a benign zero-dimensional nanomaterial with its unique optical properties and biocompatibility.[195, 196] With either top-down or bottom-up strategy, the prepared C-Dots exhibit promising applications in bioimaging,[197] optronics,[198] drug delivery,[199] and biosensiong,[196] respectively. Previously, we have managed to utilize human transferrin (HT) to deliver the C-Dots across the BBB in a zebrafish model.[200] Inspired by this, we turned to C-Dots as a potential drug candidate towards designing a new BBB-permeable nanomaterials in application of AD treatment for the first time. C-Dots posses large surface to volume ratios, and this low dimensionality nanomaterials are expected to redirect the partially unfolded Aβ by increasing the fibril steric hindrance as a result of their interaction with Aβ monomer (Figure 3.1). This hypothesis was examined by experimental and theoretical methods, respectively. The synthesized C-Dots were also found to inhibit the active site of β-

secretases 1 (BACE1) enzyme and reduce the toxicity of Aβ fibril in vitro, respectively. In addition, combined with our previous results, hereby, we further proved that the C-Dots demonstrated higher binding affinity towards forebrain in a zebrafish model. These results demonstrate an excellent potential application for further optimization of C-Dots as an antiamyloiddogenic agent for AD treatment.

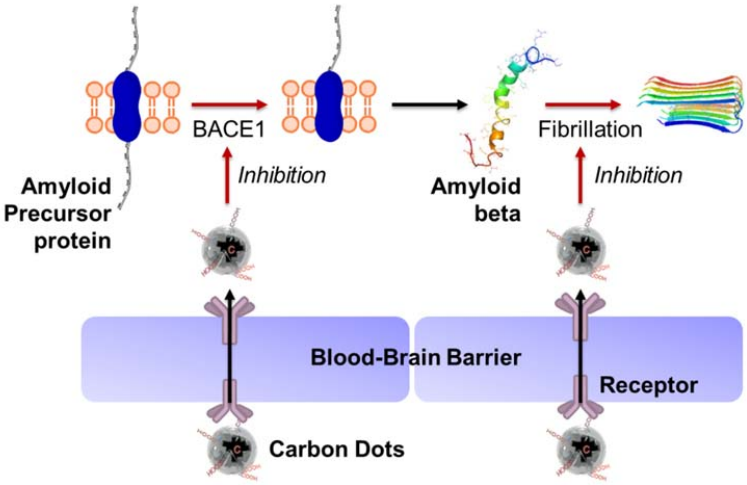

Figure 3.1 The effect of blood-brain barrier permeable carbon dots on the inhibition of BACE1 activation and Aβ fibrillation.

3.2 Experimental Section

3.2.1 Materials

Amyloid β-protein 40 (purity 95.77%) and 42 (purity 95.19%) were purchased from ChinaPeptides. Human transferrin (iron saturated) was obtained from MP Biomedicals (Solon, OH). Size exclusion chromatography column was packed from GE Healthcare Sephacryl S-300 (Uppsala, Sweden). All other reagents and starting materials were purchased from Aldrich or VWR and used without further purification unless otherwise

noted. Solutions were prepared from nanopure water purified from Milli-Q plus system (Millipore Co.), with a resistivity over 18 MΩ cm^{-1}. Thioflavin T (ThT) fluorescence was measured by a fluorescence spectrophotometer (LS-55, Perkin Elmer) at 25 ^{o}C with a slit width of 5 nm for both excitation and emission. Far-UV CD spectroscopy was measured on JASCO J-810. Atomic force microscopy was used by tapping mode with cantilever having a resonance frequency of ~170 kHz and typical force constant of 7.5 N/m.

3.2.2 Methods and Characterization

Synthesis of C-Dots and C-Dots transferrin conjugates

C-Dots and C-Dots transferrin conjugates used in the experiments were prepared and characterized according to our previous reported procedures.[200, 201] All characterizations consist with previous reported results. Briefly, sulfuric acid (36 mL) and nitric acid (12 mL) were added to 1 g of carbon nanopowder in a 100 mL flask. The mixture was heated with reflux to about 110 ^{o}C for 15 h in a sand bath. After the reaction, the acid was neutralized by sodium hydroxide. After 3 times crystallization to remove the salt generated and extraction by chloroform, the aqueous solution was dialyzed using MWCO 3500 bag against pure water for at least 4 days. Black powder was obtained after the removal of water. The characterizations of the as prepared C-Dots were identical to what we reported most recently using UV–vis spectroscopy, fluorescence, Fourier transform infrared spectrophotometry, X-ray photoelectron spectrometry, transmission electron microscopy, and atomic force microscopy. Solution-based zeta potential was characterized using a Zetasizer Nano ZS System (Malvern Inc., UK) with irradiation from a standard 633 nm laser.

A typical procedure to conjugate transferrin to C-Dots is as follows. 6.7 mg of 1-ethyl-3-(3-dimethylaminopropyl) carbodiimide hydrochloride (EDC) was added to 3 mL of 2.0 mg/mL C-Dots dispersed in phosphate-buffered saline (PBS, pH 7.4). The solution was stirred at the room temperature for 30 min, and a PBS solution (0.5 mL) of 4.0 mg N-hydroxysuccinimide (NHS) was added. The resulted solution was then stirred for 30 min before a PBS solution (2.5 mL) of transferrin (15.0 mg) was added. The mixture was then stirred for 2 h, and the resulted solution was subjected to a size exclusion chromatography column (Sephacryl S-300) for purification. For the dye-transferrin-C-Dots conjugates, the method of synthesis was similar but the amount of C-Dots, EDC, NHS and dye-transferrin was 2.0, 2.3, 1.3, and 2.0 mg, respectively. To conjugate 5-(aminomethyl) fluorescein to C-Dots (i.e. Fluor-C-Dots), 1.4 mg of 5-(aminomethyl) fluorescein hydrochloride in 100 μL dimethyl sulfoxide was added to 3 mL of 2.0 mg/mL C-Dots aqueous dispersion in PBS buffer at pH 7.4. After that, 6.7 mg EDC was added to the mixture. Then, the mixture was stirred under room temperature for 2 h, and the resulted solution was subjected to Sephacryl S-300 chromatography column for purification. In each case of conjugation, the elution was checked by fluorescence spectroscopy (Horiba Jobin Yvon Fluorolog–3). Slit width at the excitation and emission was set at 5 nm. The elution was kept if the fluorescence spectra showed the presence of C-Dots (excited using various wavelengths from 320 to 580 nm) and transferrin (excited at 280 nm) at the same time. If fluorescent dye was used, the fluorescence spectra of the kept elution needed to show the peak of the dye too. Sample was lyophilized to obtain solid transferrin-C-Dots, dye-transferrin-C-Dots and fluorescein-C-Dots.

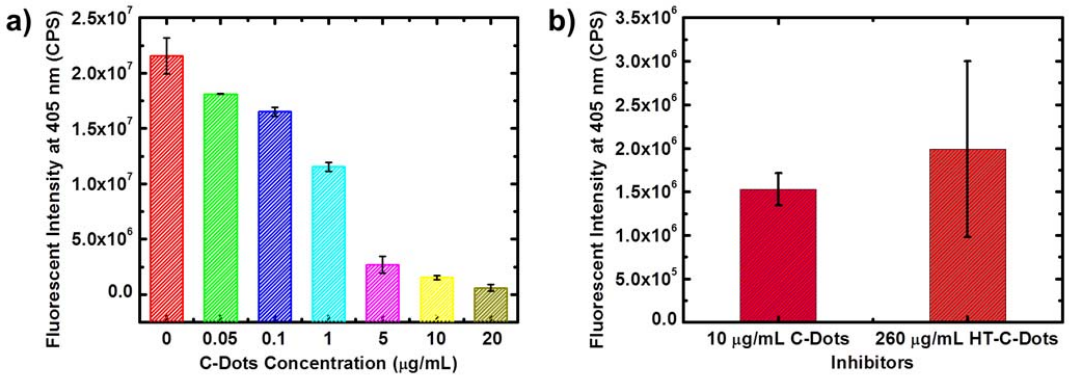

Figure 3.2 Inhibitory effect of a) different concentrations of C-Dots and b) HT-C-Dots on BACE1 activity determined by FRET assay. 260 μg/mL HT-C-Dots contains approximately 10 μg/mL C-Dots according to our previous published report.[176]

Fluorescence resonance energy transfer (FRET) assay

This assay was performed according to BACE1 Activity Detection Kit protocols (Sigma, St. Louis, MO). 500 μM BACE1 substrate solution was prepared by adding 0.5 mL of DMSO to the BACE1 substrate. Then the prepared 500 μM BACE1 substrate solution were diluted to 50 μM using fluorescent assay buffer. Each final tested samples contained 292 μL fluorescent assay buffer, 80 μL BACE1 substrate solution (50 μM), 8 μL BACE1 enzyme solution, and 20 μL different concentrations of C-Dots. Samples were incubated in dark at 37 ^{o}C for 3 h and terminated by a stop solution. The fluorescence was measured using 320 nm excitation and 405 nm emission wavelengths. The signal was obtained for three repeats of each sample. The error bars indicate the standard error of the mean.

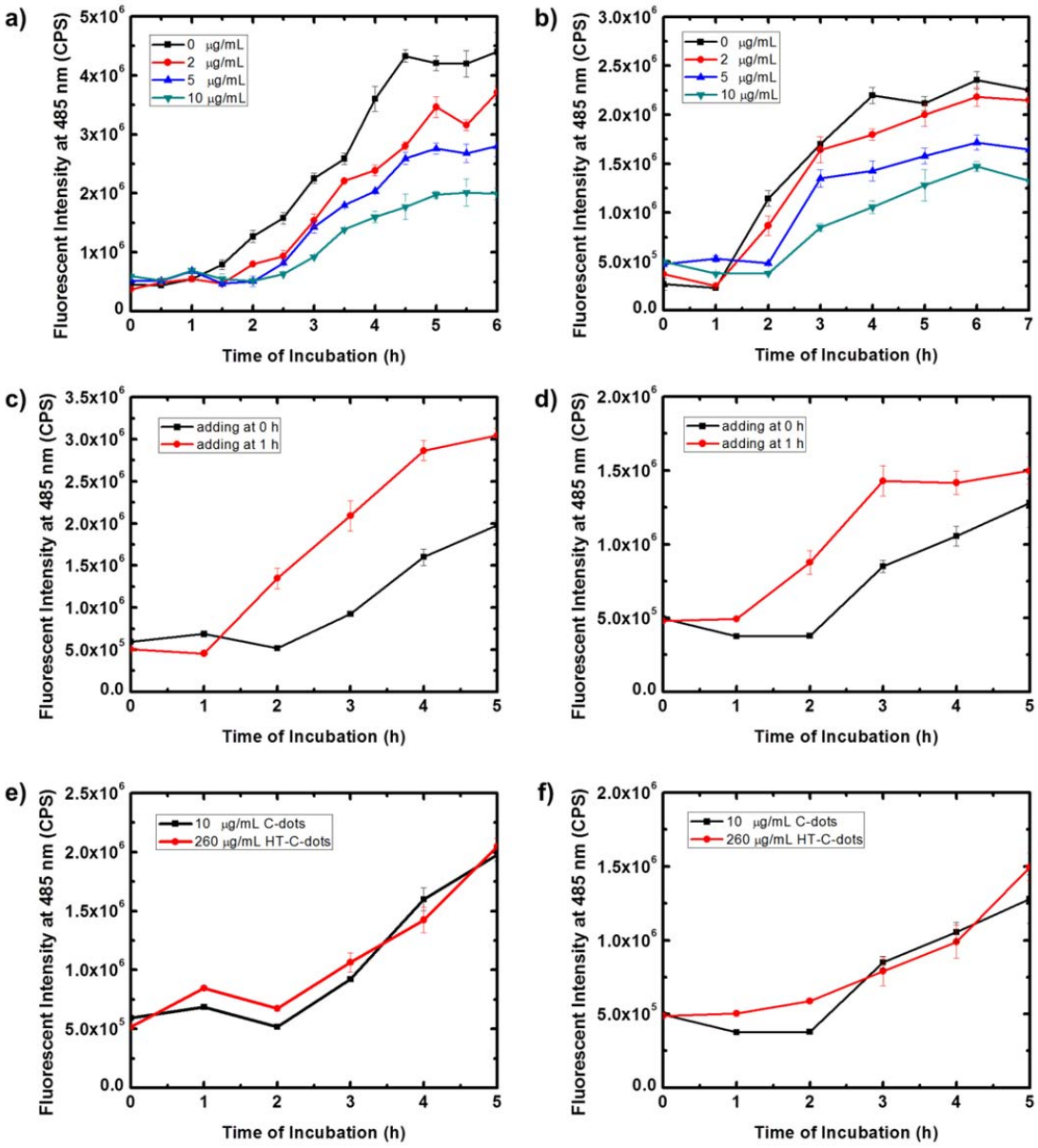

Figure 3.3 Kinetics of 10 μM of Aβ 42 fibrillation: fluorescence intensity of ThT at 485 nm as a function of incubation time at 37 ^{o}C in 25 mM PBS, pH 7.4 with 0, 2, 5, 10 μg/ml of C-Dots, respectively. The ThT fluorescence was obtained for three repeats of each sample. The error bars indicate the standard error of the mean.

Thioflavin T (ThT) fluorescence assay

The kinetics of Aβ 42 and Aβ 40 fibrillation can be characterized by the fluorescence increase of fibril‐specific dye of thioflavin T (ThT). To accomplish this, different concentrations of C-Dots, including 0, 2, 5, 10 μg/ml, were prepared for examination. At first, Aβ 42 and Aβ 40 were dissolved in 1,1,1,3,3,3-hexa-fluoroisopropanol. After evacuating the solvent, the solution was filtered through a 0.2 mm membrane to remove the pre-fibrils. Different concentrations of C-Dots were added to 10 μM Aβ in 25 mM PBS buffer solution (pH 7.4), respectively. Thereafter, the mixture were incubated at 37 ^{o}C, and aliquots of incubation solutions at different time points were collected and then diluted two times into ThT solution (25 mM ThT in 25 mM PBS buffer , pH 7.6). ThT fluorescence was measured by a fluorescence spectrophotometer (LS-55, Perkin Elmer) at 25 ^{o}C with a slit width of 5 nm for both excitation and emission. ThT emission was monitored at 480 nm with the excitation at 440 nm. The ThT fluorescence was obtained for three repeats of each sample. The error bars indicate the standard error of the mean.

Circular dichroism (CD) spectroscopy

To gain insights into the effects of C-Dots on the conformational transition of Aβ, far‐UV CD spectroscopy (JASCO J‐810) were utilized to monitor the secondary structure of Aβ over time. Similar to the fluorescence characterization, aliquots of ThT assay incubation solutions were collected for CD spectra. The spectra was recorded between 190 and 260 nm at room temperature by a 2 mm optical path length quartz cell.

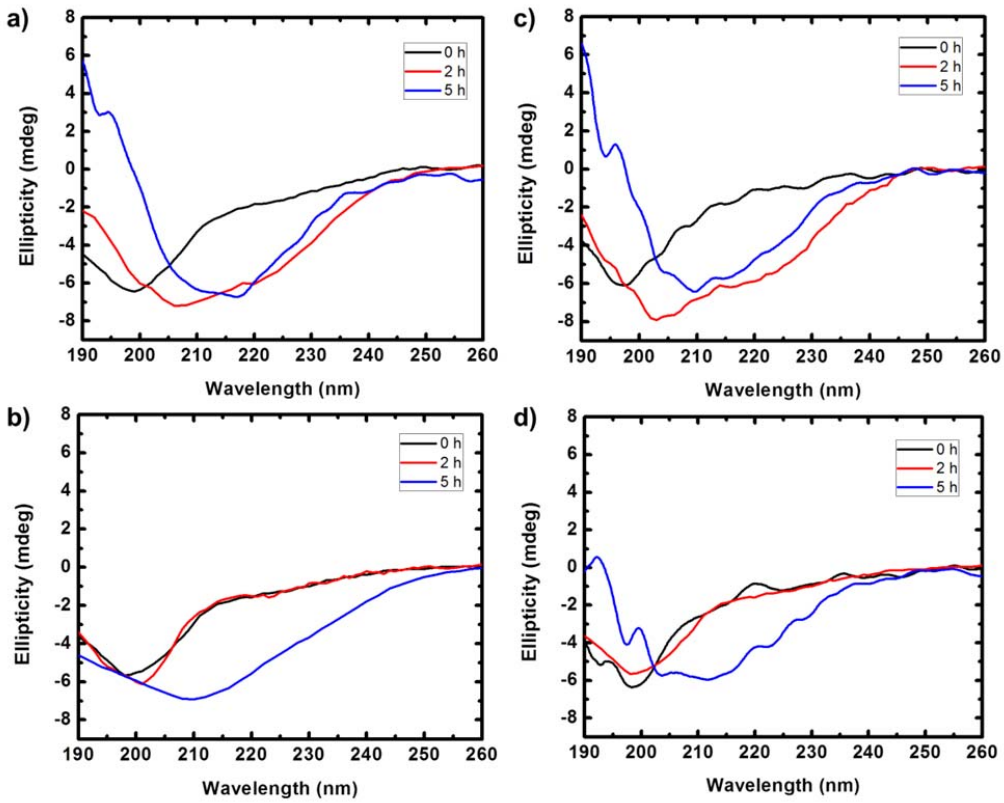

Figure 3.4 Far-UV circular dichroism spectra of 10 μM Aβ 42 incubated c) with 10 μg/ml C-Dots, and d) without C-Dots and c) 10 μM Aβ 40 incubated with 10 μg/mL C-Dots and d) without C-Dots in 25 mM pH = 7.4 PBS at 0, 2, 5 h.

Atomic force microscopy (AFM)

Tapping mode was used to observe morphologies during the fibrillation process. The cantilever has a resonance frequency of approximately 170 kHz with typical force constant of 7.5 N m^{-1}. Aliquots of samples withdrawn at different incubation times were diluted with pure water, drop-coated on a freshly cleaved mica surface, and allowed to dry for at least 1 h.

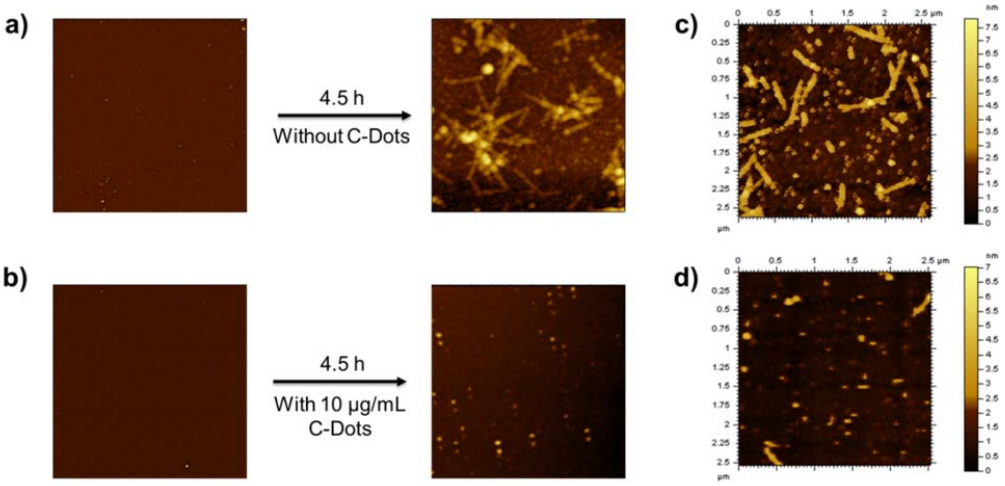

Figure 3.5 AFM images (size: 2.5 X 2.5 µm) of 10 µM Aβ 42 incubated a) in the absence of C-Dots, and, b) in the presence of 10 µg/ml C-Dots, and 10 µM Aβ 40 after 6 h, c) in the absence of C-Dots, and d) in the presence of 10 µg/ml C-Dots at 37 ^{o}C in 25 mM PBS, pH 7.4.

Cytotoxicity assay

Toxicity tests were performed in a new 96-well cell culture plate. In each well, health fertilized eggs (*Strongylocentrotus purpuratus sea urchins*) were incubated in 200 µL control sea water or 200 µL dilution of C-Dots in sea water. Aβ 42 fibrils and different Aβ 42 – C-Dots complex were collected, respectively. The test was performed at 15 °C for 24 hours until they reach hatching blastula stage embryos. 100 of embryos were examined and rate of embryo with normal development was calculated. Each experiment was repeated with similar results. The error bars indicate the standard error of the mean.

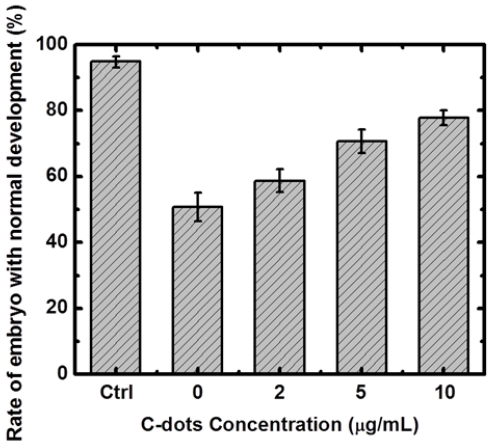

Figure 3.6 The inhibitory effect of C-Dots on the cytotoxicity of Aβ 42 fibrils at different concentrations of C-Dots. The control (ctrl) experiments showed the rate of embryo with normal development without C-Dots incubation.

Zebrafish injection and imaging

Wild-type zebrafish (*Danio rerio*) at 6 days after fertilization were obtained from the Zebrafish Core Facility at University of Miami. 4 nL of HT-C-Dots and C-Dots at 10 mg/mL PBS solution (pH 7.4) were injected into to the heart of anesthetized zebrafish by tricaine. After 5 h, Leica SP5 confocal microscope was used to observe the injected zebrafish under at 458 nm. The animal care protocol for all procedures used in this study was approved by the University of Miami Animal Care and Use Committee and complies with the guidelines of the National Institutes of Health.

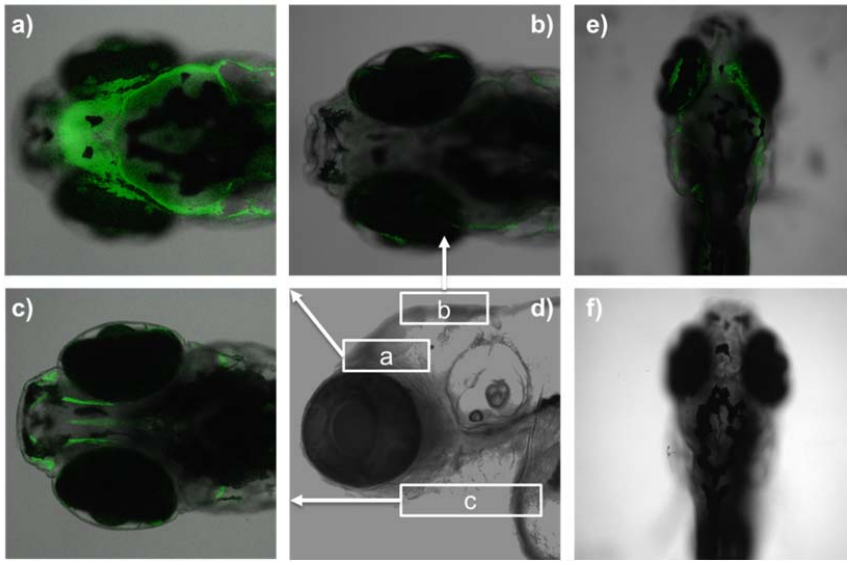

Figure 3.7 Confocal fluorescent images of a) brain, b) dorsal, c) ventral section, (d) lateral view of zebrafish after 5 h injection with C-Dots-HT conjugates, e) after 5 h injection with C-Dots, and f) without injections.

Simulation details

The CG model for Aβ monomers were converted from the PDB struc-ture (PDB code: 1Z0Q) by the Martinize python script (http://cgmartini.nl/index.php/tools2/proteins-and-bilayers). The C-Dot was modeled by coarse-grained beads densely packed to form a sphere with a radius of 2 nm. The surface of the C-Dots is either hydro-philic or hydrophobic. In the hydrophobic C-Dot, all beads were SC4 type (aromatic non-polar). In the hydrophilic C-Dot, the core beads were SC4 type while 2/3 of the surface beads were P1 (polar) or Qa (charged) type. The simulated systems consisted of one C-Dot and one Aβ monomer solvated in a cubic water box with a length of 17 nm. Counter ions and 0.15 mol/L NaCl were added to the solutions. For the hydrophilic or hydrophobic C-Dot system, a one-microsecond NVT simulations at 320 K was carried out. The integration time step was 20 fs. All simulation parameters were consistent with that used in the

parameterization of the Martini force field. GROMACS 4.5.3[202] was used for all the simulations.

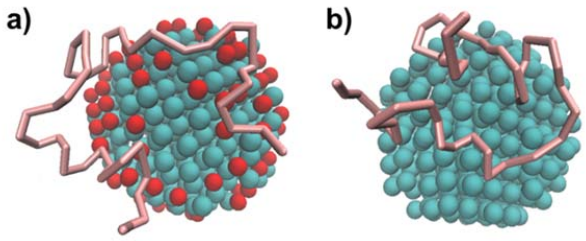

Figure 3.8 Aβ monomer binds to the C-Dot with a) hydrophilic surface and b) hydrophobic surface. Cyan spheres are the SC4 (aromatic carbon) and red spheres are Qa/P1 (COO-, C=O, OH) beads in the C-Dot. Pink sticks represent the backbone of Aβ 42 (PDB code: 1Z0Q).

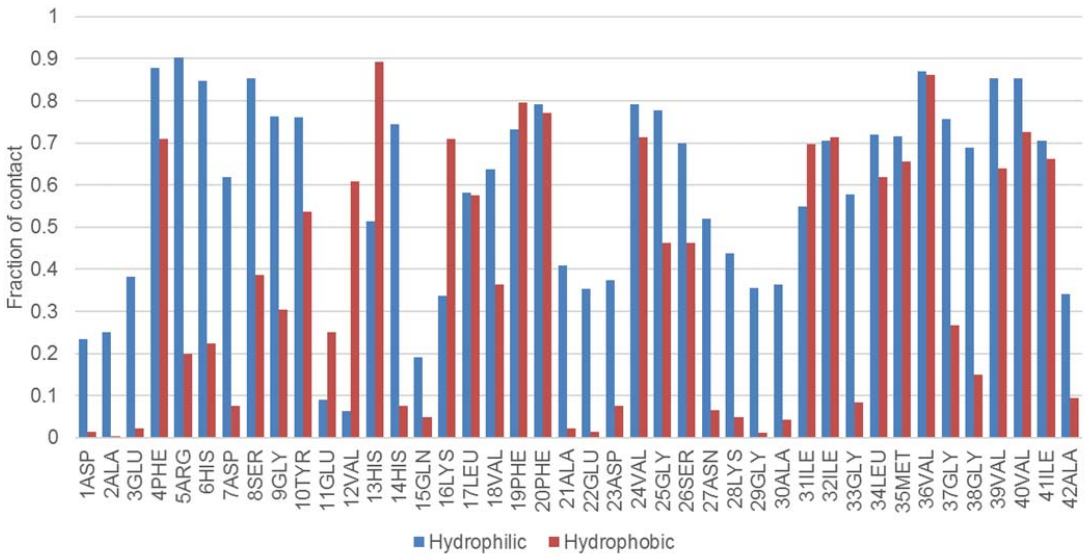

Figure 3.9 Fraction for each residue to be in contact with C-Dot. In general, the Aβ monomer has more contacts with the hydrophilic C-Dot than with the hydrophobic C-Dot. Most residues can have contacts with the hydrophilic C-Dot, while only part of the residues have contacts with the hydrophobic C-Dot.

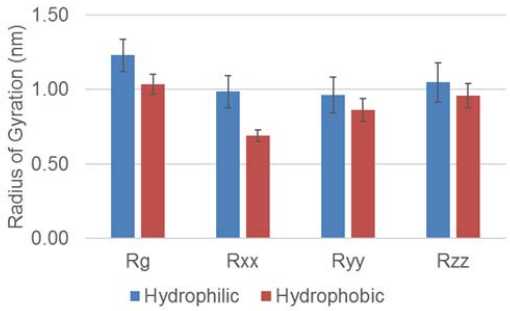

Figure 3.10 Radius of gyration of the Aβ monomer on the hydrophilic or hydrophobic surface. Error bars show the standard deviation. The uncertainties of the mean are negligible compared to the error bars. On the hydrophilic surface, the radius of gyration is larger with larger fluctuations, indicating that the structure of the Aβ monomer is more extended and flexible.

3.3 Results and Discussions

Initially, fluorescence resonance energy transfer (FRET) assay was employed to examine the effect of C-Dots on inhibition of BACE1 activity. In this assay, the substrate is attached to a fluorescence dye and a quenching group on each side, which significantly reduces the fluorescence of the substrate due to the FRET. Upon the cleavage of the substrate by the BACE1, the fluorescence of the substrate will be enhanced as a result of the disturbance of the FRET. As shown in Figure 3.2a, when incubating C-Dots in this FRET assay, the substrate fluorescence intensity decreased, and the higher concentration of C-Dots, the more effective the inhibition of C-Dots on BACE1 activity.

To evaluate the inhibition activity of C-Dots against Aβ fibrillation, different concentrations of C-Dots were prepared for thioflavin T (ThT) binding assay, where ThT exhibits enhanced fluorescence upon binding to amyloid fibrils so as to alter the fluorescent spectrum with the growth of fibrils. In the absence of C-Dots, the ThT profile of Aβ 42 showed a faster aggregation process, increasing immediately until it reached a

plateau by around 4.5 h. When introducing C-Dots at 0 h incubation, it illustrated that 1) the suppression of Aβ 42 can be observed with only 2 μg/mL C-Dots, and 2) the fluorescence intensity decreased at saturation with the increase of C-Dots concentration. However, adding 10 μg/mL C-Dots after 1 h incubation (Figure 3.2c), it promoted a faster Aβ 42 aggregation than that in the presence of 10 μg/mL C-dots before incubation, which strongly indicates C-Dots interact with Aβ 42 monomers to redirect fibril assembly at the early stage. The ThT profile of Aβ 40 demonstrated similar results (Figure 3.2b and 3.2d). Both Aβ 40 and Aβ 42, therefore, can be inhibited by C-Dots in a dose dependent manner. The ThT assay suggests potential utility of C-Dots for AD treatment, but the effect of C-Dots on cytotoxicity of Aβ 42 fibrils also needs to be addressed. Sea urchin embryos were selected as a model system, because 1) it has extreme sensitivity towards hazardous materials, and 2) it has been widely used for the static acute toxicity test. Aliquots of different ThT assay samples at 5 h were collected for the test. As shown in Figure 3.6, Aβ 42 fibrils reduced the rate of embryo with normal development to 51 %. If more C-Dots were added, the rate of embryo with normal development of sea urchin embryos would be restored, which strongly indicates that the formation of Aβ 42 toxic species can be delayed.

To attain a clearer perception of the effect of C-Dots on the conformational transition of Aβ, far-UV circular dichroism spectroscopy (CD) was utilized to monitor the secondary structure of Aβ 42 over time (Figure 3.4a and 3.4b). The Aβ peptides mainly adopt α-helical or random coin in the native conformation, while they undergo a conversion to β-strand during fibrillation process. Due to the effect of PBS buffer on the CD, both Aβ peptides spectra is in the form of disturbance but still distinguishable. As

illustrated in Figure 3.2b, in the absence of C-Dots, the initial secondary structure Aβ 42 is random coil with a representative negative band at around 198 nm. After 2 hours, this peak diminished and shifted slightly to approximately 207 nm, indicating the conformational switch of Aβ 42. Upon further aggregation, a negative valley, which is assigned to β sheet of mature peptide fibril, turned up at approximately 215 nm. In the presence of 10 μg/mL C-Dots, it exhibited a similar conformational transition as evidenced in Figure 3.2a. However, the structure of Aβ 42 did not completely convert to β sheet conformation after incubating 2 hours, resulting in the fact that C-Dots can potentially delay the conformational transition of Aβ 42. In the case of Aβ 40 alone, Figure 3.2c displayed a similar secondary structure to that of Aβ 42. With further peptide aggregation, bands shrink and there is a significant decrease in the negative absorption at around 198 nm, suggesting severe conformational changes. The final content of β strand at 5 h was much more than that of initial Aβ 40. In the presence of 10 μg/mL C-Dots, Aβ 40 showed a similar conformational transition with a delayed fibrillation process as evidenced in figure 3.2d, where the structural shift was observed when comparing 2 h curve in figure 3.2c and 3.2d. It is, thus, evidenced that C-Dots can partially suppress the fibrillation of Aβ 40 and 42.

The ability of C-Dots to inhibit Aβ aggregation was also investigated by atomic force microscopy (AFM), where the formation of these Aβ 42 and 40 fibrils can be directly observed and monitored (Figure 3.5). AFM images were obtained in the absence and presence of C-Dots, respectively, and the inhibition effect of C-Dots on Aβ peptides fibrillation consist with ThT profiles and CD spectra. As shown in Figure 3.5a and 3.5c, long Aβ 42 and 40 fibrils were apparent after 4.5 h incubation in the absence of C-Dots,

whereas less fibrils with a small amount of short protofibrils appeared during the incubation with C-Dots.

The experimental results revealed C-Dots can inhibit Aβ fibrillation. To obtain more details with regard to Aβ fibrillation by C-Dots, molecular dynamics simulations with the Martini coarse-grained (CG) force field[203] were performed to study the interaction between C-Dots and Aβ monomers, which has been a valuable tool for the study of Aβ peptides.[204-207] In this study, the surface of C-Dots has a high oxygen content,[200] which indicates high hydrophilicity. In order to see the role of the hydrophilic surface, C-Dots models with both hydrophilic and hydrophobic C-Dots were constructed.

The Aβ monomer can bind to the C-Dot with either hydrophilic or hydrophobic surface, but the binding modes and the structures of the Aβ monomer are distinct. The Aβ monomer has more contacts with the hydrophilic surface than with the hydrophobic surface. Most of the residues can interact with the hydrophilic surface through the backbone, while fewer residues have contacts with the hydrophobic surface (Figure 3.9 and 3.10), and PHE, ILE and LEU bind to the hydrophobic surfaces mainly through the side chains. As a result, the Aβ monomer forms more extended structures on the hydrophilic surface (Figure 3.8), and the structures on the hydrophobic surface are more compact. Analysis of the radius of gyration shows that the structural flexibility of the Aβ monomer is also higher on the hydrophilic surface. Previous experimental and computational studies suggest that increased flexibility inhibits fibril formation.[205, 208] Therefore, the extended structure and flexibility of the Aβ monomer induced by the hydrophilic C-Dots are possible mechanisms for the inhibition of fibrillation.

The key process to the success of the design of inhibitors is the delivery of BBB-impermeable nanomaterial or molecules into brain. To this end, we previously used HT to deliver the C-Dots across the BBB in a zebrafish model.[200] Herein, we followed the same procedure. Briefly, C-Dots loaded with HT were injected into the heart of anesthetized zebrafish at 5 days post-fertilization (dpf), where the maturation of its BBB developed as early as 3 dpf.[200] Confocal fluorescence microscopy was used to examine the brain sections of zebrafish in three dimensions by the normalized fluorescence intensity after 5 h injections. Figure 3.7a demonstrated that C-dots bind to forebrain with a higher affinity, comparing to the dorsal (Figure 3.7b) and ventral (Figure 3.7c) section images. In addition, the C-dots conjugates are still active in deactivating BACE1 and retarding Aβ fibrillation (Figure 3.3f). Combined with our previous studies, these results strongly suggest that C-Dots can be delivered across the BBB via a transferrin receptor-mediated mechanism and further help AD treatments.

3.4 Summary

In conclusion, the inhibitory effect of C-Dots on Aβ 42 and 40 fibrillation was verified by ThT assay, CD, and AFM. Molecular dynamics simulations showed that the hydrophilic surface of C-Dots can help Aβ fibrillation inhibition. C-Dots were also found to be effective in inhibiting BACE1 activity and delaying the formation of Aβ 42 toxic species in vitro, respectively. Given the tunable properties of C-Dots, transferrin was engineered onto its surface for the delivery crossing BBB in a zebrafish model. Combined with our previous results,[200] HT managed to deliver the C-Dots across the BBB to the forebrain section of zebrafish. To our knowledge, this is the first time for the application of C-Dots on AD treatment in terms of 1) Aβ fibrillation inhibition, 2) target

upstream secretases, 3) reduce the toxicity of Aβ 42 fibril, and 4) BBB penetration. C-Dots presented in this work, thus, display an excellent potential to be applied in pharmaceutical industry or other areas for the treatment of Alzheimer's disease.

Chapter 4 Ultrasensitive Plasmonic Biosensors for Real-Time Parallel Detection of Alpha-L-Fucosidase and Cardiac-Troponin-I in Whole Human Blood

4.1 Background

Novel therapies for disease prediction have increasingly been focused on in recent development of nanotechnology, and, of these, biomarker or biological marker, has begun to stand out as a competitor to be against other developed strategies,[209, 210] since the existence of any measurable specific substance can rapidly and correctly indicate the corresponding ongoing biological conditions.[211] While the interpretation of current costly and relatively complicated analysis methods, such as electrocardiography (ECG), magnetic resonance imaging (MRI), and computerized tomography (CT) scan, usually delay timely treatment, it is essential that biomarker arrays be implemented for parallel detection of several diseases to expedite clinical treatment.[212] Much work and progress has gone into multiple biomarkers detection,[213-215] especially immunoassay based sensing technology,[216] which includes colorimetric,[217] fluorescence,[218] paramagnetic,[219, 220] and electrochemical assay.[221] The methodologies to construct these immunoassays, for instance, horseradish peroxidase (HRP) initiated chemiluminometric assay,[43] fluorophore or peptide tags,[222, 223] and modified nanoparticle platform,[224, 225] generally require an antibody-antigen-antibody sandwiched structure. In a typical sandwiched immunoassay, at the sites where antigen can be recognized by the antibody immobilized on the surface at first, and followed by bounding to the functionalized secondary antibody which can display corresponding measurable properties, bottom-up assembly of hierarchical biological structures[1] are mainly employed as construction routes. However, the primary limiting factors in the conventional detection techniques concern cumbersome and low

sensitive platforms, which do not function well with whole human blood samples.[226, 227] For the improvement of cancers and many other diseases diagnosis, therefore, it is urgent that a novel strategy with simple but more accurate system for different biomarkers be developed.

Advanced development in the nanotechnology for the exploitation of localized surface plasmon resonances (LSPR)[228-230] – gold and silver nanoparticles exhibit such effects at visible and near-infrared frequencies[231] – in the applications of nanophotonics,[232-234] as well as biotechnology,[235, 236] have occurred in recent decades. Since the discovery of this label-free LSPR based biosensor,[237] it has demonstrated great potential to serve as a point-of-care testing (POCT) detector, where the medical diagnostic testing is in proximity to the patient's location. Even though there are other detection strategies to convert plasmon energy to electrical signal, most failed in the whole human blood test, and call for optical detection, making the overall sensing platform expensive and bulky integrate these sensors on a small chip.

Previously, we have explored plasmon-field-effect based thin film transistor with respect to highly efficient detections of plasmon energy, where a heavily doped n-type Si substrate serves as a back gate, and a n-type ZnO film that is deposited onto the thermally grown SiO_2 works as an active semiconductor channel.[238, 239] The gate bias incorporated in the device promotes an effective migration of induced hot electrons to cross the Schottky barrier generated between gold nanoparticle (AuNPs) and ZnO. The AuNPs utilized in the device displayed a strong plasmonic absorption at visible wavelength. By increasing the thickness of the surrounding medium of AuNPs via chemical coating, the effective refractive index can be changed, leading to the red shift in the plasmonic

absorption spectrum. Based on this previous work and to overcome primary scientific challenges described above, we developed an innovative plasmonic biosensor which is a photoconducting device with plasmonic Au nanostructures. Our plasmonic sensing platform with special architecture uses direct detection of the plasmonic energy induced by AuNPs. This function can resolve the issue of using colored medium that typically overlaps with light source wavelength. In addition to that, the small active area of the sensor, which is physically seperated from electrodes and effectively improves the number of times of bindings between the linker and the target antigen, not only requires a trivial amount of analyte, but endows a high integration capability with multiplexing.

4.2 Experimental Section

4.2.1 Materials

All solvents were purchased from commercial suppliers and used without further purification. All reagents and starting materials were purchased from Aldrich or VWR and used without further purification unless otherwise noted. Alpha-L-fucosidase and alpha-L-fucosidase antibody were purchased from Aldrich and MyBioSource, respectively. Cardiac troponin I and cardiac troponin I antibody were purchased from Hytest. Whole human blood were purchased from Aldrich. Solutions were prepared from nanopure water purified from Milli-Q plus system (Millipore Co.), with a resistivity over 18 MΩ.cm.

4.2.2 Methods and Characterization

Plasmon biosensor fabrication

Initially, a glass substrate was rinsed in acetone, methanol, and DI water for 15 min, respectively. A thin n-type semiconductor film was then deposited onto the channel layer.

A typical photolithography process and a wet etching process were utilized for the channel isolation. To create electrodes, metal layers were deposited by electron beam evaporation. The device became a fully functional plasmon biosensor after the lift-off process. The fabricated sensors were characterized regarding their electrical performance before gold nanoparticles (AuNPs) were incorporated onto the active layers. Finally, Au was patterned onto the top of the semiconductor channel. The images of the device structure are shown in Figure 4.1.

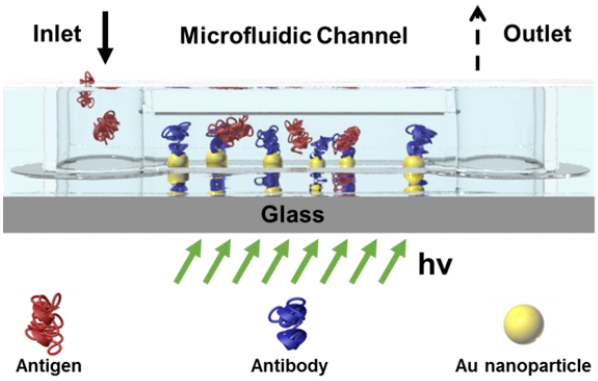

Figure 4.1 The fabricated plasmon biosensor with microfluidic channel.

Microfluidic channel fabrication

The dimensions of microfluidic channel were selected according to the device size. The injection was done using a commercial needle, making this device more suitable for mass production and industrial use. Figure 4.2 displays the microfluidic channel mold pattern on top of the device. In addition, the following process was followed to fabricate the microfluidic channel:

1. Prepare Polydimethylsiloxane (PDMS) molding solution

Mix Sylgard 184 Base with Curing Agent at a ratio of 10 (base, 25 g) to 1 (curing agent, 2.5 g) by weight for 15 mins.

2. Remove all bubble from molding solution (PDMS)

Put the PDMS in Vacuum Chamber (Vacuum 25 psi for 15 mins twice)

3. Molding

a) Put a patterned wafer in a petri dish.

b) Pour PDMS on the wafer.

c) Remove bubble again by using pipette (without vacuum chamber).

d) Put the Petri dish on an optical table, and wait for a day

4. Remove mold and Cut the patterned PDMS

5. Attach microfluidic PDMS to the device

a) Expose the device to ozone plasmon for 30 mins

b) Put the PDMS on the device by using Mask Aligner

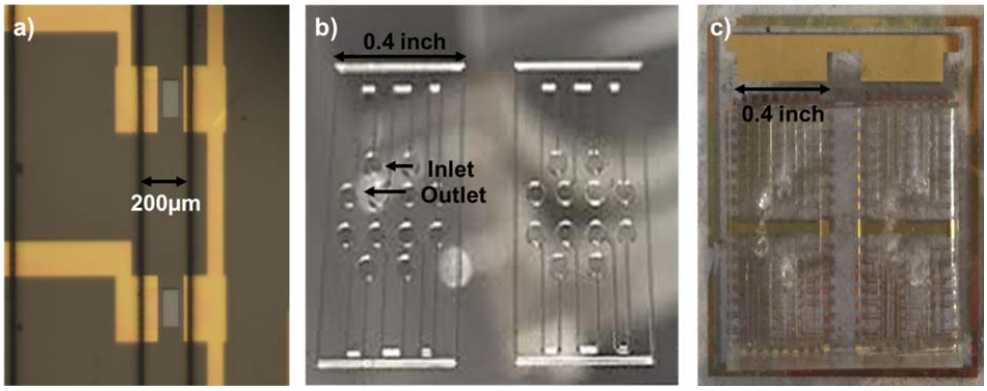

Figure 4.2 a) Optical microscopy image of the integrated device. b) Microfluidic channel mold. c) Integration of microfluidic channel with the fabricated sensor.

Electro Optical Characterization.

One source meter was employed to provide the voltage biases for the electrical characterization of plasmonic sensor (Figure 4.3). The spectral response measurement was carried out at the probe station. The optical measurement system is made up of a lamp, a lock-in amplifier, and appropriate optical filters. The light power was measured using a NIST calibrated silicon photodetector and an optical power meter for the spectral response calculation.

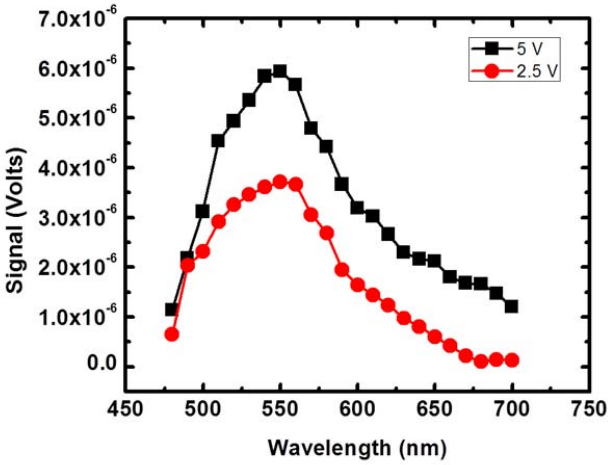

Figure 4.3 Optical response of plasmonic sensor

Sensor packaging and measurement

As depicted in the figure 4.4, a housing for the sensor was 3D printed. In this housing, a light emitting diode (LED) was placed at bottom of the sensor. The sensors were connected to the lock-in amplifier as mentioned in the previous section using the probe station. All the measured sensors were placed exactly in the middle of the circular hole to maximize the optical response.

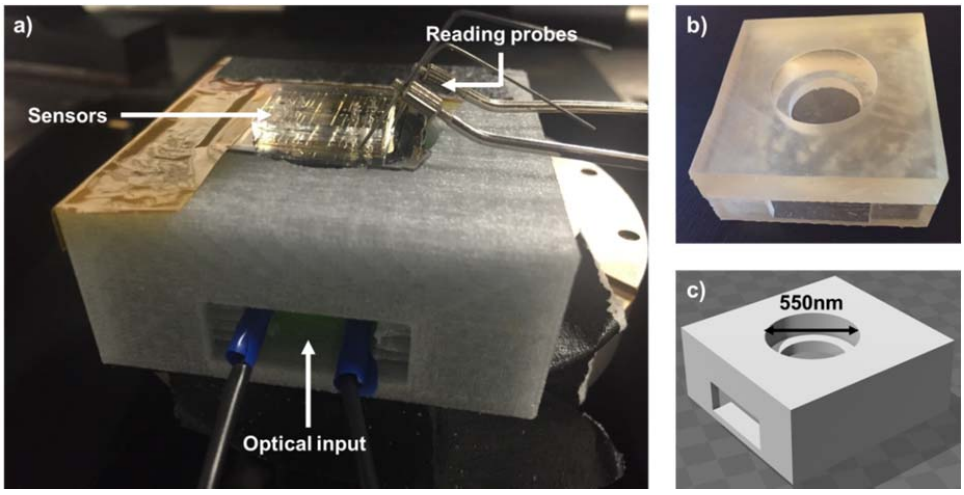

Figure 4.4 a) Sensing platform with b) the housing packaging 3D printed from c) the model.

4.3 Results and Discussions

To demonstrate the plasmonic sensor operation, we selected two specific biomarkers: 1) alpha-L-fucosidase (AFU), a valuable diagnostic biomarker for hepatocellular carcinoma (HCC),[240] and 2) cardiac troponin I (cTnI), a blood borne biomarker associated with cardiovascular diseases (CVD).[95] It is claimed that HCC, as the primary malignancy of liver cancer, remains one of the most frequent and deadly cancers worldwide, while CVD is considered to be the leading global cause of death, accounting for 17.3 million deaths each year.[95, 240] The concentration of AFU and cTnI – it has proven to increase after the onset of diseases – to separate the normal people from patients are suggested to be 50 U/L and 0.5 to 2.0 ng/mL,[95, 241] respectively. Through several careful measurements, herein, we show that the limit of detection (LOD) of the proposed fabricated biosensor is much lower than the above defined borderline concentration of AFU and cTnI. Compared to other detecting approaches, the developed novel device performed much better with respect to several parameters. The chip design

of this portable parallel biomarker detector, and the analysis of AFU and cTnI biosensing using PBS buffer and whole human blood will be described in the following section.

The plasmon biosensor, placed in a 3D printed housing accompanied with a light at the bottom (Figure 4.4), was fabricated on a glass substrate with a thin n-type semiconductor film. We created two electrodes by depositing electrode layers, and the device in turn became a metal-semiconductor-metal photoconductor. AuNPs thereafter were incorporated on the thin semiconductor film, which accomplished photo response from the plasmonic absorption in photocoductor. The fabricated devices were characterized using a custom electro-optical measurement setup. The electrical properties were detected using a source meter, and the plasmonic spectral response was measured using a modulated monochromatic light with a lock-in amplifier while the device was biased with DC voltage. We used a customized LabView program that controls the monochromator, the lock-in amplifier and picoam meter to obtain automated computerized measurements. Based on this preliminary characterization of the sensing unit, we identified the best conditions for voltage bias and the wavelength for optical response. The monochromatic light was delivered through the glass substrate (bottom of the sensor). This configuration enables a direct illumination of LED light to the plasmonic AuNPs. Therefore, there is no light absorption by the blood in the fluidic channel.

To minimize the sample size, and for further achievement in multiplexing detection for AFU and cTnI, a poly(dimethylsiloxane) (PDMS) based microfluidic channel was built by polymer casting. Followed by releasing it from the mold, the prepared microfluidics, where present four independent microchannel, were carefully aligned onto

the biosensor by utilizing optical microscopy. Next, 1 mM 3-mercaptopropionic acid (MPA) ethanolic solution was injected into the microfluidic channel to modify the AuNPs overnight. In such a way human cTnI antibody can be conjugated onto the AuNPs via 1-ethyl-3-(-3-dimethylaminopropyl) carbodiimide hydrochloride (EDC) and N-hydroxysuccinimide (NHS) chemistry. After 1 hour incubation, bovine serum albumin (BSA) was added to block the non-specific binding site.

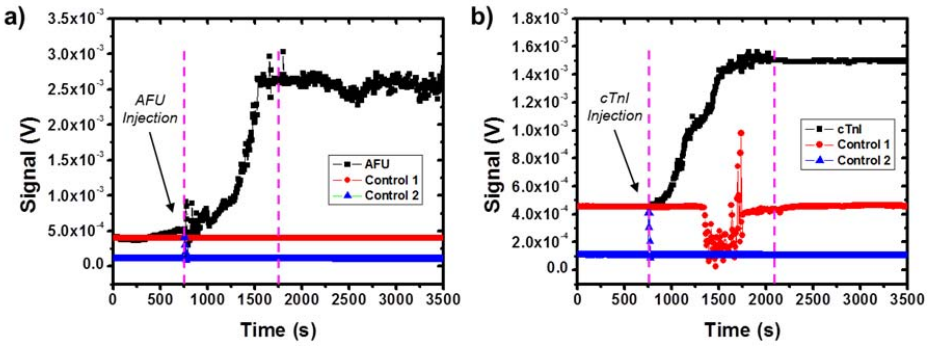

Figure 4.5 Real-time measurement of a) AFU and b) cTnI detection with blind protein control (red line) and gold nanoparticle control (blue line). The mixed PBS buffer solutions with 4 U/L AFU and 0.5 ng/mL cTnI were injected into the biosensor at 750 s, respectively. The signal got stabilized at around 1750 s.

To confirm the effectiveness of such a device in sensing technology, AFU and cTnI detection were performed by the injection of the prepared samples in PBS buffer (pH = 7.4) into the microfluidic channel, respectively, with the sensor being turned on earlier. Figure 4.5 shows the real-time measurement where the current fluctuates violently upon the injection of the sample, especially injecting AFU. Since the voltage signal relates to the thickness of the AuNPs, such fluctuation is attributed to the collision of the antigen

against the modified AuNPs, which reflects the whole process of binding recognition of antibody-antigen interactions. As is illustrated in Figure 4.5, the antigen absorbance intensity increases were recorded as a function of time, and the signal got stabilized in approximately 1000 s after the injection, which suggests the accomplishment of the antibody-antigen binding event. By plotting the signal against different AFU and cTnI concentrations, LOD was calculated to be 0.016 U/L and 0.015 ng/mL, respectively (Figure 4.6). To further confirm the working principle, a series of control experiments, including the sensing platform without AuNPs, and blind protein detection were performed, respectively. AuNP is the key to the whole detection mechanism, and missing of AuNPs, or the physiological absorption of AFU or cTnI to the detection platform surface, thus, present no results with regard to the detection of biomarkers, which is consistent with Figure 4.5 where followed the same procedure as described above except AuNPs attachment. Other than AFU and cTnI, insulin was also injected into the cTnI biosensor as a blind protein sensing test, but as expected, no significant bindings were observed in the detection window due to little binding of nonspecific secondary antibody to insulin, which in turn confirms the specificity of the constructed biosensor.

As is known, protein adopts different conformations in different environments, resulting in an impact on the antibody-antigen interactions. The whole human blood has one of the most complex matrices that create lots of false readings. Whether the developed device can be applied to the whole human blood or not is the dominant scientific challenge, particularly for the optical sensing technology due to the absorption from the blood. To this end, our sensing platform uses a wide-bandgap semiconducting material (IGZO) which is transparent at visible to infrared spectrum. Therefore, we can

excite the plamonic nanostructure from the other side of microfluidic channel filled with blood. Conventional surface plasmon resonance system with an Au film surface uses similar excitation structure. But our sensor system uses much smaller sensing area that allows excellent minimum detection limit. The other advantage of our plasmonic platform is a strong signal-to-noise ratio. We use a lock-in amplification approach by modulating the excitation light and take the response signal only from the specific modulation frequency. This approach eliminates other noises from the ionic strength in the medium, pH change, to temperature fluctuations. As a proof-of-concept, whole human blood was selected for investigation on the AFU and cTnI detection. 40 U/L AFU and 0.1 ng/mL cTnI were mixed with whole human blood, respectively, followed by injection into the microfluidic channel immediately. By comparing the control experiment (whole human blood without any biomarkers), Figure 4.7 demonstrates a similar curve – the sensing signals are over 12 % in contrast to the pure whole human blood control results – to previous tests in detection measurements, thus confirming that this portable plasmonic biosensor has a great potential for future clinical analysis.

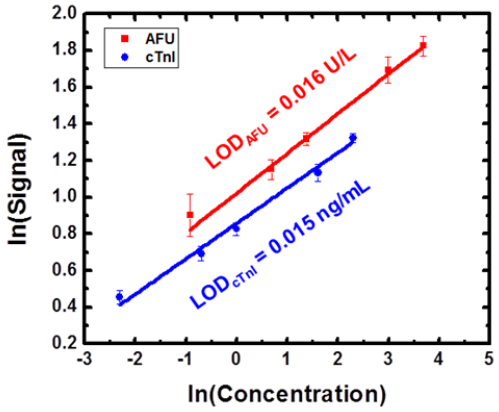

Figure 4.6 The plot of different concentrations of AFU (red spots) and cTnI (blue spots) against their corresponding signals.

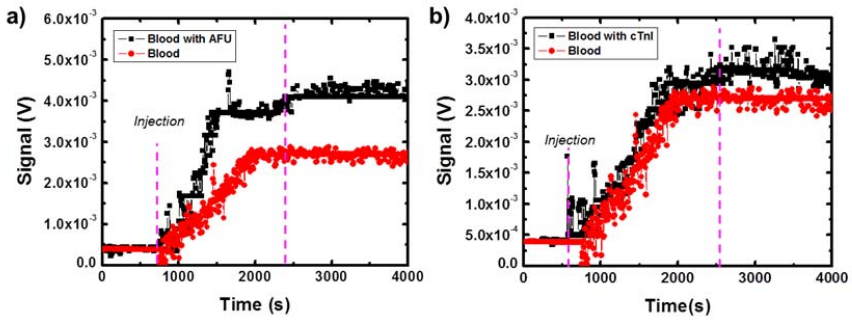

Figure 4.7 Real-time measurement of detecting a) 40 U/L AFU and b) 0.1 ng/mL cTnI mixed with whole human blood, respectively, and the control experiments with the pure whole human blood (red spots).

4.4 Summary

In conclusion, the portable plasmonic biosensor was fabricated by incorporating microfluidic channel with designed microchip. The AuNPs embedded into the channel of the microchip were conjugated with specific antibodies to enable the specificity of the whole system. Furthermore, the developed biosensor has significant potential for POCT, as well as capability for real time dynamic interaction monitoring of different biomarkers at the same time in a parallel fashion. Considering the high sensitivity towards AFU and cTnI, where the LOD is calculated to be 0.016 U/L and 0.015 ng/mL, respectively, and the wide applicable strategies for other biomarkers along with the excellent platform for whole human blood samples, this plamonic biosensor can help lead to breakthroughs in the sensing nanotechnology and future clinical use.

Chapter 5 Conclusion

Within cells, nature assembly is directed by the information encrypted in the biomacromolecules mainly made up of proteins, nucleic acids and lipids.[1] These molecules are primarily responsible for most biological related functions, such as bio-reactions, cell signaling and ligand binding, genetic information as well as the construction of biological bodies. The slight change in structures could lead to dramatic alternation in the biological functions, producing a negative impact on individuals. Significant efforts, therefore, have been devoted to investigating the structures of these biomacromolecules, so as to control the functions altered by the assembly, and of these, nanomaterials chemistry has played an essential role in the last few decades.[196] However, the concern arisen with the nanomaterials include the uncertainty of their interactions with biomacromolecules, even though the exceptional benefits these nanomaterials derive to the scientific community. In order to resolve this dilemma, we are trying to mimic and redirect the assembly process for biomedical application.

Inhibition of Protein Fibrillation in the Extracellular Space by Redirecting Nature Assembly

Amyloid-β peptides (Aβ) fibrillation is the hallmark of Alzheimer's disease (AD). However, it has been challenging to discover potent agents in order to inhibit Aβ fibrillation. In my PhD career, I demonstrated the effect of resorcinarene[191] and carbon dots on inhibiting Aβ fibrillation in vitro via experimental and computational methods. Aβ were incubated with different concentrations of our agents so as to monitor the kinetics by using thioflavin T binding assay. The results, which were further confirmed by far-UV CD spectroscopy and atomic force microscopy, strongly indicated that the

higher concentration of our agents, the more effective the inhibition of Aβ fibrillation. A cytotoxity study showed that when sea urchin embryos were exposed to our agents, the majority survived due to their low toxicity. When our agents were added, the formation of toxic Aβ 42 species was delayed. In addition, advantages arisen with the carbon dots include 1) target upstream secretases, BACE1 and 2) BBB penetration. Computational studies of Aβ fibrillation, including docking simulations and MD simulations, illustrated that the interaction between inhibitor resorcinarene and Aβ is driven by the non-polar interactions, and molecular dynamics simulations showed that the hydrophilic surface of C-Dots can help Aβ fibrillation inhibition. These studies display a novel strategy for the exploration of promising antiamyloiddogenic agents for AD treatments, wherein we also successfully used resorcinarene and carbon dots to redirect the peptide aggregation assembly.

Biosening Nanotechnology by Mimicking Nature Assembly

Cancers and many other diseases, such as hepatocellular carcinoma (HCC) and cardiovascular diseases (CVD), have threatened human lives for centuries.[95] A novel technique for such disease prediction, therefore, is in an urgent demand for timely treatment. Biomarkers - alpha-L-fucosidase (AFU) for HCC and cardiac troponin I (cTnI) for CVD - have proven to be essential in the role of disease detection. In my PhD career, I investigated an ultrasensitive plasmonic biosensor that converts plasmonic absorption to electrical current in order to detect AFU and cTnI in buffer and in whole human blood in real time parallel fashion. The detection limit was calculated to be 0.016 U/L for AFU and 0.015 ng/mL for cTnI in PBS buffer solution, respectively. Combined with the versatility of the strategies for different biomarkers, these results demonstrate that the

developed biosensor, wherein mimicking the nature assembly, exhibits a promising application for the prediction of cancers and many other disease.

WORKS CITED

1. Han, X.; Zheng, Y. T.; Munro, C. J.; Ji, Y. W.; Braunschweig, A. B. *Curr. Opin. Biotechnol.* **2015**, *34*, 41-47.

2. Lashuel, H. A.; Hartley, D.; Petre, B. M.; Walz, T.; Lansbury, P. T. *Nature* **2002**, *418*, 291-291.

3. Roman, G. C. *J. Neurol. Sci.* **2002**, *203*, 7-10.

4. Prince, M.; Bryce, R.; Albanese, E.; Wimo, A.; Ribeiro, W.; Ferri, C. P. *Alzheimers Dement.* **2013**, *9*, 63-75.

5. Fredriksen-Goldsen, K. I.; Jen, S.; Bryan, A. E.; Goldsen, J. *J. Appl. Gerontol.* **2016**, 0733464816672047.

6. Hardy, J.; Selkoe, D. J. *Science* **2002**, *297*, 353-356.

7. Klein, W. L.; Krafft, G. A.; Finch, C. E. *Trends Neurosci.* **2001**, *24*, 219-224.

8. Alwan, A. *Global Status Report on Noncommunicable Diseases 2010*; Geneva, 2011.

9. Heidenreich, P. A.; Trogdon, J. G.; Khavjou, O. A.; Butler, J.; Dracup, K.; Ezekowitz, M. D.; Finkelstein, E. A.; Hong, Y. L.; Johnston, S. C.; Khera, A.; Lloyd-Jones, D. M.; Nelson, S. A.; Nichol, G.; Orenstein, D.; Wilson, P. W. F.; Woo, Y. J.; Amer Heart Assoc Advocacy Coordina; Stroke Council; Council Cardiovasc Radiology Inter; Council Clinical Cardiology; Council Epidemiology Prevention; Council Arteriosclerosis Thrombosi; Council Cardiopulmonary Critical C; Council Cardiovasc Nursing; Council Kidney Cardiovasc Dis; Council Cardiovasc Surgery Anesthe *Circulation* **2011**, *123*, 933-944.

10. Song, S. Y.; Han, Y. D.; Kim, K.; Yang, S. S.; Yoon, H. C. *Biosens. Bioelectron.* **2011**, *26*, 3818-3824.

11. McDonnell, B.; Hearty, S.; Leonard, P.; O'Kennedy, R. *Clin. Biochem.* **2009**, *42*, 549-561.

12. Suprun, E.; Bulko, T.; Lisitsa, A.; Gnedenko, O.; Ivanov, A.; Shumyantseva, V.; Archakov, A. *Biosens. Bioelectron.* **2010**, *25*, 1694-1698.

13. Wang, J. Y.; Wang, X. Q.; Ren, L.; Wang, Q.; Li, L.; Liu, W. M.; Wan, Z. F.; Yang, L. Y.; Sun, P.; Ren, L. L.; Li, M. L.; Wu, H.; Wang, J. F.; Zhangt, L. *Anal. Chem.* **2009**, *81*, 6210-6217.

14. Kannel, W. B.; Stokes, J.; Abbott, R. D. *Circulation* **1984**, *70*, 160-160.

15. Strimbu, K.; Tavel, J. A. *Curr. Opin. Hiv Aids* **2010**, *5*, 463-466.

16. Daubert, M. A.; Jeremias, A. *Vasc. Health Risk Manage.* **2010**, *6*, 691-699.

17. Apple, F. S.; Wu, A. H.; Jaffe, A. S.; Panteghini, M.; Christenson, R. H.; Cannon, C. P.; Francis, G.; Jesse, R. L.; Morrow, D. A.; Newby, L. K. *Circulation* **2007**, *116*, e95-e98.

18. Alpert, J. S.; Thygesen, K.; Antman, E.; Bassand, J. P. *J. Am. Coll. Cardiol.* **2001**, *37*, 973-973.

19. Alpert, J. S.; Antman, E.; Apple, F.; Armstrong, P. W.; Bassand, J. P.; de Luna, A.B.; Beller, G.; Breithardt, G.; Chaitman, B. R.; Clemmensen, P.; Falk, E.; Fishbein, M. C.; Galvani, M.; Garson, A.; Grines, C.; Hamm, C.; Hoppe, U.; Jaffe, A.; Katus, H.; Kjekshus, J.; Klein, W.; Klootwijk, P.; Lenfant, C.; Levy, D.; Levy, R. I.; Luepker, R.; Marcus, F.; Naslund, U.; Ohman, M.; Pahlm, O.; Poole-Wilson, P.; Popp, R.; Pyorala, K.; Ravkilde, J.; Rehnquist, N.; Roberts, W.; Roberts, R.; Roelandt, J.; Ryden, L.; Sans, S.; Simoons, M. L.; Thygesen, K.; Tunstall-Pedoe, H.; Underwood, R.; Uretsky, B. F.; de Werf, F. V.; Voipio-Pulkki, L. M.; Wagner, G.; Wallentin, L.; Wijns, W.; Wood, D.; Amer, J. E. S. C. *Eur. Heart J.* **2000**, *21*, 1502-1513.

20. Panteghini, M.; Pagani, F.; Yeo, K. T. J.; Apple, F. S.; Christenson, R. H.; Dati, F.;Mair, J.; Ravkilde, J.; Wu, A. H. B. *Clin. Chem.* **2004**, *50*, 327-332.

21. St-Louis, P. *Clin. Biochem.* **2000**, *33*, 427-440.

22. von Lode, P. *Clin. Biochem.* **2005**, *38*, 591-606.

23. Wilkinson, J. M.; Grand, R. J. A. *Nature* **1978**, *271*, 31-35.

24. Apple, F. S.; Collinson, P. O. *Clin. Chem.* **2012**, *58*, 796-796.

25. Vallins, W. J.; Brand, N. J.; Dabhade, N.; Butlerbrowne, G.; Yacoub, M. H.; Barton, P. J. R. *Febs. Lett.* **1990**, *270*, 57-61.

26. Babuin, L.; Jaffe, A. S. *Can. Med. Assoc. J.* **2005**, *173*, 1191-1202.

27. Maqsood, A.; Kaid, K.; Cohen, M. *Internet J. of Cardiovasc. Res.* **2006**, *4*, 1-4.

28. Ahammad, A. J. S.; Choi, Y. H.; Koh, K.; Kim, J. H.; Lee, J. J.; Lee, M. *Int. J. Electrochem. Sci.* **2011**, *6*, 1906-1916.

29. Wu, A. H. B.; Apple, F. S.; Gibler, W. B.; Jesse, R. L.; Warshaw, M. M.; Valdes, R. *Clin. Chem.* **1999**, *45*, 1104-1121.

30. Shan, M.; Li, M.; Qiu, X. Y.; Qi, H. L.; Gao, Q.; Zhang, C. X. *Gold. Bull.* **2014**, *47*, 57-64.

31. Ellenius, J.; Groth, T.; Lindahl, B.; Wallentin, L. *Clin. Chem.* **1997**, *43*, 1919-1925.

32. Storrow, A. B.; Gibler, W. B. *Clin. Chim. Acta* **1999**, *284*, 187-196.

33. Liu, J.; Zhang, L. L.; Wang, Y. S.; Zheng, Y.; Sun, S. H. *Measurement* **2014**, *47*, 200-206.

34. Shen, J. W.; Li, Y. B.; Gu, H. S.; Xia, F.; Zuo, X. L. *Chem. Rev.* **2014**, *114*, 7631-7677.

35. Engvall, E.; Perlmann, P. *Immunochemistry* **1971**, *8*, 871-874.

36. Cho, I. H.; Paek, E. H.; Kim, Y. K.; Kim, J. H.; Paek, S. H. *Anal. Chim. Acta* **2009**, *632*, 247-255.

37. Wu, A. H. B.; Fukushima, N.; Puskas, R.; Todd, J.; Goix, P. *Clin. Chem.* **2006**, *52*, 2157-2159.

38. Todd, J.; Freese, B.; Lu, A.; Held, D.; Morey, J.; Livingston, R.; Goix, P. *Clin. Chem.* **2007**, *53*, 1990-1995.

39. Masson, J. F.; Obando, L.; Beaudoin, S.; Booksh, K. *Talanta* **2004**, *62*, 865-870.

40. Periyakaruppan, A.; Gandhiraman, R. P.; Meyyappan, M.; Koehne, J. E. *Anal. Chem.* **2013**, *85*, 3858-3863.

41. Dorraj, G. S.; Rassaee, M. J.; Latifi, A. M.; Pishgoo, B.; Tavallaei, M. *J. Biotechnol.* **2015**, *208*, 80-86.

42. Cummins, B.; Auckland, M. L.; Cummins, P. *Am. Heart J.* **1987**, *113*, 1333-1344.

43. Torabi, F.; Far, H. R. M.; Danielsson, B.; Khayyami, M. *Biosens. Bioelectron.* **2007**, *22*, 1218-1223.

44. Choi, D. H.; Lee, S. K.; Oh, Y. K.; Bae, B. W.; Lee, S. D.; Kim, S.; Shin, Y. B.; Kim, M. G. *Biosens. Bioelectron.* **2010**, *25*, 1999-2002.

45. Wu, W. Y.; Bian, Z. P.; Wang, W.; Wang, W.; Zhu, J. J. *Sensor. Actuat. B-Chem.* **2010**, *147*, 298-303.

46. Stringer, R. C.; Hoehn, D.; Grant, S. A. *Ieee. Sens. J.* **2008**, *8*, 295-300.

47. Kar, P.; Pandey, A.; Greer, J. J.; Shankar, K. *Lab Chip* **2012**, *12*, 821-828.

48. Aslan, K.; Grell, T. A. *Clin. Chem.* **2011**, *57*, 746-752.

49. Jarvenpaa, M. L.; Kuningas, K.; Niemi, I.; Hedberg, P.; Ristiniemi, N.; Pettersson, K.; Lovgren, T. *Clin. Chim. Acta* **2012**, *414*, 70-75.

50. Lee, S.; Kang, S. H. *Talanta* **2013**, *104*, 32-38

51. Bruls, D. M.; Evers, T. H.; Kahlman, J. A. H.; van Lankvelt, P. J. W.; Ovsyanko, M.; Pelssers, E. G. M.; Schleipen, J. J. H. B.; de Theije, F. K.; Verschuren, C. A.; van der Wijk, T.; van Zon, J. B. A.; Dittmer, W. U.; Immink, A. H. J.; Nieuwenhuis, J. H.; Prins, M. W. J. *Lab Chip* **2009**, *9*, 3504-3510.

52. Kiely, J.; Hawkins, P.; Wraith, P.; Luxton, R. *Iet. Sci. Meas. Technol.* **2007**, *1*, 270-275.

53. Dittmer, W. U.; Evers, T. H.; Hardeman, W. M.; Huijnen, W.; Kamps, R.; de Kievit, P.; Neijzen, J. H. M.; Nieuwenhuis, J. H.; Sijbers, M. J. J.; Dekkers, D. W. C.; Hefti, M. H.; Martens, M. F. W. C. *Clin. Chim. Acta* **2010**, *411*, 868-873.

54. Zhou, F.; Lu, M.; Wang, W.; Bian, Z. P.; Zhang, J. R.; Zhu, J. J. *Clin. Chem.* **2010**, *56*, 1701-1707.

55. Bhalla, V.; Carrara, S.; Sharma, P.; Nangia, Y.; Suri, C. R. *Sens. Actuators B* **2012**, *161*, 761-768.

56. Jiang, S. H.; Fan, T.; Liu, L. J.; Chen, Y.; Zhang, X. Q.; Sha, Z. L.; Liu, Y. L.; Zhang, J. K. *Prog. Biochem. Biophys.* **2014**, *41*, 916-920.

57. Kwon, Y. C.; Kim, M. G.; Kim, E. M.; Shin, Y. B.; Lee, S. K.; Lee, S. D.; Cho, M. J.; Ro, H. S. *Biotechnol. Lett.* **2011**, *33*, 921-927.

58. Guo, Z. R.; Gu, C. R.; Fan, X.; Bian, Z. P.; Wu, H. F.; Yang, D.; Gu, N.; Zhang, J. N. *Nanoscale Res. Lett.* **2009**, *4*, 1428-1433.

59. Chen, C. C.; Do, J. S.; Gu, Y. *Sensors* **2009**, *9*, 4635-4648.

60. Larue, C.; Calzolari, C.; Bertinchant, J.; Leclercq, F.; Grolleau, R.; Pau, B. *Clin. Chem.* **1993**, *39*, 972-979.

61. Davies, E.; Gawad, Y.; Takahashi, M.; Shi, Q. W.; Lam, P.; Styba, G.; Lau, A.; Heeschen, C.; Usategui, M.; Jackowski, G. *Clin. Biochem.* **1997**, *30*, 479-490.

62. Zhu, J. M.; Zou, N. L.; Zhu, D. N.; Wang, J.; Jin, Q. H.; Zhao, J. L.; Mao, H. J. *Clin. Chem.* **2011**, *57*, 1732-1738.

63. Coons, A. H.; Creech, H. J.; Jones, R. N. *Exp. Biol. Med.* **1941**, *47*, 200-202.

64. Funatsu, T.; Harada, Y.; Tokunaga, M.; Saito, K.; Yanagida, T. *Nature* **1995**, *374*, 555-559.

65. Tate, J.; Barth, J.; Bunk, D. *Analytical characteristics of commercial and research cardiac troponin I and T assays declared by the manufacturer* **2012**.

66. Dispenzieri, A.; Kyle, R. A.; Gertz, M. A.; Therneau, T. M.; Miller, W. L.; Chandrasekaran, K.; McConnell, J. P.; Burritt, M. F.; Jaffe, A. S. *Lancet* **2003**, *361*, 1787-1789.

67. Dasgupta, A.; Chow, L.; Wells, A.; Datta, P. *J. Clin. Lab. Anal.* **2001**, *15*, 175-177.

68. Keefe, A. D.; Pai, S.; Ellington, A. *Nat. Rev. Drug Discov.* **2010**, *9*, 537-550

69. Aslan, K. *Nano Biomed. Eng.* **2010**, *2*, 1-9.

70. Qureshi, A.; Gurbuz, Y.; Niazi, J. H. *Sensor Actuat. B-Chem.* **2012**, *171*, 62-76.

71. Wolf, M.; Juncker, D.; Michel, B.; Hunziker, P.; Delamarche, E. *Biosens. Bioelectron.* **2004**, *19*, 1193-1202.

72. Masson, J. F.; Battaglia, T. M.; Khairallah, P.; Beaudoin, S.; Booksh, K. S. *Anal. Chem.***2007**, *79*, 612-619.

73. Plowman, T. E.; Durstchi, J. D.; Wang, H. K.; Christensen, D. A.; Herron, J. N.; Reichert, W. M. *Anal. Chem.* **1999**, *71*, 4344-4352.

74. Luxton, R.; Badesha, J.; Kiely, J.; Hawkins, P. *Anal. Chem.***2004**, *76*, 1715-1719.

75. Eveness, J.; Kiely, J.; Hawkins, P.; Wraith, P.; Luxton, R. *Sensor Actuat. B-Chem.* **2009**, *139*, 538-542.

76. Pankhurst, Q. A.; Connolly, J.; Jones, S. K.; Dobson, J. *J. Phys. D Appl. Phys.* **2003**, *36*, R167-R181.

77. Senyei, A.; Widder, K.; Czerlinski, G. *J. Appl. Phys.* **1978**, *49*, 3578-3583.

78. Do, J.; Ahn, C. H. *Lab Chip* **2008**, *8*, 542-549.

79. Graham, D. L.; Ferreira, H. A.; Freitas, P. P. *Trends Biotechnol.* **2004**, *22*, 455-462.

80. Dittrich, P. S.; Tachikawa, K.; Manz, A. *Anal. Chem.* **2006**, *78*, 3887-3907.

81. Fitzpatrick, E.; McBride, S.; Yavelow, J.; Najmi, S.; Zanzucchi, P.; Wieder, R. *Clin. Chem.* **2006**, *52*, 1080-1088.

82. Liedberg, B.; Lundstrom, I.; Stenberg, E. *Sens. Actuator B-Chem.* **1993**, *11*, 63-72.

83. Murphy, C. J.; Gole, A. M.; Hunyadi, S. E.; Orendorff, C. J. *Inorg. Chem.* **2006**, *45*, 7544-7554.

84. Hu, J.; Ouyang, M.; Yang, P.; Lieber, C. M. *Nature* **1999**, *399*, 48-51.

85. Liu, C.; Huang, H.; Wu, Y.; Fan, S. *Appl. Phys. Lett.* **2004**, *84*, 4248-4250.

86. Rao, C. N. R.; Müller, A.; Cheetham, A. K. *The chemistry of nanomaterials: synthesis, properties and applications*. John Wiley & Sons, 2006.

87. Fan, H.; Wang, L.; Zhao, K.; Li, N.; Shi, Z.; Ge, Z.; Jin, Z. *Biomacromolecules* **2010**, *11*, 2345-2351.

88. Hiemenz, P. C.; Rajagopalan, R. *Principles of colloid and surface chemistry*; 3rd ed.; Marcel Dekker: New York, 1997.

89. Yang, S.-T.; Cao, L.; Luo, P. G.; Lu, F.; Wang, X.; Wang, H.; Meziani, M. J.; Liu, Y.; Qi, G.; Sun, Y.-P. *J. Am. Chem. Soc.* **2009**, *131*, 11308-11309.

90. Huang, P.; Lin, J.; Wang, X.; Wang, Z.; Zhang, C.; He, M.; Wang, K.; Chen, F.; Li, Z.; Shen, G. *Adv. Mater.* **2012**, *24*, 5104-5110.

91. Magrez, A.; Kasas, S.; Salicio, V.; Pasquier, N.; Seo, J. W.; Celio, M.; Catsicas, S.; Schwaller, B.; Forró, L. *Nano Lett.* **2006**, *6*, 1121-1125.

92. Aschberger, K.; Johnston, H. J.; Stone, V.; Aitken, R. J.; Tran, C. L.; Hankin, S. M.; Peters, S. A.; Christensen, F. M. *Regul. Toxicol. Pharmacol.* **2010**, *58*, 455-473.

93. Chen, R. J.; Choi, H. C.; Bangsaruntip, S.; Yenilmez, E.; Tang, X.; Wang, Q.; Chang, Y.-L.; Dai, H. *J. Am. Chem. Soc.* **2004**, *126*, 1563-1568.

94. Novoselov, K. S.; Geim, A. K.; Morozov, S. V.; Jiang, D.; Zhang, Y.; Dubonos, S.V.; Grigorieva, I. V.; Firsov, A. A. *Science* **2004**, *306*, 666-669.

95. Han, X.; Li, S.; Peng, Z.; Othman, A. M.; Leblanc, R. *ACS Sens.* **2016**, *1*, 106-114.

96. Lodish, H.; Baltimore, D.; Berk, A.; Zipursky, S. L.; Matsudaira, P.; Darnell, J. *Molecular cell biology*. New York: Scientific American Books, 1995.

97. Liu, H. P.; Ye, T.; Mao, C. D. *Angew. Chem. Int. Ed.* **2007**, *46*, 6473-6475.

98. Hu, S. L.; Niu, K. Y.; Sun, J.; Yang, J.; Zhao, N. Q.; Du, X. W. *J. Mater. Chem.* **2009**, *19*, 484-488.

99. Li, X. Y.; Wang, H. Q.; Shimizu, Y.; Pyatenko, A.; Kawaguchi, K.; Koshizaki, N. *Chem. Commun.* **2011**, *47*, 932-934.

100. Zhai, X. Y.; Zhang, P.; Liu, C. J.; Bai, T.; Li, W. C.; Dai, L. M.; Liu, W. G. *Chem.Commun.* **2012**, *48*, 7955-7957.

101. Li, H. T.; He, X. D.; Kang, Z. H.; Huang, H.; Liu, Y.; Liu, J. L.; Lian, S. Y.; Tsang, C. H. A.; Yang, X. B.; Lee, S. T. *Angew. Chem. Int. Ed.* **2010**, *49*, 4430-4434.

102. Zhu, S. J.; Meng, Q. N.; Wang, L.; Zhang, J. H.; Song, Y. B.; Jin, H.; Zhang, K.; Sun, H. C.; Wang, H. Y.; Yang, B. *Angew. Chem. Int. Ed.* **2013**, *52*, 3953-3957.

103. Li, S. H.; Wang, L. Y.; Chusuei, C. C.; Suarez, V. M.; Blackwelder, P. L.; Micic, M.; Orbulescu, J.; Leblanc, R. M. *Chem. Mater.* **2015**, *27*, 1764-1771.

104. Sun, Y. P.; Zhou, B.; Lin, Y.; Wang, W.; Fernando, K. A. S.; Pathak, P.; Meziani, M. J.; Harruff, B. A.; Wang, X.; Wang, H. F.; Luo, P. J. G.; Yang, H.; Kose, M. E.; Chen, B. L.; Veca, L. M.; Xie, S. Y. *J. Am. Chem. Soc.* **2006**, *128*, 7756-7757.

105. Cao, L.; Wang, X.; Meziani, M. J.; Lu, F. S.; Wang, H. F.; Luo, P. J. G.; Lin, Y.; Harruff, B. A.; Veca, L. M.; Murray, D.; Xie, S. Y.; Sun, Y. P. *J. Am. Chem. Soc.* **2007**, *129*, 11318-11319.

106. Yang, S. T.; Wang, X.; Wang, H. F.; Lu, F. S.; Luo, P. J. G.; Cao, L.; Meziani, M. J.; Liu, J. H.; Liu, Y. F.; Chen, M.; Huang, Y. P.; Sun, Y. P. *J. Phys. Chem. C* **2009**, *113*, 18110-18114.

107. Tao, H. Q.; Yang, K.; Ma, Z.; Wan, J. M.; Zhang, Y. J.; Kang, Z. H.; Liu, Z. *Small* **2012**, *8*, 281-290.

108. Kroto, H. W.; Heath, J. R.; Obrien, S. C.; Curl, R. F.; Smalley, R. E. *Nature* **1985**, *318*, 162-163.

109. Price, S. C.; Stuart, A. C.; Yang, L.; Zhou, H.; You, W. *J. Am. Chem. Soc.* **2011**, *133*, 4625-4631.

110. Geckeler, K. E.; Samal, S. *Polym. Int.* **1999**, *48*, 743-757.

111. Friedman, S. H.; Decamp, D. L.; Sijbesma, R. P.; Srdanov, G.; Wudl, F.; Kenyon, G. L. *J. Am. Chem. Soc.* **1993**, *115*, 6506-6509.

112. Hu, Z.; Guan, W.; Wang, W.; Huang, L.; Xing, H.; Zhu, Z. *Cell Biol. Int.* **2007**, *31*, 798-804.

113. Bernstein, R.; Prat, F.; Foote, C. S. *J. Am. Chem. Soc.* **1999**, *121*, 464-465.

114. Mikata, Y.; Takagi, S.; Tanahashi, M.; Ishii, S.; Obata, M.; Miyamoto, Y.; Wakita,K.; Nishisaka, Y.; Hirano, T.; Ito, T.; Hoshino, M.; Ohtsuki, C.; Tanihara, M.; Yano, S. *Bioorg. Med. Chem. Lett.* **2003**, *13*, 3289-3292.

115. Liu, J.; Rinzler, A. G.; Dai, H.; Hafner, J. H.; Bradley, R. K.; Boul, P. J.; Lu, A.; Iverson, T.; Shelimov, K.; Huffman, C. B. *Science* **1998**, *280*, 1253-1256.

116. Wang, X. S.; Li, Q. Q.; Xie, J.; Jin, Z.; Wang, J. Y.; Li, Y.; Jiang, K. L.; Fan, S. S. *Nano Lett.* **2009**, *9*, 3137-3141.

117. Iijima, S. *Nature* **1991**, *354*, 56-58.

118. Journet, C.; Maser, W. K.; Bernier, P.; Loiseau, A.; delaChapelle, M. L.; Lefrant, S.; Deniard, P.; Lee, R.; Fischer, J. E. *Nature* **1997**, *388*, 756-758.

119. Huang, S. M.; Cai, X. Y.; Liu, J. *J. Am. Chem. Soc.* **2003**, *125*, 5636-5637.

120. Kerman, K.; Vestergaard, M.; Tamiya, E. *Anal. Chem.* **2007**, *79*, 6881-6885.

121. Aviram, A.; Ratner, M. A. *Chem. Phys. Lett.* **1974**, *29*, 277-283.

122. Tans, S. J.; Verschueren, A. R. M.; Dekker, C. *Nature* **1998**, *393*, 49-52.

123. De Volder, M. F. L.; Tawfick, S. H.; Baughman, R. H.; Hart, A. J. *Science* **2013**, *339*, 535-539.

124. Liu, Z.; Tabakman, S.; Welsher, K.; Dai, H. *Nano Res.* **2009**, *2*, 85-120.

125. Jacobs, C. B.; Peairs, M. J.; Venton, B. J. *Anal. Chim. Acta* **2010**, *662*, 105-127.

126. Wang, J.; Musameh, M. *Anal. Chim. Acta* **2004**, *511*, 33-36.

127. Shi, X.; von Dem Bussche, A.; Hurt, R. H.; Kane, A. B.; Gao, H. *Nat. Nanotechnol.* **2011**, *6*, 714-719.

128. Lee, S. M.; Lee, Y. H. *Appl. Phys. Lett.* **2000**, *76*, 2877-2879.

129. Baughman, R. H.; Zakhidov, A. A.; de Heer, W. A. *Science* **2002**, *297*, 787-792.

130. Chen, Y.; Shaw, D. T.; Bai, X. D.; Wang, E. G.; Lund, C.; Lu, W. M.; Chung, D. D. L. *Appl. Phys. Lett.* **2001**, *78*, 2128-2130.

131. Sharma, R.; Baik, J. H.; Perera, C. J.; Strano, M. S. *Nano Lett.* **2010**, *10*, 398-405.

132. Mann, J. A.; Rodriguez-Lopez, J.; Abruna, H. D.; Dichtel, W. R. *J. Am. Chem. Soc.* **2011**, *133*, 17614-17617.

133. Lu, C. H.; Yang, H. H.; Zhu, C. L.; Chen, X.; Chen, G. N. *Angew. Chem. Int. Edit.***2009**, *48*, 4785-4787.

134. Li, S. H.; Aphale, A. N.; Macwan, I. G.; Patra, P. K.; Gonzalez, W. G.; Miksovska,J.; Leblanc, R. M. *ACS Appl. Mater. Interfaces* **2012**, *4*, 7068-7074.

135. Othman, A. M.; Li, S. H.; Leblanc, R. M. *Anal. Chim. Acta* **2013**, *787*, 226-232.

136. Li, S. H.; Mulloor, J. J.; Wang, L. Y.; Ji, Y. W.; Mulloor, C. J.; Micic, M.; Orbulescu, J.; Leblanc, R. M. *ACS Appl. Mater. Interfaces* **2014**, *6*, 5704-5712.

137. Li, S. H.; Stein, A. J.; Kruger, A.; Leblanc, R. M. *J. Phys. Chem. C* **2013**, *117*, 16150-16158.

138. Goedert, M.; Spillantini, M. G. *Science* **2006**, *314*, 777-781.

139. Duthey, B. *A Public Health Approach to Innovation* **2013**, 1-74.

140. Mattson, M. P. *Nature* **2004**, *430*, 631-639.

141. Ferri, C. P.; Prince, M.; Brayne, C.; Brodaty, H.; Fratiglioni, L.; Ganguli, M.; Hall,K.; Hasegawa, K.; Hendrie, H.; Huang, Y. Q.; Jorm, A.; Mathers, C.; Menezes, P. R.; Rimmer, E.; Scazufca, M.; Intl, A. D. *Lancet* **2005**, *366*, 2112-2117.

142. Knowles, T. P. J.; Vendruscolo, M.; Dobson, C. M. *Nat. Rev. Mol. Cell. Bio.* **2014**,*15*, 384-396.

143. Zhang, M.; Mao, X. B.; Yu, Y.; Wang, C. X.; Yang, Y. L.; Wang, C. *Adv. Mater.* **2013**, *25*, 3780-3801.

144. Eisenberg, D.; Jucker, M. *Cell* **2012**, *148*, 1188-1203.

145. Habchi, J.; Arosio, P.; Perni, M.; Costa, A. R.; Yagi-Utsumi, M.; Joshi, P.; Chia, S.; Cohen, S. I. A.; Müller, M. B. D.; Linse, S.; Nollen, E. A. A.; Dobson, C. M.; Knowles, T. P. J.; Vendruscolo, M. *Sci. adv.* **2016**, *2*, e1501244- e1501257.

146. Geula, C.; Wu, C. K.; Saroff, D.; Lorenzo, A.; Yuan, M. L.; Yankner, B. A. *Nat. Med.* **1998**, *4*, 827-831.

147. Arosio, P.; Vendruscolo, M.; Dobson, C. M.; Knowles, T. P. *Trends Pharmacol. Sci.* **2014**, *35*, 127-135.

148. Suzuki, N.; Cheung, T. T.; Cai, X. D.; Odaka, A.; Otvos, L.; Eckman, C.; Golde, T. E.; Younkin, S. G. *Science* **1994**, *264*, 1336-1340.

149. Cohen, S. I. A.; Arosio, P.; Presto, J.; Kurudenkandy, F. R.; Biverstal, H.; Dolfe, L.; Dunning, C.; Yang, X. T.; Frohm, B.; Vendruscolo, M.; Johansson, J.; Dobson, C. M.; Fisahn, A.; Knowles, T. P. J.; Linse, S. *Nat. Struct. Mol. Biol.* **2015**, *22*, 207-213.

150. Selkoe, D. J. *Nature* **1999**, *399*, A23-A31.

151. Lansbury, P. T. *Curr. Opin. Chem. Biol.* **1997**, *1*, 260-267.

152. Jakob-Roetne, R.; Jacobsen, H. *Angew. Chem. Int. Ed.* **2009**, *48*, 3030-3059.

153. Teplow, D. B.; Lazo, N. D.; Bitan, G.; Bernstein, S.; Wyttenbach, T.; Bowers, M. T.; Baumketner, A.; Shea, J. E.; Urbanc, B.; Cruz, L.; Borreguero, J.; Stanley, H. E. *Acc. Chem. Res.* **2006**, *39*, 635-645.

154. Funke, S. A.; Willbold, D. *Curr. Pharm. Des.* **2012**, *18*, 755-767.

155. Tjernberg, L. O.; Naslund, J.; Lindqvist, F.; Johansson, J.; Karlstrom, A. R.; Thyberg, J.; Terenius, L.; Nordstedt, C. *J. Biol. Chem.* **1996**, *271*, 8545-8548.

156. Gessel, M. M.; Wu, C.; Li, H. Y.; Bitan, G.; Shea, J. E.; Bowers, M. T. *Biochemistry* **2012**, *51*, 108-117.

157. Xiong, N.; Dong, X. Y.; Zheng, J.; Liu, F. F.; Sun, Y. *ACS Appl. Mater. Interfaces* **2015**, *7*, 5650.

158. Sievers, S. A.; Karanicolas, J.; Chang, H. W.; Zhao, A.; Jiang, L.; Zirafi, O.; Stevens, J. T.; Munch, J.; Baker, D.; Eisenberg, D. *Nature* **2011**, *475*, 96-100.

159. Man, B. Y. W.; Chan, H. M.; Leung, C. H.; Chan, D. S. H.; Bai, L. P.; Jiang, Z. H.; Li, H. W.; Ma, D. L. *Chem. Sci.* **2011**, *2*, 917-921.

160. Scott, L. E.; Telpoukhovskaia, M.; Rodriguez-Rodriguez, C.; Merkel, M.; Bowen, M. L.; Page, B. D. G.; Green, D. E.; Storr, T.; Thomas, F.; Allen, D. D.; Lockman, P. R.; Patrick, B. O.; Adam, M. J.; Orvig, C. *Chem. Sci.* **2011**, *2*, 642-648.

161. Wang, Q. M.; Yu, X.; Patal, K.; Hu, R. D.; Chuang, S.; Zhang, G.; Zheng, J. *ACS Chem. Neurosci.* **2013**, *4*, 1004-1015.

162. Zheng, X. Y.; Liu, D.; Klarner, F. G.; Schrader, T.; Bitan, G.; Bowers, M. T. *J. Phys. Chem. B* **2015**, *119*, 4831-4841.

163. Nie, Q.; Du, X. G.; Geng, M. Y. *Acta Pharmacol. Sin.* **2011**, *32*, 545-551.

164. Lee, H. H.; Choi, T. S.; Lee, S. J. C.; Lee, J. W.; Park, J.; Ko, Y. H.; Kim, W. J.; Kim, K.; Kim, H. I. *Angew. Chem. Int. Ed.* **2014**, *53*, 7461-7465.

165. Ma, S. H.; Rudkevich, D. M.; Rebek, J. *J. Am. Chem. Soc.* **1998**, *120*, 4977-4981.

166. Ebbing, M. H. K.; Villa, M. J.; Valpuesta, J. M.; Prados, P.; de Mendoza, J. *Proc. Natl. Acad. Sci. USA* **2002**, *99*, 4962-4966.

167. Mansikkamaki, H.; Nissinen, M.; Rissanen, K. *Angew. Chem. Int. Ed.* **2004**, *43*, 1243-1246.

168. Bian, S. D.; Zieba, S. B.; Morris, W.; Han, X.; Richter, D. C.; Brown, K. A.; Mirkin, C. A.; Braunschweig, A. B. *Chem. Sci.* **2014**, *5*, 2023-2030.

169. Rodik, R. V.; Boyko, V. I.; Kalchenko, V. I. *Curr. Med. Chem.* **2009**, *16*, 1630-1655.

170. Mokhtari, B.; Pourabdollah, K. *J. Incl. Phenom. Macro.* **2012**, *73*, 1-15.

171. Mutihac, L.; Lee, J. H.; Kim, J. S.; Vicens, J. *Chem. Soc. Rev.* **2011**, *40*, 2777-2796.

172. Biswas, A.; Kurkute, P.; Saleem, S.; Jana, B.; Mohapatra, S.; Mondal, P.; Adak, A.; Ghosh, S.; Saha, A.; Bhunia, D.; Biswas, S. C.; Ghosh, S. *ACS Chem. Neurosci.* **2015**, *6*, 1309-1316.

173. Liu, D. X.; Xu, Y. C.; Feng, Y.; Liu, H.; Shen, X.; Chen, K. X.; Ma, J. P.; Jiang, H. L. *Biochemistry* **2006**, *45*, 10963-10972.

174. Simoni, E.; Serafini, M. M.; Bartolini, M.; Caporaso, R.; Pinto, A.; Necchi, D.; Fiori, J.; Andrisano, V.; Minarini, A.; Lanni, C.; Rosini, M. *ChemMedChem* 2016, 11, 1309-1317.

175. Sanabria, E.; Esteso, M. A.; Perez-Redondo, A.; Vargas, E.; Maldonado, M. *Molecules* **2015**, *20*, 9915-9928.

176. Peng, Z.; Li, S.; Han, X.; Al-Youbi, A.; Bashammakh, A.; El-Shahawi, M.; Leblanc, R. M. *Anal. Chim. Acta* **2016**, *937*, 113-118.

177. Madadkar-Sobhani, A.; Guallar, V. *Nucleic Acids Res* **2013**, *41*, W322-W328.

178. D. A. Case, V. Babin, J. T. Berryman, R. M. Betz, Q. Cai, D. S. Cerutti, T. E. Cheatham, I. Darden, R. E. Duke, H. Gohlke, A. W. Goetz, S. Gusarov, N. Homeyer, P. Janowski, J. Kaus, I. Kolossv ´ary, A. Kovalenko, T. S. Lee, S. LeGrand, T. Luchko, R. Luo, B. Madej, K. M. Merz, F. Paesani, D. R. Roe, A. Roitberg, C. Sagui, R. Salomon-Ferrer, G. Seabra, C. L. Simmerling, W. Smith, J. Swails, R. C. Walker, J. Wang, R. M. Wolf, X. Wu and P. A. Kollman, AMBER 14, University of California, San Francisco, 2014.

179. Wang, J. M.; Wolf, R. M.; Caldwell, J. W.; Kollman, P. A.; Case, D. A. *J. Comput. Chem.* **2004**, *25*, 1157-1174.

180. Maier, J. A.; Martinez, C.; Kasavajhala, K.; Wickstrom, L.; Hauser, K. E.; Simmerling, C. *J. Chem. Theory Comput.* **2015**, *11*, 3696-3713.

181. Arosio, P.; Cukalevski, R.; Frohm, B.; Knowles, T. P. J.; Linse, S. *J. Am. Chem. Soc.* **2014**, *136*, 219-225.

182. Hellstrand, E.; Boland, B.; Walsh, D. M.; Linse, S. *ACS Chem. Neurosci.* **2010**, *1*, 13-18.

183. Walsh, D. M.; Thulin, E.; Minogue, A. M.; Gustavsson, N.; Pang, E.; Teplow, D. B.; Linse, S. *FEBS J.* **2009**, *276*, 1266-1281.

184. Cohen, S. I. A.; Linse, S.; Luheshi, L. M.; Hellstrand, E.; White, D. A.; Rajah, L.; Otzen, D. E.; Vendruscolo, M.; Dobson, C. M.; Knowles, T. P. J. *Proc. Natl. Acad. Sci. USA* **2013**, *110*, 9758-9763.

185. Cohen, S. I. A.; Vendruscolo, M.; Dobson, C. M.; Knowles, T. P. J. *J. Mol. Biol.* **2012**, *421*, 160-171.

186. Nicholls, A.; Sharp, K. A.; Honig, B. *PROTEINS* **1991**, *11*, 281-296.

187. Lesné, S.; Koh, M. T.; Kotilinek, L.; Kayed, R.; Glabe, C. G.; Yang, A.; Gallagher, M.; Ashe, K. H. *Nature* **2006**, *440*, 352-357.

188. Linse, S.; Cabaleiro-Lago, C.; Xue, W. F.; Lynch, I.; Lindman, S.; Thulin, E.; Radford, S. E.; Dawson, K. A. *Proc. Natl. Acad. Sci. U.S.A.* **2007**, *104*, 8691-8696.

189. Hardy, J. *Trends Neurosci.* **1997**, *20*, 154-159.

190. Collins, S. R.; Douglass, A.; Vale, R. D.; Weissman, J. S. *PLoS Biol.* **2004**, *2*, 1582-1590.

191. Han, X.; Park, J.; Wu, W.; Malagon, A.; Wang, L.; Vargas, E.; Wikramanayake, A.; Houk, K.; Leblanc, R. M. *Chem. Sci.* **2017**, DOI: 10.1039/c6sc04854d.

192. Cabaleiro-Lago, C.; Quinlan-Pluck, F.; Lynch, I.; Lindman, S.; Minogue, A. M.; Thulin, E.; Walsh, D. M.; Dawson, K. A.; Linse, S. *J. Am. Chem. Soc.* **2008**, *130*, 15437-15443.

193. Luo, Y.; Bolon, B.; Kahn, S.; Bennett, B. D.; Babu-Khan, S.; Denis, P.; Fan, W.; Kha, H.; Zhang, J. H.; Gong, Y. H.; Martin, L.; Louis, J. C.; Yan, Q.; Richards, W. G.; Citron, M.; Vassar, R. *Nat. Neurosci.* **2001**, *4*, 231-232.

194. Bowman, G. L.; Kaye, J. A.; Moore, M.; Waichunas, D.; Carlson, N. E.; Quinn, J. F. *Neurology* **2007**, *68*, 1809-1814.

195. Yang, S. T.; Cao, L.; Luo, P. G. J.; Lu, F. S.; Wang, X.; Wang, H. F.; Meziani, M. J.; Liu, Y. F.; Qi, G.; Sun, Y. P. *J. Am. Chem. Soc.* **2009**, *131*, 11308-11309.

196. Han, X.; Li, S. H.; Peng, Z. L.; Al-Yuobi, A. R. O.; Bashammakh, A. S. O.; EI-Shahawi, M. S.; Leblanc, R. M. *J. Oleo Sci.* **2016**, *65*, 1-7..

197. Sun, Y. P.; Zhou, B.; Lin, Y.; Wang, W.; Fernando, K. A. S.; Pathak, P.; Meziani, M. J.; Harruff, B. A.; Wang, X.; Wang, H. F.; Luo, P. J. G.; Yang, H.; Kose, M. E.; Chen, B. L.; Veca, L. M.; Xie, S. Y. *J. Am. Chem. Soc.* **2006**, *128*, 7756-7757.

198. Zhang, X. Y.; Zhang, Y.; Wang, Y.; Kalytchuk, S.; Kershaw, S. V.; Wang, Y. H.; Wang, P.; Zhang, T. Q.; Zhao, Y.; Zhang, H. Z.; Cui, T.; Wang, Y. D.; Zhao, J.; Yu, W. W.; Rogach, A. L. *ACS Nano* **2013**, *7*, 11234-11241.

199. Zheng, M.; Liu, S.; Li, J.; Qu, D.; Zhao, H. F.; Guan, X. G.; Hu, X. L.; Xie, Z. G.; Jing, X. B.; Sun, Z. C. *Adv. Mater.* **2014**, *26*, 3554-3560.

200. Li, S. H.; Peng, Z. L.; Dallman, J.; Baker, J.; Othman, A. M.; Blackwelder, P. L.; Leblanc, R. M. *Colloids Surf., B* **2016**, *145*, 251-256.

201. Li, S.; Wang, L.; Chusuei, C. C.; Suarez, V. M.; Blackwelder, P. L.; Micic, M.; Orbulescu, J.; Leblanc, R. M. *Chem. Mater.* **2015**, *27*, 1764-1771.

202. Pronk, S.; Pall, S.; Schulz, R.; Larsson, P.; Bjelkmar, P.; Apostolov, R.; Shirts, M. R.; Smith, J. C.; Kasson, P. M.; van der Spoel, D.; Hess, B.; Lindahl, E. *Bioinformatics* **2013**, *29*, 845-854.

203. Monticelli, L.; Kandasamy, S. K.; Periole, X.; Larson, R. G.; Tieleman, D. P.; Marrink, S. J. *J. Chem. Theory Comput.* **2008**, *4*, 819-834.

204. Dominguez, L.; Foster, L.; Straub, J. E.; Thirumalai, D. *Proc. Natl. Acad. Sci. U.S.A.* **2016**, *113*, E5281-E5287.

205. Todorova, N.; Makarucha, A. J.; Hine, N. D. M.; Mostofi, A. A.; Yarovsky, I. *PLoS Comput. Biol.* 2013, *9,* e1003360- e1003373.

206. Nasica-Labouze, J.; Nguyen, P. H.; Sterpone, F.; Berthoumieu, O.; Buchete, N. V.; Cote, S.; De Simone, A.; Doig, A. J.; Faller, P.;́ Garcia, A.; Laio, A. *Chem. Rev.* **2015**, *115*, 3518-3563.

207. Ball, K. A.; Phillips, A. H.; Nerenberg, P. S.; Fawzi, N. L.; Wemmer, D. E.; Head-Gordon, T. *Biochemistry* **2011**, *50*, 7612-7628.

208. Hung, A.; Griffin, M. D. W.; Howlett, G. J.; Yarovsky, I. *Eur. Biophys. J.* **2008**, *38*, 99-110.

209. Motzer, R. J. *Nature* **2016**, *537*, S111-S111.

210. Sawyers, C. L. *Nature* **2008**, *452*, 548-552.

211. Strimbu, K.; Tavel, J. A. *Curr. Opin. Hiv Aids* **2010**, *5*, 463-466.

212. Suprun, E.; Bulko, T.; Lisitsa, A.; Gnedenko, O.; Ivanov, A.; Shumyantseva, V.; Archakov, A. *Biosens. Bioelectron.* **2010**, *25*, 1694-1698.

213. Zhang, A. Q.; Lieber, C. M. *Chem. Rev.* **2016**, *116*, 215-257.

214. Labib, M.; Sargent, E. H.; Kelley, S. O. *Chem. Rev.* **2016**, *116*, 9001-9090.

215. Berggren, M.; Richter-Dahlfors, A. *Adv. Mater.* **2007**, *19*, 3201-3213.

216. Shen, J. W.; Li, Y. B.; Gu, H. S.; Xia, F.; Zuo, X. L. *Chem. Rev.* **2014**, *114*, 7631-7677.

217. Liu, J. W.; Lu, Y. *Angew. Chem. Int. Ed.* **2006**, *45*, 90-94.

218. Wu, J. S.; Liu, W. M.; Ge, J. C.; Zhang, H. Y.; Wang, P. F. *Chem. Soc. Rev.* **2011**, *40*, 3483-3495.

219. Liu, J.; Lu, Y. *J. Am. Chem. Soc.* **2007**, *129*, 9838-9839.

220. Zhao, M.; Josephson, L.; Tang, Y.; Weissleder, R. *Angew. Chem. Int. Ed.* **2003**, *42*, 1375-1378.

221. Zuo, X. L.; Xiao, Y.; Plaxco, K. W. *J. Am. Chem. Soc.* **2009**, *131*, 6944-6945.

222. Hatch, A.; Kamholz, A. E.; Hawkins, K. R.; Munson, M. S.; Schilling, E. A.; Weigl, B. H.; Yager, P. *Nat. Biotechnol.* **2001**, *19*, 461-465.

223. Choi, Y.; Ho, N. H.; Tung, C. H. *Angew. Chem. Int. Ed.* **2007**, *46*, 707-709.

224. Saha, K.; Agasti, S. S.; Kim, C.; Li, X. N.; Rotello, V. M. *Chem. Rev.* **2012**, *112*, 2739-2779.

225. Liu, X.; Dai, Q.; Austin, L.; Coutts, J.; Knowles, G.; Zou, J. H.; Chen, H.; Huo, Q. *J. Am. Chem. Soc.* **2008**, *130*, 2780-2782.

226. Gaster, R. S.; Hall, D. A.; Nielsen, C. H.; Osterfeld, S. J.; Yu, H.; Mach, K. E.; Wilson, R. J.; Murmann, B.; Liao, J. C.; Gambhir, S. S.; Wang, S. X. *Nat. Med.* **2009**, *15*, 1327-U130.

227. Arlett, J. L.; Myers, E. B.; Roukes, M. L. *Nat. Nanotechnol.* **2011**, *6*, 203-215.

228. Mayer, K. M.; Hafner, J. H. *Chem. Rev.* **2011**, *111*, 3828-3857.

229. Anker, J. N.; Hall, W. P.; Lyandres, O.; Shah, N. C.; Zhao, J.; Van Duyne, R. P. *Nat. Mater.* **2008**, *7*, 442-453.

230. Willets, K. A.; Van Duyne, R. P. *Annu. Rev. Phys. Chem.* **2007**, *58*, 267-297.

231. Hutter, E.; Fendler, J. H. *Adv. Mater.* **2004**, *16*, 1685-1706.

232. Atwater, H. A.; Polman, A. *Nat. Mater.* **2010**, *9*, 205-213.

233. Knight, M. W.; Sobhani, H.; Nordlander, P.; Halas, N. J. *Science* **2011**, *332*, 702-704.

234. Okamoto, K.; Niki, I.; Shvartser, A.; Narukawa, Y.; Mukai, T.; Scherer, A. *Nat. Mater.* **2004**, *3*, 601-605.

235. Yonzon, C. R.; Jeoungf, E.; Zou, S. L.; Schatz, G. C.; Mrksich, M.; Van Duyne, R. P. *J. Am. Chem. Soc.* **2004**, *126*, 12669-12676.

236. Mayer, K. M.; Lee, S.; Liao, H.; Rostro, B. C.; Fuentes, A.; Scully, P. T.; Nehl, C. L.; Hafner, J. H. *ACS Nano* **2008**, *2*, 687-692.

237. Englebienne, P. *Analyst* **1998**, *123*, 1599-1603.

238. Shokri Kojori, H.; Yun, J.-H.; Paik, Y.; Kim, J.; Anderson, W. A.; Kim, S. J. *Nano Lett.* **2015**, *16*, 250-254.

239. Kojori, H. S.; Ji, Y.; Paik, Y.; Braunschweig, A. B.; Kim, S. J. *Nanoscale* **2016**, *8*, 17357-17364

240. Malaguarnera, G.; Giordano, M.; Paladina, I.; Berretta, M.; Cappellani, A.; Malaguarnera, M. *Dig. Dis. Sci.* **2010**, *55*, 2744-2755.

241. Zhang, S.-Y.; Lin, B.-D.; Li, B.-R. *FEBS Open Bio* **2015**, *5*, 240-244.